The hierarchy of Davydov's Ansätze and its applications

Yang Zhao[a], Kewei Sun[a,b], Lipeng Chen[c], and Maxim Gelin[b]

[a] Division of Materials Science, Nanyang Technological University, Singapore 639798, Singapore
[b] School of Science, Hanghzhou Dianzi University, Hangzhou 310018, China
[c] Max Planck Institute for the Physics of Complex Systems, Nöthnitzer Str 38, Dresden, Germany

E-mail: YZhao@ntu.edu.sg

October 21, 2021

Abstract

This review provides a bird's eye view over the development of the hierarchy of Davydov's Ansätze and its applications in a variety of problems in computational physical chemistry. Davydov's original solitons appeared in the 1970s as a candidate for vibrational energy carriers in proteins, thanks to their association with the Fröhlich Hamiltonian and the Holstein molecular crystal model. Momentum-space projection of those solitary waves emerged to be great approximations to the ground-state wave functions of the extended Holstein Hamiltonian, lending unambiguous evidence to the absence of formal quantum phase transitions in those systems. The multiple Davydov Ansätze are introduced, with increasing multiplicity, as incremental improvements of their corresponding single-Ansatz parents. The time-dependent variational formalism of Davydov's Ansätze is discussed in great detail, and the relative deviation of the Ansätze is constructed to quantify how faithfully they follow the Schrödinger equation, a quantity that is shown to vanish in the limit of large multiplicities. Three approaches to finite-temperature variational dynamics of Davydov's Ansätze are demonstrated, namely, the Monte Carlo importance sampling, the method of thermofield dynamics, and the method of displaced number states. Applications of Davydov's Ansätze are given to variants of the spin-boson model, the Landau-Zener transition, the Holstein Hamiltonian, energy transfer in light-harvesting, and singlet fission in organic photovoltaics. As an example, simulation of multidimensional spectroscopic signals via Davydov's Ansätze is fully implemented for the finite-temperature fission process in crystalline rubrene.

1 Introduction

Recent years have seen an increasingly prolific use of multidimensional spectroscopy as an indispensable tool to interrogate energy and charge transfer in a large variety of material in photosynthesis and photovoltaics [1–3]. In contrast to linear spectroscopy with often congested spectral lines, nonlinear spectroscopic techniques allow for many laser interactions to differentiate dynamical processes of diverging time scales. For example, two-dimensional (2D) spectroscopy, which emerged as a powerful technique in infrared/visible spectral ranges [4, 5], employs three ultra-short laser pulses, separated by two time delays, namely, the coherence time and the waiting time, with the resultant signal field

spectrally resolved in a given phase-matched direction. Interpretation of those spectroscopic responses in terms of underlying molecular structure necessitates complex simulations to extract intrinsic system dynamics encoded in spectroscopic signals, and often involves computation of the third-order polarization $P^{(3)}(t)$ after solving coupled, many-body dynamics [6, 7].

A conceptually straightforward approach to third-order polarization is the density matrix formalism, where nonlinear response functions are obtained by propagating the density matrix of the material system along different Liouville pathways [6]. The numerically exact approaches of hierarchical equations of motion (HEOM) [8, 9] and the quasiadiabatic path integral (QUAPI) [10, 11] are among the most successful density matrix methods for computing the nonlinear spectra [12–15]. But both methods are computationally prohibitive in the strong system-bath coupling regime and at low temperatures despite overcoming well-known limitations of other equations-of-motion approaches, including the rotating wave approximation, the Markovian approximation, and the perturbative approximant that is associated with the dynamical positivity problem. Furthermore, the construction of the HEOM restricts its applications to only certain forms of bath spectral densities, although several spectrum decomposition techniques have been developed to tackle this issue [16–18].

Wave function-based methods offer an alternative to the density matrix formalism for computing third-order response functions at zero and finite temperatures. To solve the time-dependent Schrödinger equation, the many-body wave function is expanded in a set of basis functions that are propagated in time by numerical means. Typical examples of wave function-based methods include the multiconfiguration time-dependent Hartree (MCTDH) method and its multilayer extension (ML-MCTDH) [19–22], the multiple spawning method [23, 24], the hierarchy of Davydov's Ansätze (HDA) [25–31], the multiconfigurational Ehrenfest (MCE) method [32–34], and other basis set methods [35–38], delivering accurate descriptions of quantum dynamics at zero and low temperatures. To extend wave function-based methods such as the HDA approach to finite-temperature dynamics of many-body systems, several useful techniques can be borrowed, including the method of Monte Carlo importance sampling to initialize vibrational modes in order to properly account for temperature effects [39, 40], the method of thermo-field dynamics (TFD) that maps the Liouville-von Neumann equation for the density matrix to the TFD Schrödinger equation with twice as many degrees of freedom [41–49], and the method of displaced number states exploiting the fact that initial excitation of the vibrational manifold can be conveniently described by displaced number states of the bath degrees of freedom [50, 51].

The focus of this review is on the HDA method, i.e., the formalism of employing Davydov's Ansätze [52, 53] and their multistate extensions (i.e., linear superpositions of the single Davydov

Ansätze) [26, 27, 29, 54] to reveal accurate dynamics of quantum many-body systems and the corresponding spectroscopic manifestations. By using the time-dependent variational principle, those Davydov trial states have been applied, with great success, to describe the ground-state as well as the dynamic properties of the paradigmatic spin-boson model (SBM) as well as the Holstein molecular crystal model [26, 27, 40, 45, 52–56]. The Davydov Ansätze are also integrated into the nonlinear response function formalism, allowing for efficient simulations of single molecule and 2D electronic spectra of molecular aggregates for close experimental comparison [25, 57, 58].

The remainder of the Review is structured as follows. Given in Sec. 2 is a concise history of Davydov's solitons and the hierarchy of Ansätze derived from them. Several variants of Davydov's original solitons are introduced from their association with the Fröhlich Hamiltonian and the Holstein molecular crystal model, and momentum-space projection of those solitons are unveiled as approximations of varying precision to the ground-state wave functions of the extended Holstein Hamiltonian. The multiple Davydov Ansätze are discussed next as incremental improvements of their corresponding single-Ansatz parents with increasing multiplicity. In Sec. 3, the time-dependent variational formalism for Davydov's Ansätze is given in great detail, using the multi-D_2 Ansatz as an example, and the relative deviation of the Ansätze is introduced to quantify the accuracy of the variational trial states. In Sec. 4, three approaches to finite-temperature dynamics of Davydov's Ansätze are discussed, namely, the Monte Carlo importance sampling, the method of thermofield dynamics, and the method of displaced number states. In Sec. 5, simulation of linear spectra and multidimensional spectroscopic signals via Davydov's Ansätze is detailed. In Sec. 6, we discuss applications of Davydov's Ansätze to the SBM and its variants, the Landau-Zener (LZ) transition, the Holstein Hamiltonian, energy transfer in light-harvesting, and singlet fission (SF) in organic photovoltaics. How the HDA approach is related to other Gaussian basis-set methods is elaborated in Sec. 7. Lastly, conclusions are drawn in Sec. 8.

2 Brief History of Davydov Ansätze

In the early 1970s, Alexander S. Davydov proposed a new mechanism for transport and localization of vibrational energy in proteins, in which the jargon of Davydov's soliton first appeared [59–61]. Specifically, the vibrational energy of the CO stretching (or Amide-I) oscillators that is localized on the alpha-helix of proteins may distort the helix structure, leading to trapping of the Amide-I oscillation energy by acoustic phonons, a phenomenon also called self-trapping (borrowed from theory of classical nonlinearity, also used in the polaron literature). Scott and Careri *et al.* have also carried out experiments on crystalline acetanilide and discussed their results using Davydov's

model [62, 63]. Modifying Davydov's original equations for the α-helix soliton, Scott claimed using numerical results that such solitions may appear under physiological conditions [64]. Initially, two versions of Davydov's soliton were introduced, namely, the Davydov D_1 and D_2 trial states, with the latter being a simplified form of the former [65–67].

It was realized early on that Davydov's solitons have their roots in polaron theory [68, 69], and equations of motion that the solitons follow in their time evolution differ from those proposed by Davydov. As the quantum theory of polaron is linear, it is intriguing to consider how a polaronic entity is capable to exhibit the behavior of a nonlinear classical system [70]. Along this line, various theories have been devised connecting approximate solutions to the Fröhlich Hamiltonian to the solitons of the nonlinear Schrödinger equation [71–73].

Davydov's soliton, initially proposed in the context of energy transport in proteins, was a spatially localized entity that is deprived of nearly all quantum characteristics. Its solitary structure is seemingly at odds with the translational invariant symmetry of the Fröhlich Hamiltonian, to which the solitons are approximate solutions. Čápek and Krausová showed that extended, translationally invariant states always have lower energies than their solitary parent states [74]. Translationally invariant remakes of Davydov's solitons, obtained by projections onto the momentum space have attracted much attention in the context of the Holstein molecular crystal model, and have been systematically investigated [75–84]. The Davydov D_2 Ansatz, for example, can be projected onto the crystal-momentum space, yielding the celebrated Toyozawa Ansatz [75], a relatively decent approximation to the ground-state wave functions of the Holstein molecular crystal model for most of the phase diagram except the regime of weak exciton-phonon coupling. A delocalized, momentum-conserving state that simplifies Toyozawa's Ansatz to one with only two variational parameters was worked out for the Holstein polaron in mid-1980s [78], while the full version of Toyozawa's Ansatz was solved in early 1990s, revealing intricate details of the exciton-phonon quasi-particle previously unavailable [79, 82]. The projection of Davydov D_1 Ansatz onto the crystal-momentum space leads to the delocalized D_1 Ansatz, which is considerably more accurate than Toyozawa's Ansatz and yields results with accuracy on par with the computationally expensive density matrix renormalization group (DMRG) method [84].

Mutliple Davydov Ansätze are simply linear superpositions of the corresponding single Davydov Ansätze in which the bosonic components of the trial states are much more refined with the multiplied coherent states. Inspired by numerically exact solutions to the problem of an electronic excitation hopping between two sites, Shore and Sander experimented with trial wave functions with two Gaussians to represent the phonon deformation [77], which are forerunners of the mutliple

Davydov Ansätze. To a certain extent, the aforementioned translationally invariant descendents of Davydov's solitary states are also examples of the mutliple Davydov Ansätze since they are the superposition of N copies of the single Davydov Ansätze for a lattice of N sites. Recently, the multiple Davydov D_1 Ansatz has been used as the variational wave function of choice to uncover a quantum phase transition from a doubly degenerate "localized phase" to the other doubly degenerate "delocalized phase" for a sub-Ohmic spin-boson model with simultaneous diagonal and off-diagonal coupling, with corresponding transition points determined accurately, fully consistent with the results from the methods of DMRG and exact diagonalization [85].

Time-dependent variants of the multiple Davydov Ansätze have not been implemented to extract numerically exact dynamics of quantum many-body systems until very recently [27, 54]. The multi-D_2 Ansatz has been utilized to uncover high-precision dynamics of Holstein polaron which results in fast, accurate implementation of multidimensional spectroscopy [27]. The SBM phase diagram of the dynamical coherent-incoherent crossover near critical points have been obtained by the multi-D_1 Ansatz, with the critical value of the spectral-density exponent estimated by the extrapolation [54].

2.1 Davydov's solitons and their momentum-space projections

As a quasi-classical (or semi-classical) construct, Davydov's soliton is shown, under certain approximations, to be a solution to the nonlinear Schrödinger equation frequently encountered in soliton studies [86]. The starting point of Davydov is the Fröhlich/Holstein-type Hamiltonian with linear coupling between intramolecular excitations (Frenkel excitons) and molecular vibrations (phonons), extending the concept of the polaron from its original context in polar crystals (Fröhlich polaron) to phonon-dressed excitons in molecular systems.

In the second quantized form, the generalized one-dimensional Holstein Hamiltonian, also known as the extended Holstein molecular crystal model, is given by

$$\begin{aligned}
\hat{H}_{\rm Hol}^{\rm ext} &= \hat{H}_{\rm ex} + \hat{H}_{\rm ph} + \hat{H}_{\rm ex-ph}, \\
\hat{H}_{\rm ex} &= \sum_k J_k a_k^\dagger a_k, \\
\hat{H}_{\rm ph} &= \sum_q \omega_q b_q^\dagger b_q, \\
\hat{H}_{\rm ex-ph} &= N^{-1/2} \sum_{kq} \omega_q f_{-k}^q a_{k+q}^\dagger a_k (b_q + b_{-q}^\dagger),
\end{aligned} \tag{1}$$

where $a_k^\dagger$, $b_q^\dagger$ (a_k, b_q) are the exciton and phonon creation (annihilation) operators of wave vectors k and q, respectively, and ω_q is the frequency of qth mode. J_k is the Fourier transform of the site-space transfer integral J_n (n denotes the hopping distance in units of lattice spacing). f_k^q is

the linear exciton-phonon coupling parameter (linear exciton-phonon coupling leads to a shift in the equilibrium position of the nuclei, while quadratic coupling alters the phonon frequency). We have set $\hbar = 1$ in this review for simplicity. Here we only consider interactions of the exciton with deformations on the lattice site it resides on (or its nearest neighbors) due to the short-range nature of exciton-phonon coupling. Hamitonian (1) is the generalized Holstein molecular crystal model in one dimension, which describes quasi-one-dimensional solids (anisotropic molecular crystals and especially polymeric crystals) characterized by considerable anisotropy in their electronic transport properties. A continuum Hamiltonian which preceded the above lattice Hamiltonian is the Fröhlich Hamiltonian, originally proposed by H. Fröhlich for the problem of a slow electron in an ionic crystal [87] (the "real" polaron problem). Thanks to the fact that systems of coupled electrons and phonons constitute some of the simplest yet richest structures in condensed matter physics, the Fröhlich Hamiltonian has been the subject of continuous attention for the last seventy years. The interest extends far beyond physical descriptions of materials. The field has been a testing ground for various theoretical techniques, including the first application of field theoretic approaches to condensed matter physics. Recent applications of the Fröhlich Hamiltonian are found in the context of low dimensional systems such as CuO_2-based materials [88], quantum wires[89, 90], and superfluids[91]. The original form of the Fröhlich Hamiltonian also contains three terms [92]:

$$\hat{H}_{\rm Froh} = \frac{\vec{P}^2}{2} + \sum_{\vec{q}} b^\dagger_{\vec{q}} b_{\vec{q}} + i(\frac{\sqrt{2}\pi\alpha}{V})^{\frac{1}{2}} \sum_{\vec{q}} \frac{b^\dagger_{\vec{q}} e^{-i\vec{q}\cdot\vec{X}} - \text{H.c.}}{|\vec{q}|} \tag{2}$$

where the Einstein phonon frequency ω and electron mass m_e have been set to unity, $\vec{X}$ is the position vector of the electron and $\vec{P}$ its conjugate momentum, $b^\dagger_{\vec{q}}$ ($b_{\vec{q}}$) is the phonon creation (annihilation) operator, and the coupling constant α is given in terms of the static and high frequency dielectric constants ϵ and ϵ_∞ by $\alpha = 2^{-\frac{1}{2}} e^2 (\epsilon_\infty^{-1} - \epsilon^{-1})$. The electron-phonon coupling in Eq. (2) arises from a long-range Coulomb interaction, which is to be distinguished from the short-range nonpolar interaction in Holstein systems.

The Fröhlich Hamiltonian is but one of the models that one may consider in the discussion of Davydov's solitons. The Hamiltonian describes two linear fields, such as an electronic excitation or an intramolecular vibration, and a collection of phonons, interacting with one another. The most immediate concept associated with the Fröhlich Hamiltonian, or its discrete extension in a lattice, the Holstein Hamiltonian, is in fact a polaron, which is defined as a quasiparticle excitation in a solid consisting of a bare particle nontrivially correlated with the deformation or polarization quanta of the solid. Davydov's solitons are, on the other hand, particle-like solutions to nonlinear Schrödinger equation that are connected to the polarons in the correspondence limit [93]. While it is likely that

the polarons are in fact the quantum solitons, Davydov's solitons represent limiting forms of the polaron in the adiabatic limit [82].

The stability of Davydov's soliton in the presence of thermal fluctuations has been an issue of major concern and sustained contention in the field. A quantum Monte Carlo study of the model proposed by Davydov for the description of energy transport processes in the α helix shows that Davydov's soliton exhibits classical hopping behavior at physiological temperature [94, 95], in agreement with earlier simulations of finite-temperature molecular dynamics [96]. Highly localized spatially and bearing a close resemblance to Davydov's soliton, a coherent structure is found to exist in quantum Monte Carlo simulation at low temperatures, but is substantially destroyed above 7 K [94]. Förner also studied the thermal stability of Davydov's D_2 Ansatz by including temperature effects in the model [97–99], but claimed that Davydov's soliton is stable at room temperature in his simulation under certain conditions on parameter values which may be fulfilled in proteins, citing additional supporting arguments from Langevin-equation models and perturbative approaches [97].

Davydov's solitons are localized entities that were proposed to describe a soliton-like transport phenomenon in proteins. In order to connect Davydov's solitions to accurate variational trial states for translationally invariant Hamiltonians such as the aforementioned Holstein molecular crystal model, Hamitonian (1), one has to carry out projections of the localized Davydov solitons onto the crystal-momentum space. As an illustration of this projection procedure, we first introduce a translationally invariant trial state (with some resemblance to the Davydov D_2 Ansatz):

$$|\Psi^K_{\rm small}\rangle = N^{-\frac{1}{2}} \sum_n e^{iKn} a_n^\dagger \exp[-\sum_{n_2} (\delta^K_{n_2-n} b^\dagger_{n_2} - \delta^{K*}_{n_2-n} b_{n_2})] \; |0\rangle, \tag{3}$$

where $|0\rangle$ stands for the vacuum state for both the exciton and the phonon field, and δ^K_n is the variational parameter for phonon displacements. Ansatz (3), which we shall call the small polaron Ansatz, is constructed (apart from a factor $N^{1/2}$) via the application of the following projection operator characterized by parameter K,

$$\hat{\Xi}(K) = N^{-1} \sum_n e^{i(K-\hat{P})n}, \tag{4}$$

onto a localized structure centered, without loss of generality, at site $n = 0$

$$a_0^\dagger \exp[-\sum_{n_2} (\delta^K_{n_2} b^\dagger_{n_2} - \delta^{K*}_{n_2} b_{n_2})] \; |0\rangle. \tag{5}$$

Here $\hat{P}$ is the crystal momentum operator

$$\hat{P} = \sum_k k a_k^\dagger a_k + \sum_q q b_q^\dagger b_q. \tag{6}$$

The localized structure consists of a single excitation localized at site $n = 0$ accompanied by a phonon cloud of a single coherent state characterized by δ_n^K. The operator (4) yields a sum over n of localized structures (i.e., Davydov's solitons) displaced from the origin by n lattice spacings, and each weighted by a factor of e^{iKn}.

In 1961, Toyozawa proposed a translationally invariant trial state [75], which we call Toyozawa's Ansatz:

$$|\Psi_{\rm Toyo}^K\rangle = N^{-\frac{1}{2}} \sum_n e^{iKn} \sum_{n_1} \psi_{n_1-n}^K a_{n_1}^\dagger \exp[-\sum_{n_2} (\lambda_{n_2-n}^K b_{n_2}^\dagger - \lambda_{n_2-n}^{K*} b_{n_2})]|0\rangle. \tag{7}$$

Here λ_n^K again characterizes the phonon displacement, and the new addition ψ_n^K is the exciton amplitude which describes the distribution of the electronic excitation (ψ_n^K is reduced to $\delta_{n,0}$ in the small polaron Ansatz). Toyozawa's Ansatz can be constructed by making the structure

$$|\Psi_{\rm D_2}\rangle = \sum_{n_1} \psi_{n_1}^K a_{n_1}^\dagger \exp[-\sum_{n_2} (\lambda_{n_2}^K b_{n_2}^\dagger - \lambda_{n_2}^{K*} b_{n_2})]|0\rangle \tag{8}$$

translationally invariant by means of the projection operator of (4) ($\psi_{n_1}^K$ in general has a localized form). The above localized structure is also the so-called "$\rm D_2$" Ansatz in the theory of Davydov's solitons, which attempts to explain the localization and transport of vibrational energy in proteins via polaron models.

Unlike the small polaron Ansatz (3), with localized electronic excitation on a single site ($\psi_n^K \to \delta_{n,0}$), Eq. (8) allows its electronic excitation to adapt self-consistently to the phonon field, despite that the two are not explicitly correlated since n_1 and n_2 are independent of each other. Is such explicit correlation important to the structure and the energy of the ground state of Hamiltonian (3)? Again we will refer to the literature on the theory of Davydov's solitons, in which a more general localized Ansatz state by the name of the Davydov "$\tilde{\rm D}$" Ansatz was proposed by Ivić *et al.*[100]

$$|\Psi_{\tilde{\rm D}}\rangle = \sum_{n_1} \psi_{n_1}^K a_{n_1}^\dagger \exp\{-\sum_{n_2} [(\alpha_{n_2}^K - \beta_{n_2-n_1}^K) b_{n_2}^\dagger - {\rm H.c.}]\}|0\rangle \tag{9}$$

where H.c. denotes Hermitian conjugate, and the new variational parameter β_n^K is introduced to provide a direct correlation between the exciton amplitude and the phonon field. Eq. (9) is in fact an intermediate step between the localized structure of Toyozawa's Ansatz (8) and the so-called "$\rm D_1$" Ansatz in the theory of Davydov's solitons:

$$|\Psi_{\rm D_1}\rangle = \sum_{n_1} \psi_{n_1}^K a_{n_1}^\dagger \exp[-\sum_{n_2} (\gamma_{n_2,n_1}^K b_{n_2}^\dagger - {\rm H.c.})]|0\rangle. \tag{10}$$

As compared with the Davydov "$\rm D_1$" Ansatz with triple-indexed variational parameter γ_{n_2,n_1}^K, the dependence of the phonon structure on the exciton label n_1 enters Eq. (9) solely through $\beta_{n_2-n_1}^K$.

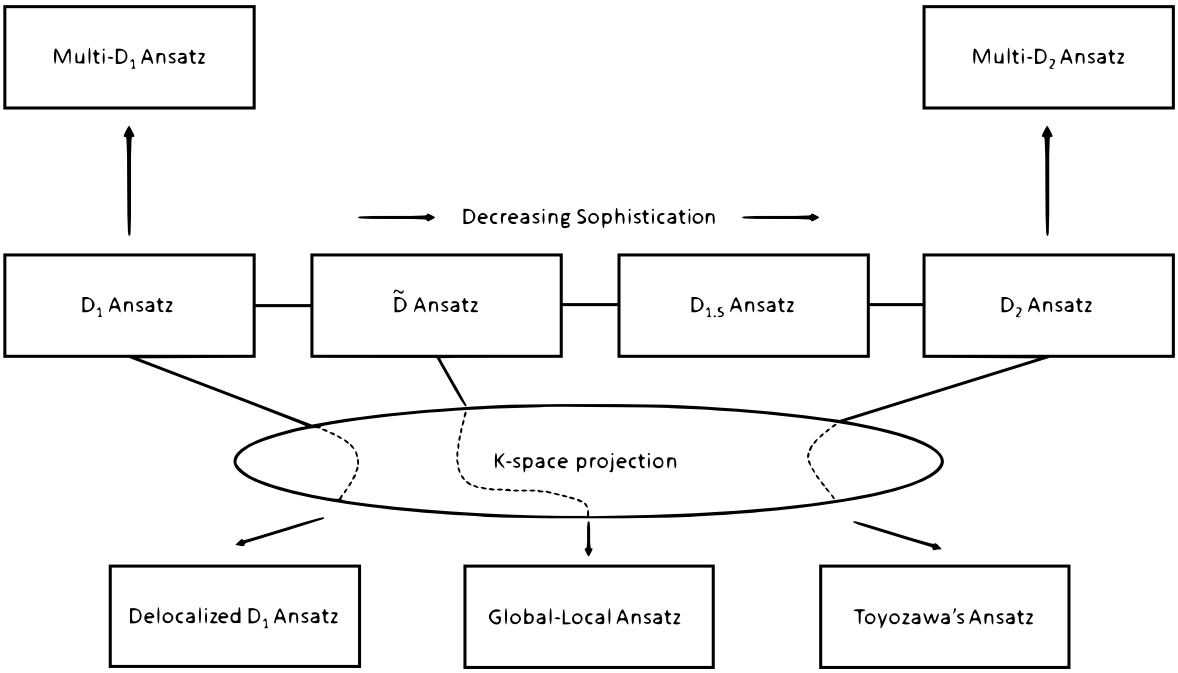

Figure 1: Schematic of the hierarchy of Davydov Ansätze. Sitting at the second row from the top are Davydov's solitons, the D_1 Ansatz, the $\tilde{D}$ Ansatz, the $D_{1.5}$ Ansatz, and the D_2 Ansatz, in the order of decreasing sophistication. Three translationally invariant Davydov Ansätze are listed at the bottom row. Two time-dependent, multiple Davydov Ansätze, the multi-D_1 Ansatz and multi-D_2 Ansatz, occupy the top row.

While there is some redundancy between α_n^K and β_n^K, α_n^K cannot be absorbed into β_n^K because $\beta_{n_2-n_1}^K$ in Eq. (9) only captures the part of the phonon field that depends on the relative separation $n_2 - n_1$ between the excitation and the phonon. If β_n^K is weakly dependent on n, then it is not well distinguished from α_n^K when the summation over the exciton index n_1 is performed. If we define β_q^K as the Fourier transform of β_n^K, then the long wavelength components of β_q^K are by construction somewhat repetitive of α_q^K, the Fourier transform of α_n^K.

Delocalization of Eq. (9) yields the delocalized Davydov "$\tilde{\text{D}}$" Ansatz [53]

$$|\Psi_{\text{GL}}^K\rangle = N^{-\frac{1}{2}} \sum_n e^{iKn} \sum_{n_1} \psi_{n_1-n}^K a_{n_1}^\dagger \exp\{-\sum_{n_2}[(\alpha_{n_2-n}^K - \beta_{n_2-n_1}^K) b_{n_2}^\dagger - H.c.]\}|0\rangle, \tag{11}$$

which is also known as the Global-Local Ansatz [83]. Similarly, projection of the Davydov "D_1" Ansatz on to the crystal-momentum space leads to the delocalized Davydov "D_1" Ansatz [84]

$$|\Psi_{\text{dD}_1}^K\rangle = N^{-\frac{1}{2}} \sum_n e^{iKn} \sum_{n_1} \psi_{n_1-n}^K a_{n_1}^\dagger \exp\{-\sum_{n_2}[\gamma_{n_2-n,n_1-n}^K b_{n_2}^\dagger - H.c.]\}|0\rangle, \tag{12}$$

The exciton amplitudes ψ_n^K serve as weights in a linear superposition of phonon coherent states

if Toyozawa's Ansatz (7) is viewed in the following form[101]:

$$|\Psi^K_{\rm Toyo}\rangle = N^{-\frac{1}{2}} \sum_n e^{iKn} a^\dagger_n \sum_{n_1} e^{-iKn_1} \psi^K_{n_1} \exp[-\sum_{n_2} (\lambda^K_{n_2+n_1-n} b^\dagger_{n_2} - \lambda^{K*}_{n_2+n_1-n} b_{n_2})]|0\rangle.$$

Similarly, the Global-Local Ansatz (11) may also be written as

$$|\Psi^K_{\rm GL}\rangle = N^{-\frac{1}{2}} \sum_n e^{iKn} a^\dagger_n \sum_{n_1} e^{-iKn_1} \psi^K_{n_1} \exp\{-\sum_{n_2} [(\alpha^K_{n_2+n_1-n} - \beta^K_{n_2-n}) b^\dagger_{n_2} - H.c.]\}|0\rangle.$$

In this form, we see that $\beta^K_{n_2-n}$ represents a component of the phonon field that remains constant when the linear superposition sum over n_1 is performed on phonon coherent states.

In Fig. 1, a schematic drawing of the hierarchy of Davydov Ansätze is presented, illustrating various Davydov trial states discussed earlier and the intertwined relations among them. Sitting at the second row from the top are Davydov's solitons, namely, the D_1 Ansatz, the $\tilde{D}$ Ansatz, the $D_{1.5}$ Ansatz, and the D_2 Ansatz, all of which are localized in the site space. Upon projection onto the crystal-momentum space, translationally invariant Davydov Ansätze at the bottom row are generated, in decreasing sophistication, the delocalized D_1 Ansatz, the Global-Local Ansatz, and Toyozawa's Ansatz.

2.2 Multiple Davydov trial states

Using as an example the two-site problem of the SBM, we demonstrate how the aforementioned Davydov trial states can be extended to include a linear combination of coherent states in order to increase their accuracies in the study of the dynamical properties of many-body quantum systems. The Hamiltonian of the spin-boson model, $\hat{H}_{\rm SBM}$, is written as

$$\begin{aligned} \hat{H}_{\rm SBM} &= \hat{H}_{\rm S} + \hat{H}_{\rm SB} + \hat{H}_{\rm B}, \\ \hat{H}_{\rm S} &= \frac{\epsilon}{2}\sigma_z - \frac{\Delta}{2}\sigma_x, \\ \hat{H}_{\rm SB} &= \frac{\sigma_z}{2} \sum_l \lambda_l (b^\dagger_l + b_l), \\ \hat{H}_{\rm B} &= \sum_l \omega_l b^\dagger_l b_l. \end{aligned} \tag{13}$$

Here, σ_i $(i = x, z)$ are Pauli operators defined as $\sigma_x = |+\rangle\langle -| + |-\rangle\langle +|$ and $\sigma_z = |+\rangle\langle +| - |-\rangle\langle -|$ with $|+\rangle$ and $|-\rangle$ representing two electronic localized states. ϵ and Δ is the energy bias and the coupling constant between two electronic states, respectively. $b^\dagger_l$ (b_l) is creation (annihilation) operator for the bosonic bath mode of frequency ω_l, and λ_l is the strength of the coupling between the system and the lth mode.

Firstly, the Davydov D_1 Ansatz can be readily extended to form its multiple variant $|\Psi^M_{\mathrm{D}_1}(t)\rangle$, i.e., the so-called multi-D_1 Ansatz with mulplicity M, as follows

$$|\Psi^M_{\mathrm{D}_1}(t)\rangle = \sum_u^M A_u(t)|+\rangle \exp(\sum_l f_{ul}(t)b_l^\dagger - \mathrm{H.c.})|0\rangle_{\mathrm{ph}} + \sum_u^M B_u(t)|-\rangle \exp(\sum_l g_{ul}(t)b_l^\dagger - \mathrm{H.c.})|0\rangle_{\mathrm{ph}} \quad (14)$$

Here $|+\rangle(|-\rangle)$ stands for the spin-up (spin-down) state, and $|0\rangle_{\mathrm{ph}}$ is the vacuum state of the boson bath. $A_u(t), B_u(t)$ are variational parameters used to represent the amplitudes of states $|+\rangle$ and $|-\rangle$, respectively, and $f_{ul}(t)$ and $g_{ul}(t)$ are the corresponding phonon displacements, where u and l denotes the uth coherent state and the lth mode, respectively.

Similarly, the multiple variant of the Davydov D_2 Ansatz, also known as the multi-D_2 Ansatz, is given by

$$|\Psi^M_{\mathrm{D}_2}(t)\rangle = \sum_u^M [A_u(t)|+\rangle + B_u(t)|-\rangle] \exp(\sum_l f_{ul}(t)b_l^\dagger - \mathrm{H.c.})|0\rangle_{\mathrm{ph}} \quad (15)$$

A trial state with its complexity falling between those of the Davydov D_1 and D_2 Ansatz, the Davydov $\mathrm{D}_{1.5}$ Ansatz [102] can also be extended to form the multi-$\mathrm{D}_{1.5}$ Ansatz of multiplicity M as follows

$$|\Psi^M_{\mathrm{D}_{1.5}}(t)\rangle = \sum_u^M A_u(t)|+\rangle e^{(\sum_l (f_{ul}(t)-N_l)b_l^\dagger - \mathrm{H.c.})}|0\rangle_{\mathrm{ph}} + \sum_u^M B_u(t)|-\rangle e^{(\sum_l (f_{ul}(t)+N_l)b_l^\dagger - \mathrm{H.c.})}|0\rangle_{\mathrm{ph}} \quad (16)$$

where $N_l = \lambda_l/2\omega_l$. Similar extensions can be made to the Davydov $\tilde{\mathrm{D}}$ Ansatz.

From a quick comparison of Eqs. (14) and (15), it is noted that the multi-D_2 Ansatz can be viewed as a simplified version of the multi-D_1 Ansatz of the same multiplicity in that the bath displacements in the former are the same for the spin up and spin down states. However, upon a close inspection of the expression of the multi-D_2 Ansatz in Eq. (15), the multi-D_1 Ansatz can also be viewed as a special case of the multi-D_2 Ansatz of twice the multiplicty: $A_u(t) = 0$ for even u, and $B_u(t) = 0$ for odd u. The multi-$\mathrm{D}_{1.5}$ Ansatz, on the other hand, sits between the multi-D_1 and multi-D_2 Ansätze of the same multiplicity in the level of sophistication, i.e., the bath displacements in the spin up and spin down states are not independent but are linearly connected as compared to the multi-D_1 Ansatz, similar to what has been encountered in the case of the Davydov $\tilde{\mathrm{D}}$ Ansatz with its sophistication sandwiched between that of the Davydov D_1 and D_2 Ansatz.

Lastly, in a similar manner as above, the multiple-site dynamic problem of Hamiltonian (1) can be solved numerically to any desired precision by extending the Davydov D_2 and D_1 trial states, Eqs. (8) and (10), to their respective multiple variants, provided sufficient multiplicities of the Ansätze [26, 27]. The multiple-site(state) multi-D_1 Ansatz of multiplicity M can be compactly expressed as [27, 29]

$$|\Psi^M_{\mathrm{D}_1}(t)\rangle = \sum_m |m\rangle \sum_{k=1}^M A_{mk}(t) e^{\left(\sum_l f_{m,kl}(t)b_l^\dagger - \mathrm{H.c.}\right)}|0\rangle_{\mathrm{ph}}, \quad (17)$$

where $|m\rangle$ represents the mth excitation state of a multiple-state system, or the excitation at the mth site of a multiple-site system. The corresponding version for the multi-D_2 Ansatz is written as [27, 103]

$$|\Psi^M_{D_2}(t)\rangle = \sum_m |m\rangle \sum_{k=1}^{M} A_{mk}(t) e^{\left(\sum_l f_{kl}(t) b_l^\dagger - \text{H.c.}\right)} |0\rangle_{\text{ph}}. \tag{18}$$

In the subsequent sections, we will use $|D^M_{1,2}\rangle$ to refer to the multiple Davydov Ansätze $|\Psi^M_{D_{1,2}}\rangle$. In Fig. 1, occupying the top row are the two time-dependent, multiple Davydov Ansätze, namely, the multi-D_1 Ansatz and multi-D_2 Ansatz, which have been successfully applied to a number of many-body quantum systems [104–106], yielding numerically exact solutions.

3 Time-Dependent Variational Scheme of Davydov's Ansätze

Using the multiple-state multi-D_2 Ansatz (18) as an example, we demonstrate in this section how equations of motion for the variational parameters in a Davydov Ansatz can be derived in the framework of the time-dependent variational principle. The equations that govern the time propagation of the variational parameters μ_i can be obtained from Euler equations of motion,

$$\frac{d}{dt}\frac{\partial L}{\partial \dot{\mu}_i^*} - \frac{\partial L}{\partial \mu_i^*} = 0, \tag{19}$$

where the Lagrangian is given by

$$L = \frac{i}{2}\left[\langle D_2^M(t)|\frac{\overrightarrow{\partial}}{\partial t}|D_2^M(t)\rangle - \langle D_2^M(t)|\frac{\overleftarrow{\partial}}{\partial t}|D_2^M(t)\rangle\right] - \langle D_2^M(t)|H|D_2^M(t)\rangle =: L_{\text{td}} - L_{\text{H}}. \tag{20}$$

Using the normalization of the Davydov Ansatz, the derivative needs only to be taken to the right, simplifying the derivation considerably. Thus the first term in Eq. (20), L_{td}, is given by

$$L_{\text{td}} = i\langle D_2^M(t)|\frac{\overrightarrow{\partial}}{\partial t}|D_2^M(t)\rangle = i\sum_m \sum_{k,p}^{M} A^*_{mk} S_{kp}\left(\dot{A}_{mp} + A_{mp}\sum_q \frac{2f^*_{kq}\dot{f}_{pq} - f^*_{pq}\dot{f}_{pq} - f_{pq}\dot{f}^*_{pq}}{2}\right), \tag{21}$$

where the Debye-Waller factor is $S_{kp} = \exp\sum_q\left\{-\left(|f_{kq}|^2 + |f_{pq}|^2\right)/2 + f^*_{kq}f_{pq}\right\}$. The second term L_{H} is in fact the average energy of the system in Eq. (20), which can be obtained as

$$\begin{aligned} L_{\text{H}} &= \left\langle D_2^M(t)\right| H \left|D_2^M(t)\right\rangle \\ &= \sum_m \sum_{k,p}^{M} \epsilon_m A^*_{mk} A_{mp} S_{kp} + \sum_m \sum_{m'\neq m} \sum_{k,p}^{M} J_{mm'} A^*_{mk} A_{m'p} S_{kp} \\ &\quad + \sum_m \sum_{k,p}^{M} A^*_{mk} A_{mp} \sum_q \omega_q f^*_{kq} f_{pq} S_{kp} + \sum_m \sum_{m'} \sum_{k,p}^{M} \sum_q g_q^{mm'} A^*_{mk} A_{m'p}\left(f_{pq} + f^*_{kq}\right) S_{kp}. \end{aligned} \tag{22}$$

It follows that the time-dependent variational principle results in equations of motion for A_{mp},

$$
\begin{aligned}
&i\sum_{p}^{M}\dot{A}_{mp}S_{kp}+i\sum_{p}^{M}A_{mp}\sum_{q}\left[-\frac{1}{2}\left(\dot{f}_{pq}f_{pq}^{*}+f_{pq}\dot{f}_{pq}^{*}\right)+f_{kq}^{*}\dot{f}_{pq}\right]S_{kp}\\
&=\epsilon_{m}\sum_{p}^{M}A_{mp}S_{kp}+\sum_{m'\neq m}\sum_{p}^{M}J_{mm'}A_{m'p}S_{kp}+\sum_{p}^{M}A_{mp}\sum_{q}\omega_{q}f_{kq}^{*}f_{pq}S_{kp}\\
&+\sum_{p}^{M}A_{mp}\sum_{q}g_{q}^{mm}\left(f_{pq}+f_{kq}^{*}\right)S_{kp}+\sum_{m'\neq m}\sum_{p}^{M}A_{m'p}\sum_{q}g_{q}^{mm'}\left(f_{pq}+f_{kq}^{*}\right)S_{kp}.
\end{aligned}
\tag{23}
$$

Similarly, the equations of motion for f_{pq} are

$$
\begin{aligned}
&i\sum_{m}\sum_{p}^{M}A_{mk}^{*}\dot{A}_{mp}f_{pq}S_{kp}+i\sum_{m}\sum_{p}^{M}A_{mk}^{*}A_{mp}\dot{f}_{pq}S_{kp}\\
&+i\sum_{m}\sum_{p}^{M}A_{mk}^{*}A_{mp}f_{pq}S_{kp}\sum_{q'}\left[f_{kq'}^{*}\dot{f}_{pq'}-\frac{1}{2}\left(\dot{f}_{pq'}f_{pq'}^{*}+f_{pq'}\dot{f}_{pq'}^{*}\right)\right]\\
&=\sum_{m}\sum_{p}^{M}\epsilon_{m}A_{mk}^{*}A_{mp}f_{pq}S_{kp}+\sum_{m}\sum_{m'\neq m}\sum_{p}^{M}J_{mm'}A_{mk}^{*}A_{m'p}f_{pq}S_{kp}\\
&+\sum_{m}\sum_{p}^{M}A_{mk}^{*}A_{mp}\omega_{k}f_{pq}S_{kp}+\sum_{m}\sum_{p}^{M}f_{pq}\sum_{q'}A_{mk}^{*}A_{mp}\omega_{q'}f_{kq'}^{*}f_{pq'}S_{kp}\\
&+\sum_{m}\sum_{m'}\sum_{p}^{M}A_{mk}^{*}A_{m'p}g_{q}^{mm'}S_{kp}+\sum_{m}\sum_{m'}\sum_{p}^{M}f_{pq}\sum_{q'}A_{mk}^{*}A_{m'p}g_{q'}^{mm'}\left(f_{pq'}+f_{kq'}^{*}\right)S_{kp}
\end{aligned}
\tag{24}
$$

To avoid singularity, noise satisfying the uniform distribution within $[-10^{-5},10^{-5}]$ is added to the variational parameters A_{mk} and f_{kl} of the initial states. Eqs. (23) and (24) construct a set of linear differential equations, i.e., $\mathbf{A}\dot{\vec{x}}=\mathbf{B}$, which can be solved by the fourth-order Runge Kutta method. However, since the parameter matrix $\mathbf{A}$ is generally not a square matrix of full rank, the inverse of $\mathbf{A}$ does not always exist. Fortunately, the Moore-Penrose pseudo inverse is a generalization of the matrix inverse when the matrix may not be invertible. It is worth mentioning that the pseudo inverse function "pinv" based on the singular value decomposition can be called in Matlab.

In addition, we can introduce the relative deviation to evaluate the performance of the multi-$\mathrm{D}_{1,2}$ Ansatz. Assuming the trial wave function $|\mathrm{D}_{1,2}^{M}(t)\rangle=|\Psi(t)\rangle$ at the time t, we introduce a deviation vector $\vec{\delta}(t)$ to quantify the accuracy of the variational dynamics based on the multiple Davydov trial states,

$$
\vec{\delta}(t)=\vec{\chi}(t)-\vec{\gamma}(t)=\frac{\partial}{\partial t}|\Psi(t)\rangle-\frac{\partial}{\partial t}|\mathrm{D}_{1,2}^{M}(t)\rangle. \tag{25}
$$

where the vectors $\vec{\chi}(t)$ and $\vec{\gamma}(t)$ obey the Schrödinger equation $\vec{\chi}(t) = \partial|\Psi(t)\rangle/\partial t = -i\hat{H}|\Psi(t)\rangle$ and the variational dynamics $\vec{\gamma}(t) = \partial|\mathrm{D}^M_{1,2}\rangle/\partial t$ in Eq. (19), respectively. Using the Schrödinger equation and the relationship $|\Psi(t)\rangle = |\mathrm{D}^M_{1,2}(t)\rangle$ at the moment t, the deviation vector $\vec{\delta}(t)$ can be calculated as

$$\vec{\delta}(t) = -i\hat{H}|\mathrm{D}^M_{1,2}(t)\rangle - \frac{\partial}{\partial t}|\mathrm{D}^M_{1,2}(t)\rangle. \tag{26}$$

Thus, Ansatz deviation from the exact Schrödinger dynamics can be quantified by the amplitude of the deviation vector $\Delta(t) = ||\vec{\delta}(t)||$. In order to view the deviation in the parameter space, a dimensionless relative deviation σ is calculated as

$$\sigma = \frac{\max\{\Delta(t)\}}{\mathrm{mean}\{N_{\mathrm{err}}(t)\}}, \qquad t \in [0, t_{\max}]. \tag{27}$$

where $N_{\mathrm{err}}(t) = ||\vec{\chi}(t)||$ is the amplitude of the time derivative of the wave function,

$$N_{\mathrm{err}}(t) = \sqrt{\langle\frac{\partial}{\partial t}\Psi(t)|\frac{\partial}{\partial t}\Psi(t)\rangle} = \sqrt{\langle \mathrm{D}^M_{1,2}(t)|\hat{H}^2|\mathrm{D}^M_{1,2}(t)\rangle}. \tag{28}$$

4 Finite-Temperature Dynamics of Davydov's Ansätze

4.1 Monte Carlo Importance Sampling

The conventional procedure of time-dependent variation described in Sec. 3 is only applicable at zero temperature. Since laboratory measurements are inevitably carried out at nonzero temperatures, it is essential to understand many-body quantum dynamics and its spectral manifestation at finite temperatures. To extend the variational approach to finite temperatures, in this section a Monte Carlo method is adopted, similar to what is employed in the ML-MCTDH method [21, 39].

For simplicity, we demonstrate the approach using the $\hat{H}_{\mathrm{SBM}}$ of Eq. (13) as an example. The initial density matrix for the entire system is assumed to have a factorized form, *i.e.* $\hat{\rho}_{\mathrm{tot}}(0) = \hat{\rho}(0)\hat{\rho}^{\mathrm{eq}}_{\mathrm{B}}$, where $\hat{\rho}(0) = |+\rangle\langle+|$. The extension to more general initial conditions with superposition of $|-\rangle$ and $|+\rangle$ is straightforward, which is important for modeling nonlinear spectroscopy.

The expectation value of an observable $\hat{O}(t)$ at finite temperatures can be expressed as

$$\langle\hat{O}(t)\rangle = \mathrm{Tr}\{\hat{O}e^{-i\hat{H}_{\mathrm{SBM}}t}\hat{\rho}^{\mathrm{eq}}_{\mathrm{B}}|1\rangle\langle 1|e^{i\hat{H}_{\mathrm{SBM}}t}\}. \tag{29}$$

In principle, the observables at t can be calculated in any representations. We employ the coherent state representation to calculate the observable as

$$\langle\hat{O}(t)\rangle = \pi^{-N_b}\int d^2\boldsymbol{\alpha}\langle\boldsymbol{\alpha}|\langle 1|\hat{\rho}^{\mathrm{eq}}_{\mathrm{B}}e^{i\hat{H}_{\mathrm{SBM}}t}\hat{O}e^{-i\hat{H}_{\mathrm{SBM}}t}|1\rangle|\boldsymbol{\alpha}\rangle, \tag{30}$$

where $|\boldsymbol{\alpha}\rangle$ denotes a direct product of coherent states $(\alpha_1, \alpha_2, \alpha_3, \cdots, \alpha_{N_b})$ for the N_b discrete bath modes, and is expressed as $|\boldsymbol{\alpha}\rangle = \exp(\sum_l \alpha_l b_l^\dagger - \text{H.c.})\big|0\big\rangle_{\text{B}}$. Each α_i runs over all of the feasible coherent states. The element of area $d^2\alpha_i$ on the complex plane of α_i denotes $d\text{Re}(\alpha_i) \cdot d\text{Im}(\alpha_i)$, which $\text{Re}(\alpha_i)$ and $\text{Im}(\alpha_i)$ are the real and imaginary part of α_i, respectively. The equilibrium density matrix of the bath at a finite temperature is a diagonal matrix, and can be expressed as[107, 108]

$$\hat{\rho}_{\text{B}}^{\text{eq}} = \int d^2\boldsymbol{\alpha}\, p(\boldsymbol{\alpha};\, \beta)|\boldsymbol{\alpha}\rangle\langle\boldsymbol{\alpha}|, \tag{31}$$

where $p(\boldsymbol{\alpha};\, \beta)$ represents the diagonal elements of the density matrix in the coherent state representation and can be expressed as[109]

$$p(\boldsymbol{\alpha};\, \beta) = \prod_l^{N_b} \left[\frac{e^{\beta\omega_l} - 1}{\pi} \exp\left(-|\alpha_l|^2 (e^{\beta\omega_l} - 1) \right) \right]. \tag{32}$$

Here $\beta = 1/(k_B T)$ (k_B is the Boltzmann constant and T is the temperature). As shown in Eq. (32), $p(\boldsymbol{\alpha};\, \beta)$ is a positive defined function of $\boldsymbol{\alpha}$ and can be seen as a probability density. Substituting Eq. (31) into Eq. (30), the observables $\langle \hat{O}(t) \rangle$ at finite temperatures can be obtained by the average according to the probability density $p(\boldsymbol{\alpha};\, \beta)$ as

$$\begin{aligned} \langle \hat{O}(t) \rangle &= \int d^2\boldsymbol{\alpha} p(\boldsymbol{\alpha};\, \beta) \langle\boldsymbol{\alpha}| \langle 1| e^{i\hat{H}_{\text{SBM}} t} \hat{O} e^{-i\hat{H}_{\text{SBM}} t} |1\rangle |\boldsymbol{\alpha}\rangle \\ &= \int d^2\boldsymbol{\alpha} p(\boldsymbol{\alpha};\, \beta) \langle \text{D}_{1,2}^M(t;\, \boldsymbol{\alpha}) | \hat{O} | \text{D}_{1,2}^M(t;\, \boldsymbol{\alpha}) \rangle. \end{aligned} \tag{33}$$

For the second equality, we have used the multi-D_1 or D_2 Ansatz, $\big|\text{D}_{1,2}^M(t;\, \boldsymbol{\alpha})\big\rangle = e^{-i\hat{H}_{\text{SBM}} t}\big|1\big\rangle\big|\boldsymbol{\alpha}\big\rangle$, and $\big|\text{D}_{1,2}^M(0;\, \boldsymbol{\alpha})\big\rangle$ denotes a trial state with initial bath displacements of $\boldsymbol{\alpha}$ at $t = 0$. For the case of the multi-D_1 Ansatz, initial condition parameters are $A_1(0) = 1$, $B_1(0) = 0$, $A_n(0) = B_n(0) = 0$ for $n \neq 1$ and $f_{nl}(0) = g_{nl}(0) = \alpha_l$ for all n and l. Likewise, initial parameters of the multi-D_2 Ansatz are $A_1(0) = 1$, $B_1(0) = 0$, $A_n(0) = B_n(0) = 0$ for $n \neq 1$ and $f_{nl}(0) = \alpha_l$ for all n and l.

The expectation value of the observable at finite temperature can numerically be calculated by the technique of Monte Carlo importance sampling as

$$\langle \hat{O}(t) \rangle = \frac{1}{N_s} \sum_i^{N_s} \langle \text{D}_{1,2}^M(t;\, \boldsymbol{\alpha}_i) | \hat{O} | \text{D}_{1,2}^M(t;\, \boldsymbol{\alpha}_i) \rangle, \tag{34}$$

where N_s is the sampling number. The configuration $\boldsymbol{\alpha}_i$ for the bath is numerically generated according to $p(\boldsymbol{\alpha};\, \beta)$ by importance sampling, where $p(\boldsymbol{\alpha};\, \beta)$ is the Boltzmann distribution used as the weighting function in the importance sampling procedure. Letting $2\sigma_l^2 = 1/(e^{\beta\omega_l} - 1)$ and $\alpha_l = x_l + ip_l$, $p(\boldsymbol{\alpha};\, \beta)$ in Eq. (32) can be partitioned into two independent Gaussian distribution as

$$p(\boldsymbol{\alpha};\, \beta) = \prod_l^{N_b} \frac{1}{\sqrt{2\pi}\sigma_l} e^{-\frac{x_l^2}{2\sigma_l^2}} \frac{1}{\sqrt{2\pi}\sigma_l} e^{-\frac{p_l^2}{2\sigma_l^2}}, \tag{35}$$

where σ_l can be taken as the variance of the Gaussian distribution. To avoid singularity, boson displacements in the trial states are initialized by setting $f_{nl}(0) = g_{nl}(0) = \alpha_l + \epsilon_0$, where noise ϵ_0 satisfying the uniform distribution $[-10^{-2}, 10^{-2}]$ is added to the variational parameters of the initial states. From the definition of σ_l, a lower temperature or the higher frequency ω_l gives a smaller σ_l. The zero temperature case corresponds to every bath mode being in the ground state initially, and it is equivalent to a coherent state with displacement parameter, $\alpha_l = 0$ for all l. In this case, the observable of Eq. (33) or Eq. (34) reduces to that at zero temperature, $\langle \mathrm{D}^M_{1,2}(t)|\hat{O}|\mathrm{D}^M_{1,2}(t)\rangle$.

4.2 Thermofield Dynamics

The TFD method was introduced in the 1970s to provide a finite temperature representation of quantum mechanics within the wave-function formalism, mostly as an analytical tool [42, 110–112]. It was recognized only recently that TFD can be transformed into a powerful instrument for dynamics simulation of many-body quantum systems at finite temperatures. To achieve that, the TFD machinery must be combined with highly efficient methods of integration of multidimensional Schrödinger equations based, for example, on the tensor-train (TT) [113, 114] or the Davydov Ansätze. The TFD-TT approach and its applications have recently been reviewed in Ref. [115]. In the physics literature, TTs are synonymous to matrix product states (MPS), and TFD-TT is similar to the method of finite-temperature time-dependent density matrix renormalization group (TD-DMRG) [116], which is summarized in Refs. [117, 118]. The approach marrying the Davydov Ansätze to the TFD method has been successfully applied to the Holstein polaron in Ref. [45].

The TFD representation can efficiently be introduced for systems described by so-called vibronic coupling (VC) Hamiltonians, in which diabatic potential energy surfaces are represented by polynomials of nuclear coordinates. The VC representation is commonly used for the construction of *ab initio* Hamiltonians of polyatomic chromophores [119, 120], molecular aggregates [121, 122] and molecular materials [123, 124]. The Hamiltonians of Eqs. (1) and (13) considered in the present work belong to the class of VC Hamiltonians. To introduce the TFD methodology, we follow the presentation of Sec. 4.1 and consider the SBM system at finite temperatures as an example. Systems governed by other VC Hamiltonians can be treated in much the same manner.

The time evolution of the SBM system is specified by the density matrix $\hat{\rho}_{\mathrm{tot}}(t)$ whose time evolution obeys the Liouville – von Neumann equation

$$\partial_t \hat{\rho}_{\mathrm{tot}}(t) = -i[\hat{H}_{\mathrm{SBM}}, \hat{\rho}_{\mathrm{tot}}(t)], \;\; \hat{\rho}_{\mathrm{tot}}(0) = |+\rangle\langle+|\hat{\rho}^{\mathrm{eq}}_{\mathrm{B}}. \tag{36}$$

Following Ref. [125], we introduce the eigenvectors of the bath Hamiltonian, $\hat{H}_{\mathrm{B}}|\boldsymbol{k}\rangle = E_{\boldsymbol{k}}|\boldsymbol{k}\rangle$. Obviously, $|\boldsymbol{k}\rangle = \prod_l |k_l\rangle$ where $E_{\boldsymbol{k}} = \sum_l k_l\omega_l$ and $|k_l\rangle$ are the eigenvectors of the lth phonon mode.

We also define vectors $|\tilde{\boldsymbol{k}}\rangle$ which are a copy of the original vectors $|\boldsymbol{k}\rangle$ but act in a different Hilbert space, the so-called *tilde* space. Using the notation $|\boldsymbol{k}\tilde{\boldsymbol{k}}\rangle = |\boldsymbol{k}\rangle|\tilde{\boldsymbol{k}}\rangle$, we introduce the unity vector $|\boldsymbol{I}\rangle = \sum_{\boldsymbol{k}} |\boldsymbol{k}\tilde{\boldsymbol{k}}\rangle$ and the thermal vacuum state,

$$|\mathbf{0}(\beta)\rangle = \sqrt{\hat{\rho}_{\mathrm{B}}^{\mathrm{eq}}}|\boldsymbol{I}\rangle = Z_{\mathrm{B}}^{-\frac{1}{2}} e^{-\frac{1}{2}\hat{H}_{\mathrm{B}}}|\boldsymbol{I}\rangle, \tag{37}$$

Z_{B} being the partition function. With these definitions, the thermal Boltzmann distribution can be rewritten in the form $\hat{\rho}_{\mathrm{B}}^{\mathrm{eq}} = \mathrm{Tr}_{\tilde{\boldsymbol{k}}}\{|\mathbf{0}(\beta)\rangle\langle\mathbf{0}(\beta)|\}$ where $\mathrm{Tr}_{\tilde{\boldsymbol{k}}}\{...\}$ indicates the trace over the tilde subspace. Let us now consider the Liouville – von Neumann equation

$$\partial_t \hat{\sigma}_{\mathrm{tot}}(t) = -i[\hat{H}_{\mathrm{SBM}}, \hat{\sigma}_{\mathrm{tot}}(t)], \;\; \hat{\sigma}_{\mathrm{tot}}(0) = |+\rangle\langle +||\mathbf{0}(\beta)\rangle\langle\mathbf{0}(\beta)|. \tag{38}$$

Obviously, $\hat{\rho}_{\mathrm{tot}}(t) = \mathrm{Tr}_{\tilde{\boldsymbol{k}}}\{\hat{\sigma}_{\mathrm{tot}}(t)\}$. Furthermore, Eq. (36) in which $\hat{H}_{\mathrm{SBM}} \to \hat{H}_{\mathrm{SBM}} - \tilde{h}$ ($\tilde{h}$ being any operator acting in the tilde subspace only) yields $\hat{\sigma}_{\mathrm{tot}}(t)$ which produces the same $\hat{\rho}_{\mathrm{tot}}(t)$. Since the initial condition of Eq. (38) corresponds to a pure state, we obatin

$$\hat{\sigma}_{\mathrm{tot}}(t) = |\psi(t)\rangle\langle\psi(t)| \tag{39}$$

where the wave function $|\psi(t)\rangle$ obeys the TFD Schrödinger equation

$$\partial_t|\psi(t)\rangle = -i(\hat{H}_{\mathrm{SBM}} - \tilde{h})|\psi(t)\rangle, \;\; |\psi(0)\rangle = |+\rangle|\mathbf{0}(\beta)\rangle. \tag{40}$$

It has thus been demonstrated that the solution of the original Liouville – von Neumann equation (36) is equivalent to the solution of the TFD Schrödinger equation (40).

The key advantage of the TFD method is a compact analytical representation of the thermal vacuum state given by the thermal Bogoliubov transformation

$$e^{-iG}|\mathbf{0}\tilde{\mathbf{0}}\rangle = |\mathbf{0}(\beta)\rangle \tag{41}$$

where $|\mathbf{0}\tilde{\mathbf{0}}\rangle$ is the ground state in the $|\boldsymbol{k}\rangle \otimes |\tilde{\boldsymbol{k}}\rangle$ subspace. Applying the thermal Bogoliubov transformation to Eq. (40), we obtain

$$i\partial_t|\psi_\theta(t)\rangle = \hat{H}^\theta_{\mathrm{SBM}}|\psi_\theta(t)\rangle, \;\; |\psi_\theta(0)\rangle = |+\rangle|\mathbf{0}\tilde{\mathbf{0}}\rangle \tag{42}$$

where $\hat{H}^\theta_{\mathrm{SBM}} = e^{iG}(\hat{H}_{\mathrm{SBM}} - \tilde{h}_v)e^{-iG}$, $|\psi_\theta(t)\rangle = e^{iG}|\psi(t)\rangle$. For thermal vacuum state $|\mathbf{0}(\beta)\rangle$ of Eq. (37), the operator of the thermal Bogoliubov transformation reads [42, 110–112] $G = -i\sum_l \theta_l(b_l\tilde{b}_l - b_l^\dagger\tilde{b}_l^\dagger)$ where $\theta_l = \mathrm{arctanh}(e^{-\beta\omega_l/2})$. For obtaining the explicit form of the transformed Hamiltonian $\hat{H}^\theta_{\mathrm{SBM}}$, it is convenient to choose [115] $\tilde{h} = \sum_l \omega_l \tilde{b}_l^\dagger \tilde{b}_l$. We thus obtain the TFD Schrödinger equation (42) in

which [115]

$$\begin{aligned}
\hat{H}^{\theta}_{\rm SBM} &= \hat{H}^{\theta}_{\rm S} + \hat{H}^{\theta}_{\rm SB} + \hat{H}^{\theta}_{\rm B}, \\
\hat{H}^{\theta}_{\rm S} &= \hat{H}_{\rm S}, \\
\hat{H}^{\theta}_{\rm SB} &= \frac{\sigma_z}{2}\sum_l \lambda_l \left[\cosh(\theta_l)(b_l^\dagger + b_l) + \sinh(\theta_l)(\tilde{b}_l^\dagger + \tilde{b}_l)\right], \\
\hat{H}^{\theta}_{\rm B} &= \sum_l \omega_l \left[b_l^\dagger b_l - \tilde{b}_l^\dagger \tilde{b}_l\right].
\end{aligned} \tag{43}$$

The TFD Schrödinger equation (42) is governed by the TFD Hamiltonian $\hat{H}^{\theta}_{\rm SBM}$ of Eq. (43). It is fully equivalent to the original Liouville – von Neumann equation (36) governed by the Hamiltonian $\hat{H}_{\rm SBM}$. Hence all observables evaluated via Eqs. (42) and (36) are identical. The number of phonon modes in $\hat{H}^{\theta}_{\rm SBM}$ is double of that in the original Hamiltonian $\hat{H}_{\rm SBM}$ of Eq. (13), and electron-phonon couplings in $\hat{H}^{\theta}_{\rm SBM}$ are renormalized by temperature-dependent factors: $\cosh(\theta_l)$ for physical phonon modes and $\sinh(\theta_l)$ for tilde phonon modes. If $T \to 0$ then $\theta_l \to 0$, the coupling to the tilde space disappears, and the standard Schrödinger equation is recovered as expected. Nonzero temperature causes dynamical mixing of the physical (b_l, $b_l^\dagger$) and tilde ($\tilde{b}_l$, $\tilde{b}_l^\dagger$) variables. The number of electronic degrees of freedom in the Hamiltonians of Eqs. (13) and (43) remains unchanged.

It is essential that the TFD Hamiltonian of Eq. (43) has absolutely the same structure as the original SBM Hamiltonian of Eq. (13). Hence the TFD Schrödinger equation (42) can be treated as the usual Schrödinger equation, and all formal derivations (e.g. those based on time-dependent perturbation theory) remain unaffected. Furthermore, all variants of the Davydov Ansatz methods used for the solution of Schrödinger equations at zero temperature are directly applicable to the solution of TFD Schrödinger equations at final temperatures.

4.3 Displaced Number States

Another approach to introduce temperature effects in the time evolution of many-body quantum dynamics using the multi-D_2 Ansatz is based on the displaced number states, thanks to the fact that initial excitation of the vibrational manifold in the system can be conveniently described by displaced number states of the bath degrees of freedom.

The multi-D_2 Ansatz of multiplicity M for the displaced number state is given by [50, 51]

$$|{\rm D}_2^{\vec{n},M}(t)\rangle = \sum_m |m\rangle \sum_{k=1}^{M} A^{\vec{n}}_{m,k}(t) e^{\left(\sum_q f^{\vec{n}}_{kq}(t) b_q^\dagger - H.c.\right)} |\vec{n}\rangle,$$

which can be used to include temperature effects. Here $|\vec{n}\rangle = |n_1 n_2 \cdots n_w\rangle$ and $|m\rangle$ denotes diabatic electronic states. The time-dependent variational parameters $\vec{\mu} = \{A^{\vec{n}}_{mk}(t), f^{n_q}_{kq}(t)\}$ can be derived from the time-dependent variational principle via the construction of the corresponding Lagrangian.

Two ways to proceed are available in the context of using displaced number states. The first is to derive relatively complex equations of motion that depend on the initial excitation state index but have trivial initial conditions, while the second is to expand the initially excited oscillator number states in terms of coherent states, then to obtain the standard equations of motion but with nontrivial initial conditions that have to be sampled along a circle in the phase space. It turns out that the latter that greatly alleviates numerics is preferable, which will be described in detail in this subsection.

It is well known that the number state $|n_l\rangle$ of the harmonic oscillator can be expanded in terms of coherent states [50], which becomes

$$|n_l\rangle = \frac{1}{2\pi}\sqrt{\frac{n_l! e^{|\beta_l|^2}}{|\beta_l|^{2n_l}}}\int_{-\pi}^{\pi} d\theta_l e^{-in_l\theta_l}||\beta_l|e^{i\theta_l}\rangle. \tag{44}$$

To discretize the integral over θ_l, we adopt the approximate expression

$$|n_l\rangle \approx \sqrt{\frac{n_l! e^{|\beta_l|^2}}{|\beta_l|^{2n_l}}}\frac{1}{N}\sum_{k_l=0}^{N-1} e^{-in_l\theta_{k_l}}||\beta_l|e^{i\theta_{k_l}}\rangle, \tag{45}$$

where $\theta_{k_l} = -\pi + \frac{2\pi}{N}k_l$ and $k_l = 0, ..., N-1$.

Following Werther *et al.* [50], for the Davydov D_2 Ansatz with multiplicity $M \geq N^w$ (w is the number of modes that may be excited), the initial conditions with the w phonon modes read

$$A^{\vec{n}}_{m,k}(0) = \begin{cases} \prod_l \mathcal{N}(\beta_l)\exp(-in_l\theta_{k_l}), & 1 \leq k \leq N^w. \\ 0, & \text{else.} \end{cases} \tag{46}$$

$$A^{\vec{n}}_{m',k}(0) = 0, (\text{for } \ m' \neq m). \tag{47}$$

$$f^{n_l}_{kl}(0) = \begin{cases} |\beta_l|\exp(i\theta_{k_l}), & 1 \leq k \leq N^w. \\ 0, & \text{else,} \end{cases} \tag{48}$$

where $\mathcal{N}(\beta_l) = \frac{1}{N}\sqrt{\frac{(n_l!)e^{\beta_l^2}}{|\beta_l|^{2n_l}}}$. The convergence with respect to the number of sampling points N on the circle of radius $|\beta_l| = \sqrt{n_l}$ can be quickly obtained, for example, in Ref. [102], for N between 5 and 14 depending on various initial excitations n. The value of best performance $|\beta_l| = \sqrt{n_l}$ is often adopted in simulations. As a demonstration, the phase-space initial conditions are plotted in Fig. 2 with 12 coherent states evenly distributed on a circle of radius $|\beta_l| = \sqrt{n_l}$.

The time-dependent diabatic population of the electronic state $|\mathrm{m}\rangle$ for the number state $|\vec{n}\rangle$ can be written as

$$P^{\vec{n}}_m = \sum_k^M \sum_{k'}^M A^{\vec{n}*}_{m,k}(t) A^{\vec{n}}_{m,k'}(t) S^{\vec{n}}_{kk'},$$

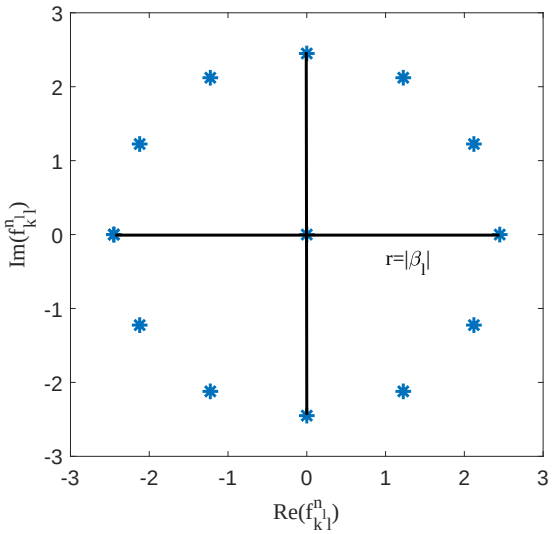

Figure 2: Initial conditions in the phase space of $f_{kl}^{n_l}$ for $N = 12$ and $n_l = 6$ with $k > N$. 12 coherent states are distributed on the circle with the radius $|\beta_l| = \sqrt{n_l}$, and the rest expansion coefficients are set as zero initially.

where the Debye-Waller factor is given by

$$S_{kk'}^{\vec{n}} = \exp\left(\sum_q \left\{-\left(\left|f_{kq}^{n_q}\right|^2 + \left|f_{k'q}^{n_q}\right|^2\right)/2 + f_{kq}^{n_q *} f_{k'q}^{n_q}\right\}\right). \tag{49}$$

Then we adopt the Boltzmann-averaged method to calculate the observable from

$$P_m^B = \prod_l \sum_{n_l=0}^{N_{l,T}} \frac{e^{-\beta n_l \omega_l}}{Q_\beta} P_m^{\vec{n}},$$

where

$$Q_\beta = \prod_l \sum_{n_l=0}^{\infty} e^{-\beta n_l \omega_l} \tag{50}$$

is the canonical partition function. The truncated number of the lth phonon mode excitation $N_{l,T}$ yielding converged numerical results is determined by the temperature and the total phonon excitation energy.

The method of displaced number states in the multi-D_2 Ansatz can provide efficient, quantitative descriptions of nonadiabatic dynamics at conical intersections in chemical reactions and beyond [51]. Based on many-body wave functions, the multiple Davydov Ansatz is nonperturbative, numerically exact if provided sufficiently large multiplicities of the trial states, capable to compute nonlinear spectroscopic responses for close comparisons with experiment [51, 126].

5 Spectral simulation via Davydov's Ansätze

Optical spectroscopy is another important aspect in the dynamics investigation of various exciton-phonon systems including the Holstein molecular crystal model, as it provides valuable information on a variety of correlation functions [127, 128]. First of all, linear absorption spectra $F(\omega)$ calculated on the basis of Davydov's Ansätze are comprehensively studied to validate these trial wave functions in parameter regimes of interest [27, 52, 53, 129]. The autocorrelation function $F(t)$ based on the multi-D_2 ansatze is defined by

$$F(t) =_{\rm ph} \langle 0|_{\rm ex}\langle 0|e^{iHt}Pe^{-iHt}P^\dagger|0\rangle_{\rm ex}|0\rangle_{\rm ph} =_{\rm ph} \langle 0|_{\rm ex}\langle 0|Pe^{-iHt}P^\dagger|0\rangle_{\rm ex}|0\rangle_{\rm ph}, \tag{51}$$

where $P = \mu\sum_n(|n\rangle_{\rm ex\ ex}\langle 0| + |0\rangle_{\rm ex\ ex}\langle n|)$ is the polarization operator. The linear absorption spectra can be obtained by the Fourier transformation of the autocorrelation function, which reads

$$F(\omega) = \frac{1}{\pi}{\rm Re}\int_0^\infty F(t)e^{i\omega t}dt. \tag{52}$$

In addition to the information provided by the linear absorption spectra, 2D photon echo (PE) spectra provide direct knowledge on exciton-exciton interactions and on the dephasing and relaxation processes that is elusive in the output from the traditional 1D spectroscopy. In order to simulate the 2D PE spectra, we have to consider the interaction between the system and the light field. The corresponding Hamiltonian is given by $\hat{H}_{\rm L} = -\left(\mathbf{E}\left(\mathbf{r},t\right)\cdot\hat{\mu}_+ + \mathbf{E}^*\left(\mathbf{r},t\right)\cdot\hat{\mu}_-\right)$, with $\mathbf{E}(r,t)$ being the time-dependent electric field of the applied pulse sequence,

$$\begin{aligned}
\mathbf{E}\left(\mathbf{r},t\right) &= \mathbf{E}_1\left(\mathbf{r},t\right) + \mathbf{E}_2\left(\mathbf{r},t\right) + \mathbf{E}_3\left(\mathbf{r},t\right),\\
\mathbf{E}_1\left(\mathbf{r},t\right) &= \mathbf{e}_1E_1\left(t-\tau_1\right)e^{i\mathbf{k}_1\cdot\mathbf{r}-i\omega_1t+i\phi_1},\\
\mathbf{E}_2\left(\mathbf{r},t\right) &= \mathbf{e}_2E_2\left(t-\tau_2\right)e^{i\mathbf{k}_2\cdot\mathbf{r}-i\omega_2t+i\phi_2},\\
\mathbf{E}_3\left(\mathbf{r},t\right) &= \mathbf{e}_3E_3\left(t-\tau_3\right)e^{i\mathbf{k}_3\cdot\mathbf{r}-i\omega_3t+i\phi_3},
\end{aligned} \tag{53}$$

where $\mathbf{e}_a$, k_a, ω_a, $E_a\left(t\right)$, and $\phi_a\left(a=1,2,3\right)$ denote the polarization, the wave vector, the frequency, the dimensionless envelope, and the initial phase, respectively [4, 58]. It is common to define the pulse arrival times in $\hat{H}_{\rm L}$ as $\tau_1 = -T_w - \tau$, $\tau_2 = -T_w$, $\tau_3 = 0$ where τ (the so-called coherence time) is the delay time between the second and the first pulse, and T_w (the so-called population time) is the delay time between third and second pulse. In the short pulse limit, we have $E_a\left(t\right) = E_0\delta\left(t\right)$. Before the optical excitation ($t \ll -T-\tau$), the system is assumed to be in its global ground state $|g\rangle\,|0\rangle_{\rm ph}$. Adopting this factorized initial condition allows one to neglect correlations between the primary system and its environment. Without the contribution of excited-state absorption, the PE

third polarization $P^{(3)}(t)$ can be decomposed into four nonlinear response functions R_{1-4}, which form the theoretical bases for the simulations of different 2D spectra [4, 6]. The third-order response is directly given by the response functions in the impulsive limit, which can be expressed through the Multi-D_2 parameters in Eq. (18) as follows [27, 51, 58, 103]

$$\begin{aligned}
R_1(\tau,T_w,t) &= \sum_{i,j}^{M}\sum_{n,n_1,n_2,n_3}(\mathbf{e}_4^*\cdot\boldsymbol{\mu}_{n_2}^*)(\mathbf{e}_1\cdot\boldsymbol{\mu}_{n_3})(\mathbf{e}_2^*\cdot\boldsymbol{\mu}_n^*)(\mathbf{e}_3\cdot\boldsymbol{\mu}_{n_1})\\
&\quad\times A^*_{jn_1n}(T_w)A_{in_2n_3}(\tau+T_w+t)e^{\sum_q f^*_{jqn}(T_w)f_{iqn_3}(\tau+T_w+t)e^{i\omega_q t}}\\
&\quad\times e^{-\frac{1}{2}\sum_q(|f_{jqn}(T_w)|^2+|f_{iqn_3}(\tau+T_w+t)|^2)},\\
R_2(\tau,T_w,t) &= \sum_{i,j}^{M}\sum_{n,n_1,n_2,n_3}(\mathbf{e}_4^*\cdot\boldsymbol{\mu}_{n_2}^*)(\mathbf{e}_1^*\cdot\boldsymbol{\mu}_n^*)(\mathbf{e}_2\cdot\boldsymbol{\mu}_{n_3})(\mathbf{e}_3\cdot\boldsymbol{\mu}_{n_1})\\
&\quad\times A^*_{jn_1n}(\tau+T_w)A_{in_2n_3}(T_w+t)e^{\sum_q f^*_{jqn}(\tau+T_w)f_{iqn_3}(T_w+t)e^{i\omega_q t}}\\
&\quad\times e^{-\frac{1}{2}\sum_q(|f_{jqn}(\tau+T_w)|^2+|f_{iqn_3}(T_w+t)|^2)},\\
R_3(\tau,T_w,t) &= \sum_{i,j}^{M}\sum_{n,n_1,n_2,n_3}(\mathbf{e}_4^*\cdot\boldsymbol{\mu}_{n_2}^*)(\mathbf{e}_1^*\cdot\boldsymbol{\mu}_n^*)(\mathbf{e}_2\cdot\boldsymbol{\mu}_{n_1})(\mathbf{e}_3\cdot\boldsymbol{\mu}_{n_3})\\
&\quad\times A^*_{jn_1n}(\tau)A_{in_2n_3}(t)e^{\sum_q f^*_{jqn}(\tau)f_{iqn_3}(t)e^{i\omega_q(T_w+t)}}\\
&\quad\times e^{-\frac{1}{2}\sum_q(|f_{jqn}(\tau)|^2+|f_{iqn_3}(t)|^2)},\\
R_4(\tau,T_w,t) &= \sum_{i,j}^{M}\sum_{n,n_1,n_2,n_3}(\mathbf{e}_4^*\cdot\boldsymbol{\mu}_n^*)(\mathbf{e}_1^*\cdot\boldsymbol{\mu}_{n_3}^*)(\mathbf{e}_2\cdot\boldsymbol{\mu}_{n_2})(\mathbf{e}_3\cdot\boldsymbol{\mu}_{n_1})\\
&\quad\times A^*_{jn_1n}(-t)A_{in_2n_3}(\tau)e^{\sum_q f^*_{jqn}(-t)f_{iqn_3}(\tau)e^{-i\omega_q T_w}}\\
&\quad\times e^{-\frac{1}{2}\sum_q(|f_{jqn}(-t)|^2+|f_{iqn_3}(\tau)|^2)}.
\end{aligned}\tag{54}$$

Here $\mathbf{e}_4$ refers to the polarization of the local oscillator field, and $\boldsymbol{\mu}_n$ are the transition dipole moment vectors. $A^*_{jn_1n}(t)$ represents the probability amplitude at time t for the exciton at the state $|n_1\rangle$ with the initial state $|n\rangle$ and multiplicity j, and $f_{jqn}(t)$ is the corresponding phonon displacement, also starting from $|n\rangle\exp\left\{\sum_q^{N_q}\left[f_{jq}(0)\hat{b}_q^\dagger - f^*_{jq}(0)\hat{b}_q\right]\right\}|\mathbf{0}\rangle_{\rm ph}$.

Similarly, the higher excited-state response functions are given by [58, 126]

$$
\begin{aligned}
R_1^*(\tau,T_w,t) &= \sum_{i,j}^{M}\sum_{\substack{nn_1n_2\\ n_3m}} (\mathbf{e}_4^*\cdot\boldsymbol{\mu}_{n_1m}^*)(\mathbf{e}_1^*\cdot\boldsymbol{\mu}_n^*)(\mathbf{e}_2\cdot\boldsymbol{\mu}_{n_3})(\mathbf{e}_3\cdot\boldsymbol{\mu}_{n_2m}) \\
&\quad A^{j*}_{m(n_1n)}(0)A^{i}_{m(n_2n_3)}(t)e^{\sum_q f^{j*}_{m(n_1n),q}(0)f^{i}_{m(n_2n_3),q}(t)}e^{-\frac{1}{2}\sum_q(|f^{j*}_{m(n_1n),q}(0)|^2+|f^{i}_{m(n_2n_3),q}(t)|^2)}, \\
R_2^*(\tau,T_w,t) &= \sum_{i,j}^{M}\sum_{\substack{nn_1n_2\\ n_3m}} (\mathbf{e}_4^*\cdot\boldsymbol{\mu}_{n_1m}^*)(\mathbf{e}_1\cdot\boldsymbol{\mu}_{n_3})(\mathbf{e}_2^*\cdot\boldsymbol{\mu}_n^*)(\mathbf{e}_3\cdot\boldsymbol{\mu}_{n_2m}) \\
&\quad A^{j\prime*}_{m(n_1n)}(0)A^{i\prime}_{m(n_2n_3)}(t)e^{\sum_q f^{j\prime*}_{m(n_1n),q}(0)f^{i\prime}_{m(n_2n_3),q}(t)}e^{-\frac{1}{2}\sum_q(|f^{j\prime*}_{m(n_1n),q}(0)|^2+|f^{i\prime}_{m(n_2n_3),q}(t)|^2)}.
\end{aligned}
$$

The initial amplitudes of the higher excited-state are $A^{j*}_{m(n_1n)}(0)=A^*_{jn_1n}(\tau+T_w+t)$, $A^{i}_{m(n_2n_3)}(0)=A_{in_2n_3}(T_w)$, $A^{j\prime*}_{m(n_1n)}(0)=A^*_{jn_1n}(t+T_w)$, and $A^{i\prime}_{m(n_2n_3)}(0)=A_{in_2n_3}(\tau+T_w)$, and the corresponding phonon displacements are $f^{j*}_{m(n_1n),q}(0)=f^*_{jn_1q}(\tau+T_w+t)$, $f^{i}_{m(n_2n_3),q}(0)=f_{in_2q}(T_w)$, $f^{j\prime*}_{m(n_1n),q}(0)=f^*_{jn_1q}(t+T_w)$, and $f^{i\prime}_{f(n_2n_3),q}(0)=f_{in_2q}(\tau+T_w)$.

The contributions from stimulated emission, ground-state bleach, and excited-state absorption, are expressed, respectively, as [4, 6],

$$
\begin{aligned}
S_{\rm SE}(\omega_\tau,T_w,\omega_t) &= \Re\int_0^\infty\int_0^\infty dtd\tau[R_2(\tau,T_w,t)e^{-i\omega_\tau\tau+i\omega_t t}+R_4(\tau,T_w,t)e^{i\omega_\tau\tau+i\omega_t t}] \\
S_{\rm GSB}(\omega_\tau,T_w,\omega_t) &= \Re\int_0^\infty\int_0^\infty dtd\tau[R_3(\tau,T_w,t)e^{-i\omega_\tau\tau+i\omega_t t}+R_1(\tau,T_w,t)e^{i\omega_\tau\tau+i\omega_t t}] \\
S_{\rm ESA}(\omega_\tau,T_w,\omega_t) &= -\Re\int_0^\infty\int_0^\infty dtd\tau[R_1^*(\tau,T_w,t)e^{-i\omega_\tau\tau+i\omega_t t}+R_2^*(\tau,T_w,t)e^{i\omega_\tau\tau+i\omega_t t}] \qquad (55)
\end{aligned}
$$

The correlated 2D spectrum is given by the sum of the three contributions

$$
S(\omega_\tau,T_w,\omega_t)=S_{\rm SE}(\omega_\tau,T_w,\omega_t)+S_{\rm GSB}(\omega_\tau,T_w,\omega_t)+S_{\rm ESA}(\omega_\tau,T_w,\omega_t). \qquad (56)
$$

In summary, both singly and doubly excited excitonic states can be treated in the formalism of Davydov's Ansätze, handling nicely the contributions due to stimulated emission, ground state bleach, and excited state absorption. As an illustration, a series of optical 2D spectra of a model J-aggregate have been simulated, and their waiting-time dependence is plotted in Fig. 3. The relevant parameters, such as the site-independent nearest-neighbor transfer integral ($J=0.1$), the attractive inter-exciton coupling ($K=-0.2$), the Huang-Rhys factor ($S=2$), and the narrow bandwidth ($W=0.1$), are adopted in the simulation. The spectra exhibit a pronounced vibrational structure. Coexistence of positive and negative peaks is a result of the delicate balance between the GSB and SE on the one hand and the ESA on the other. A slight redshift of the peaks relative to their positions at $j\omega_0$, $j=0,\pm1,\ldots$ is due to the inter-exciton coupling. Computationally efficient, the Davydov-Ansatz approach is suitable for the computation of femtosecond optical four-wave-mixing signals

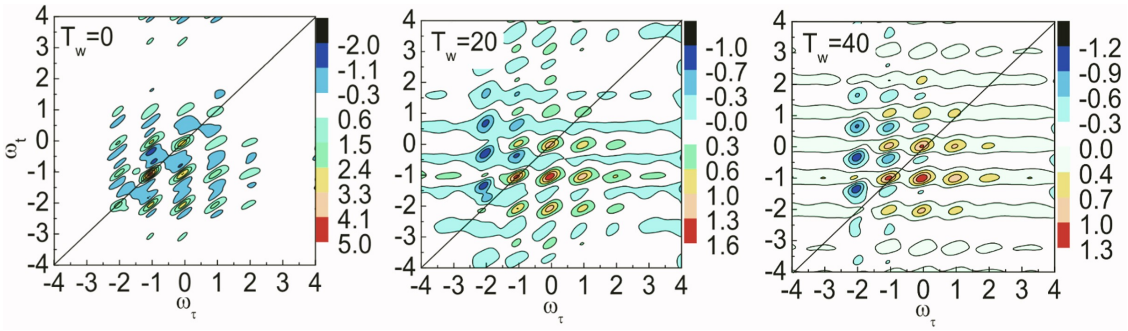

Figure 3: Waiting-time (T_w) dependence of 2D spectra $S(\omega_\tau, T_w, \omega_t)$ which is calculated for a molecular ring with nearest-neighbor transfer integral $J = 0.1$, attractive inter-exciton coupling $K = -0.2$, Huang-Rhys factor $S = 2$, and bandwidth $W = 0.1$. The spectra include contributions from stimulated emission, ground state bleach, and excited state absorption.

of molecular aggregates with intermediate-to-strong exciton-phonon and exciton-exciton coupling strengths. The effect of inhomogeneous broadening can be accounted for by performing a series of simulations at slightly different system parameters.

6 Applications of Davydov's Ansätze

6.1 The spin-boson model and its variants

Popularized chiefly by Anthony Leggett, the SBM has become a paradigm for the study of a two-state system coupled to a dissipative environment [130]. In this section, we attempt to summarize a few recent applications of the HDA machinery to both the ground-state properties and the dynamics of the SBM and its variants, such as the SBM in a high-Q cavity, the sinusoidally driven SBM, the two-bath SBM, and the two-spin SBM.

6.1.1 The traditional spin-boson model

Despite much attention devoted to the paradigmatic SBM, a consensus on the dynamics of the Hamiltonian of Eq. (13) in much of the SBM phase diagram has yet to emerge. With the help of the multi-D_1 Ansatz and the Monte Carlo importance sampling scheme discussed in Sec. 4.1, a sketch of the dynamics phase diagram of SBM has been produced and shown schematically in Figs. 4 (a) and (b). The spectral density form $J(\omega) = 2\alpha\omega_c^{1-s}\omega^s e^{-\omega/\omega_c}$ is adopted, where α represents the coupling strength, ω_c provides a phenomenological frequency cutoff, and s determines the dependence of $J(\omega)$ on the bath frequency ω. The spin bias ϵ and the tunneling constant Δ are set to zero and one tenth

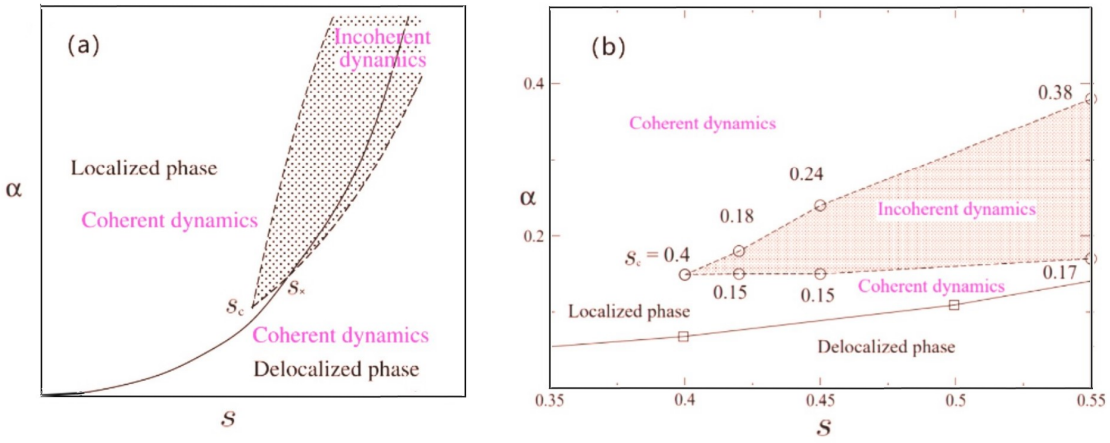

Figure 4: (a) Sketch of the SBM phase diagram. The solid line which is the critical line of the localized-delocalized phase transition, partitions the domain into the delocalized (below) and the localized (above) phase. The two dashed lines are coherent-incoherent crossover lines. The lower crossover line intersects with the phase transition line at $s_\times$ and the two crossover lines meet at the critical point s_c. s_c separates the interval into two parts. For $s_c < s < 1$, the two dashed line separate the domain into three parts. The shaded area corresponds to the incoherent state and the other two are in the coherent state. For $s < s_c$, there is only coherent state. (b) The phase diagram of the dynamical coherent-incoherent crossover near the critical point s_c obtained by the multi-D_1 Ansatz. The critical point $s_c = 0.4$ is estimated by the extrapolation. The domain spanned by s and α is separated by the dashed lines of the coherent-incoherent crossover. The shaded area is the incoherent phase. The solid line with square symbols is the localized-delocalized phase transition line. For both panels, the spin bias ϵ and the tunneling constant Δ are set to zero and $\omega_c/10$, respectively.

of ω_c, respectively. It is believed that for $s \leq 1$, with increasing coupling strength α, a dynamical coherent-incoherent crossover takes place first, followed by a delocalized-to-localized transition at a larger α, as revealed by the ML-MCTDH approach and the quantum master equation techniques [131–134]. As shown in Figs. 4 (a) and (b), two transition lines meet at a critical exponent s_c, partitioning the plane into three parts for $s > s_c$. The shaded area corresponds to the incoherent phase, and the rest of domain belongs to the coherent phase. The solid line in Fig. 4 (a) depicts the localized-delocalized phase transition and intersects with the coherent-incoherent transition line at an exponent point $s_\times$ larger than s_c. For the sub-Ohmic dephasing fluctuations case, a similar phase diagram is obtained by analyzing the response function [135].

More accurately, using the multi-D_1 Ansatz and extrapolation [54], we estimate $s_c \approx 0.4$, as shown in Fig. 4 (b) in which the multi-D_2 results are at variance with those obtained with the non-interacting blip approximation (NIBA) method [136]. From the NIBA method, $s_c = s_\times = 0.5$ is obtained [136], and the coherence does not recur in the strong coupling regime, leading to the nonexistence of the

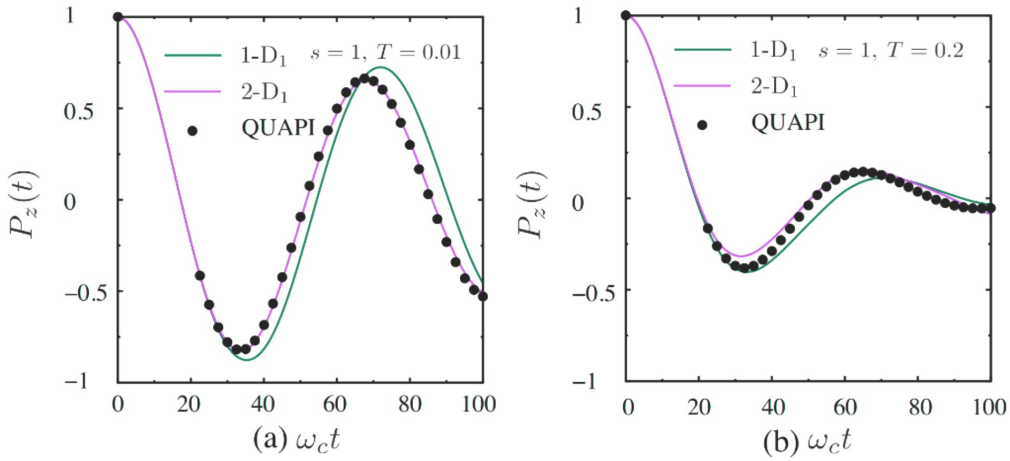

Figure 5: Time evolution of $P_z(t)$ calculated by the multi-D_1 Ansätze (solid lines) with $M = 1$ (1-D_1, green) and $M = 2$ (2-D_1, purple) and the QUAPI approach (black circles) for $s = 1$ and two temperatures, $T/\omega_c = 0.01$ and 0.2. The factorized bath initial condition is employed. The number of the discrete bath mode is $N_b = 250$. The number of samples for the $D_1^{M=1}$ (1-D_1) and $D_1^{M=2}$ (2-D_1) Ansatz is $N_s = 400$ in both panels. Other parameters in Eq. (13) are fixed to be $\epsilon = 0$, Δ=0.1, $\alpha = 0.05$.

upper boundary of the shaded area in Fig. 4 (b). This discrepancy in the phase diagram between the two methods may be due to the approximation employed in the NIBA method. It is conjectured that for $s < s_c$, the coherent-incoherent crossover has larger α than the localized-delocalized phase transition [137]. Recently, real-time path integral Monte Carlo (PIMC) techniques show that below the critical point s_c, the nonequilibrium coherent dynamics can persist even under strong dissipation [136]. Reliable algorithms are needed to probe the dynamics accurately in the both weak and strong coupling regime.

In Fig. 5, dynamics obtained by both the $D_1^{M=2}$ Ansatz and the QUAPI approach agree with each other at high temperature ($k_B T/\omega_c = 0.2$) despite a tiny difference between the $D_1^{M=2}$ Ansatz and QUAPI populations, which may be attributed to insufficient number of bath modes in the variational method. From Eq. (35) and the definition of the variance of the Gaussian distribution σ_l, the value of σ_l becomes large at high temperature. The increase of σ_l leads to large values of $f_{nl}(0)$ and $g_{nl}(0)$ even for high-frequency modes that can be safely ignored at low temperatures. Therefore, the number N_b of bath modes required as well as the sampling number become large due to large value of σ_l at high temperatures. The accuracy of the single D_2 Ansatz ($M = 1$) at high temperatures is improved significantly relative to that in the low temperature regime, and are similar to that of the $D_1^{M=2}$ Ansatz. The increased computational cost due to additional bath modes and extended sampling is offset by the reduced Ansatz multiplicity, and thus the variational approach

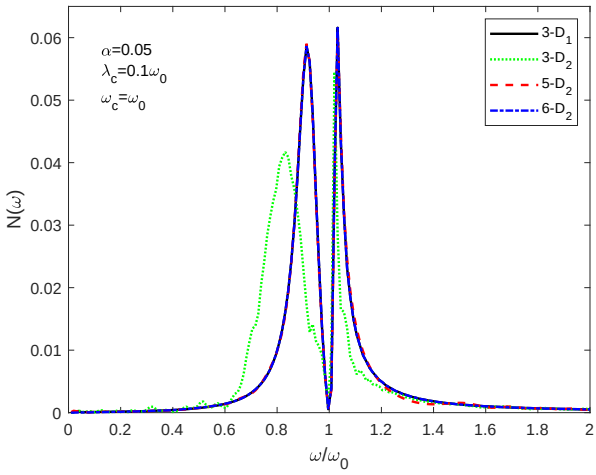

Figure 6: Comparison of emission spectra calculated with the multi-D_1 (M= 3, or 3-D_1) Ansatz and the multi-D_2 ($M = 3, 5$ and 6, or 3-, 5-, 6-D_2) Ansatz.

with importance sampling remains efficient even at high temperatures.

6.1.2 Vacuum Rabi splitting in a dissipative bath

We consider a qubit coupled to a high-Q cavity and a radiation reservoir, which is described by

$$\hat{H}_{\rm VRS} = \frac{1}{2}\omega_0\sigma_z + \omega_c b_c^\dagger b_c + \frac{\lambda_c}{2}(b_c + b_c^\dagger)\sigma_x + \sum_k \omega_k b_k^\dagger b_k + \sum_k \frac{\lambda_k}{2}(b_k + b_k^\dagger)\sigma_x, \tag{57}$$

where ω_0 is the qubit transition frequency, σ_i ($i = x, y, z$) denotes the Pauli matrices, b_c ($b_c^\dagger$) is the annihilation (creation) operator of the cavity mode of frequency ω_c, b_k ($b_k^\dagger$) is the annihilation (creation) operator of the reservoir mode of frequency ω_k, λ_c and λ_k are the cavity- and reservoir-qubit coupling constants, respectively. The spectral density is assumed to be

$$J(\omega) = \sum_k \lambda_k^2 \delta(\omega_k - \omega) = 2\alpha\omega \exp(-\omega/\omega_{\rm cut}), \tag{58}$$

where α is the dimensionless coupling constant and $\omega_{\rm cut}$ is the cut-off frequency. In this setup, the vacuum Rabi splitting is clearly visible in the emission spectrum, as shown in Fig. 6. The emission spectrum has been calculated using the multi-D_1 and multi-D_2 Ansätze with various multiplicities, and the outcomes are compared in Fig. 6. One readily notes that the 3-D_1 result coincides with the 6-D_2 result, which seems to confirm that the multi-D_1 state with the multiplicity M is a special case of the multi-D_2 states with the multiplicity $2M$ [50].

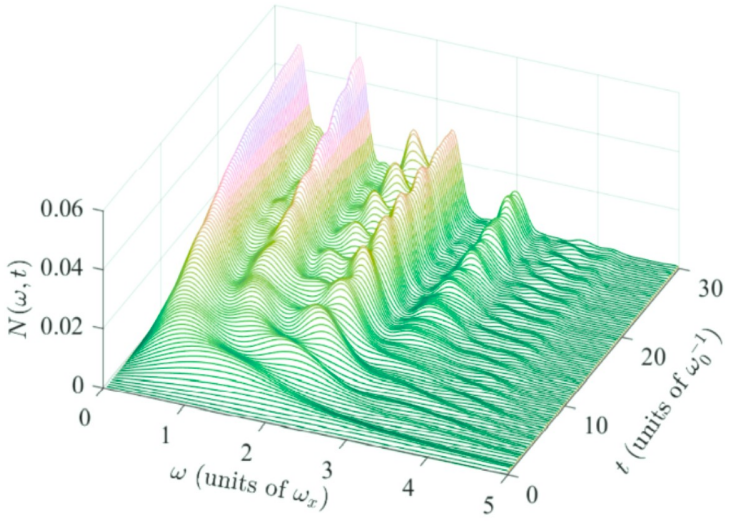

Figure 7: Time-dependent fluorescence spectrum versus frequency ω and time t from the multi-D_1 result for $\alpha = 0.1$, $\omega_0 = 0.2\omega_c$, $\omega_x = \omega_0$, and $\Omega = 1.5\omega_0$ with $N_b = 150$ and $M = 15$.

6.1.3 The driven spin-boson model

The multi-D_1 approach can also be applied to the driven SBM problem [106]:

$$H(t) = H_{\rm S}(t) + H_{\rm R} + H_{\rm SR}, \tag{59}$$

where $H_{\rm S}(t)$ describes the driven qubit:

$$H_{\rm S}(t) = \frac{1}{2}\omega_0\sigma_z + \Omega\cos(\omega_x t)\sigma_x \tag{60}$$

ω_0 is the transition frequency between the two levels of the qubit and $\sigma_{z,x}$ are the Pauli matrices. Ω is the Rabi frequency and ω_x is the driving frequency. $H_{\rm R}$ is the reservoir Hamiltonian given by $H_{\rm R} = \sum_{k=1}^{N_b}\omega_k b_k^\dagger b_k$, with b_k ($b_k^\dagger$) the annihilation (creation) operator of the kth bosonic mode and N_b the mode number. $H_{\rm SR}$ describes the interaction between the qubit and the reservoir and takes the form

$$H_{\rm SR} = \sigma_x/2\sum_{k=1}^{N_b}\lambda_k(b_k + b_k^\dagger), \tag{61}$$

where λ_k is the coupling strength between the kth mode and qubit. The interaction between the qubit and reservoir is characterized by the Ohmic spectral density

$$J(\omega) = \sum_{k=1}^{N_b}\lambda_k^2\delta(\omega - \omega_k) = 2\alpha\omega\Theta(\omega_c - \omega), \tag{62}$$

where α is a dimensionless coupling strength, ω_c is the cut-off frequency, and $\Theta(\cdot)$ is the Heaviside step function. The advantage of this approach is that it allows us to compute not only the reduced

dynamics but also the bosonic field dynamics. For exemple, we calculate time evolution of bosonic population at each mode of radiation reservoir, which can be used to characterize the time-resolved fluorescence spectrum. In Fig. 7, we display the photon number distribution versus emission frequency and time, which clearly reveals the formation of emission peaks [106].

6.1.4 The two-bath spin-boson model

The multi-D_1 Ansatz can be employed to study the two-bath spin-boson model described by

$$\hat{H}_{\rm SBM}^{2-\rm bath} = \frac{\varepsilon}{2}\sigma_z - \frac{\Delta}{2}\sigma_x + \sum_{l,i}\omega_l b_{l,i}^\dagger b_{l,i} + \frac{\sigma_z}{2}\sum_l \lambda_l(b_{l,1}^\dagger + b_{l,1}) + \frac{\sigma_x}{2}\sum_l \phi_l(b_{l,2}^\dagger + b_{l,2}), \tag{63}$$

where ε and Δ is the spin bias and tunneling constant, respectively, $i = 1, 2$ is the index of the baths, and λ_l (ϕ_l) is the diagonal (off-diagonal) coupling strength. In order to investigate quantum phase transitions, we focus on the case of $\varepsilon = \Delta = 0$. A logarithmic discretization procedure is adopted by dividing the phonon frequency domain $[0, \omega_c]$ into L intervals $\omega_c[\Lambda^{-l}, \Lambda^{-(l-1)}]$ ($l = 1, 2, \ldots, L$) [138]. The coupling strengthes ω_l and λ_l (or ϕ_l) in Eq. (63) can then be calculated as

$$\lambda_l^2 = \int_{\Lambda^{-l-1}\omega_c}^{\Lambda^{-l}\omega_c} dt J(t), \quad \omega_l = \lambda_l^{-2}\int_{\Lambda^{-l-1}\omega_c}^{\Lambda^{-l}\omega_c} dt J(t)t, \tag{64}$$

For convenience, the frequency cutoff $\omega_c = 1$ and the discretization factor $\Lambda = 2$ are set. It should be noted that infinite bath modes are considered via the integration of the continuous spectral density $J(\omega)$, although the number of effective bath modes L is finite.

A number of studies have investigated extensions of the standard spin-boson model, for example, to a two-spin system involving a common bath [139, 140] or two independent baths [141], and to a single spin coupled to a bath with simultaneous diagonal and off-diagonal coupling [142]. The two-bath spin-boson model has also been recently studied by Zhao *et al.* [85, 143, 144], yielding a phase diagram that is displayed schematically in Fig. 8(b). The arrow in Fig. 8(a) represents a spin, and X and Z denote the diagonal and off-diagonal coupling, respectively. The bath spectral densities can be described by $J_z(\omega) = 2\alpha\omega_c^{1-s}\omega^s$, $J_x(\omega) = 2\beta\omega_c^{1-\bar{s}}\omega^{\bar{s}}$, where α and β are the dimensionless coupling strengths, and s and $\bar{s}$ denote the spectral exponents characterizing the two baths coupled to the spin diagonally and off-diagonally, respectively. Possible realizations of such two-bath model include impurities in a magnet coupled to two spin-wave modes or two sources of dissipation [145–148], excitonic energy transfer processes in natural and artificial light-harvesting systems [149], electromagnetic fluctuations of two linear circuits attached to a superconducting qubit [150–152], two cavity fields coupled to a SQUID-based charge qubit [153], and the process of thermal transport between two reservoirs coupled with a molecular junction [154].

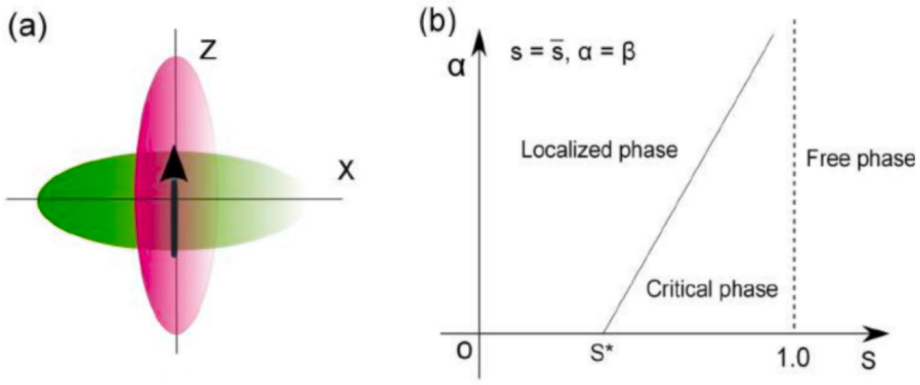

Figure 8: (a) Schematic of the two-bath spin-boson model. A single spin is immersed in two independent baths with simultaneous diagonal coupling (Z) and off-diagonal coupling (X). (b) Schematic plot of the phase diagram of the spin-boson model with two identical bosonic baths $s = \bar{s}$ and $\alpha = \beta$. Where s ($\bar{s}$) and α (β) represent the spectral exponents and coupling strengths, respectively, for the spectral density functions $J_z(\omega)$ ($J_x(\omega)$). Three different phases (localized, critical and free) are displayed in the α-s plane with two critical values of the spectral exponents, s^* and 1.0.

In the two-bath model with $s = \bar{s}$, $\alpha = \beta$, studies based on the perturbative renormalization group theory predict the presence of three phases, namely, the "localized phase," the "critical phase" and the "free phase", in the absence of bias and tunneling [146, 155, 156]. This prediction has been further confirmed numerically in the strong, the intermediate, and the weak coupling regime [157]. A continuous quantum phase transition separating the localized phase from the critical phase was claimed to exist only for the spectral exponent $s^* < s < 1$, and a critical value of the spectral exponent, $s^* = 0.75$, was estimated from DMRG calculations. When $s > 1$, the impurity behaves as a free spin in the so-called free phase [157]. The phase boundary was determined from the response to the external field (i.e., the bias or tunneling) perpendicular to the bath plane. However, the localized-to-delocalized phase transition will occur under the external field, which renders the phase diagram rather complex. Moreover, the critical value of the spectral exponent was predicted by a recent mean-field analysis [85] to $s^* = 1/2$, that stands at variance to the aforementioned DMRG result. It thus remains a challenging task to understand accurately the localized-to-critical phase transition represented in Fig. 8(b).

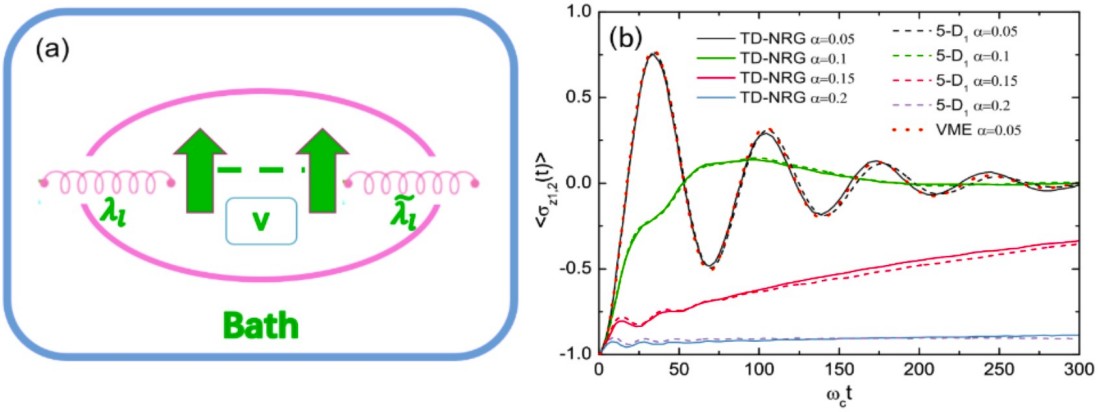

Figure 9: (a) Schematic of two spins coupled to a common boson bath in the two-spin SBM. (b) Time evolution of the population difference for $s = 1$ and various coupling constants α. Other parameters are $\Delta_1 = \Delta_2 = 0.1\omega_c$, $V = 0.05\omega_c$. The perturbative results are presented only for the moderately weak coupling strengths.

6.1.5 The two-spin spin-boson model

Using the multi-D_1 Ansatz, we study the two-spin SBM that is described by

$$\hat{H}_{\rm SBM}^{2-\rm spin} = -\sum_{i=1}^{2}\frac{\Delta_i}{2}\sigma_{xi} + V\sigma_{1z}\sigma_{2z} + \sum_l \omega_l b_l^\dagger b_l + \frac{\sigma_{z1}}{2}\sum_l \lambda_l(b_l + b_l^\dagger) + \frac{\sigma_{z2}}{2}\sum_l \tilde{\lambda}_l(b_l + b_l^\dagger), \tag{65}$$

where $\sigma_{\mu i}$ ($\mu = x, y, z$) is the μ-component Pauli matrix describing the ith spin, b_l ($b_l^\dagger$) is the annihilation (creation) operator of the lth bosonic mode of frequency ω_l, Δ_i is the tunneling amplitude of the ith spin. λ_l ($\tilde{\lambda}_l$) is the coupling constant between spin 1 (2) and the bath, as illustrated in Fig. 9(a). The dissipative effect of the bath is characterized by the spectral density $J(\omega)$ as follows:

$$J(\omega) = \sum_l \lambda_l^2 \delta(\omega - \omega_l) = 2\alpha\omega_c^{1-s}\omega^s\theta(\omega_c - \omega), \tag{66}$$

where α is the dimensionless coupling constant, ω_c is the cutoff frequency, $\theta(\omega)$ is the step function,and s is the spectral exponent.

In Fig. 9(b), the reduced dynamics of the spins in the Ohmic bath are obtained by the multi-D_1 Ansatz, the time-dependent numerical renormalization group (TD-NRG), and the variational master equation (VME) approach. From weak to strong coupling, the TD-NRG and the multi-D_1 results are in great agreement with each other. In addition, the perturbative VME approach is found to yield accurate results similar to those of the multi-D_1 approach and TD-NRG for weak coupling.

Interestingly, the multi-D_1 and TD-NRG results show that the spin becomes localized in the strong coupling regime.

6.2 The Landau-Zener transition

In Sec. 6.1.3, we studied the dynamics of a two-level system driven by a sinusoidally varying external field and its spectral manifestation. Here we turn our attention to the LZ transition that comes into play when the energy difference between two diabatic states is swept through an avoided level crossing. The total Hamiltonian of a linearly driven two-level system interacting with a bosonic bath is given by

$$\hat{H}_{\mathrm{LZM}} = \hat{H}_{\mathrm{LZ}} + \hat{H}_{\mathrm{B}} + \hat{H}_{\mathrm{SB},\theta} \tag{67}$$

where $\hat{H}_{\mathrm{LZ}}$ is the standard LZ Hamiltonian for an isolated two-level system,

$$\hat{H}_{\mathrm{LZ}} = \frac{vt}{2}\sigma_z + \frac{\Delta}{2}\sigma_x \tag{68}$$

The states, $|\uparrow\rangle$ and $|\downarrow\rangle$, are eigenstates of the qubit Hamiltonian $\frac{vt}{2}\sigma_z$ with an energy difference vt (with level-crossing speed $v > 0$). Transition-inducing tunneling strength Δ represents intrinsic coupling between the two diabatic states. To consider the LZ transition in an environment, we model a bosonic bath of N quantum harmonic oscillators as in Eq. (13), and the qubit-bath coupling by the Hamiltonian $\hat{H}_{\mathrm{SB},\theta}$ [158],

$$\hat{H}_{\mathrm{SB},\theta} = \sum_{q=1}^{N} \frac{\gamma_q}{2} \left(\cos\theta_q \sigma_z + \sin\theta_q \sigma_x\right) \left(\hat{b}_q^\dagger + \hat{b}_q\right) \tag{69}$$

where ω_q indicates the frequency of the q-th mode with creation (annihilation) operator $\hat{b}_q^\dagger(\hat{b}_q)$. γ_i and θ_i are the qubit-oscillator coupling and the interaction angle, respectively. The bath alters qubit energies via diagonal coupling (σ_z) and induces transitions between qubit levels via off-diagonal coupling (σ_x). The bath and its coupling to the system are characterized by a spectral density function, $J(\omega) = \sum_q \gamma_q^2 \delta(\omega - \omega_q) = 2\alpha\omega_c^{1-s}\omega^s e^{-\omega/\omega_c}$, where α and ω_c are defined as in Sec. 6.1.1. The Ohmic bath is specified by $s = 1$, and $s < 1 (> 1)$ denotes the sub-Ohmic (super-Ohmic) bath [159].

As shown in Figs. 10 (a)-(d), we compare the LZ dynamics of the sub-Ohmic, Ohmic and super-Ohmic bath with an identical coupling strength $\alpha = 0.002$. Figs. 10 (a) and (b) display LZ dynamics for the sub-Ohmic bath ($s = 0.5$) and the Ohmic bath ($s = 1$). Figs. 10(c) and (d) depict time evolution of the transition probability using the super-Ohmic bath with $s = 1.5$ and 2, respectively. For $\theta = 0$, there exists only one stage of the LZ transition near $t = 0$ for nonzero Δ. That is, in the

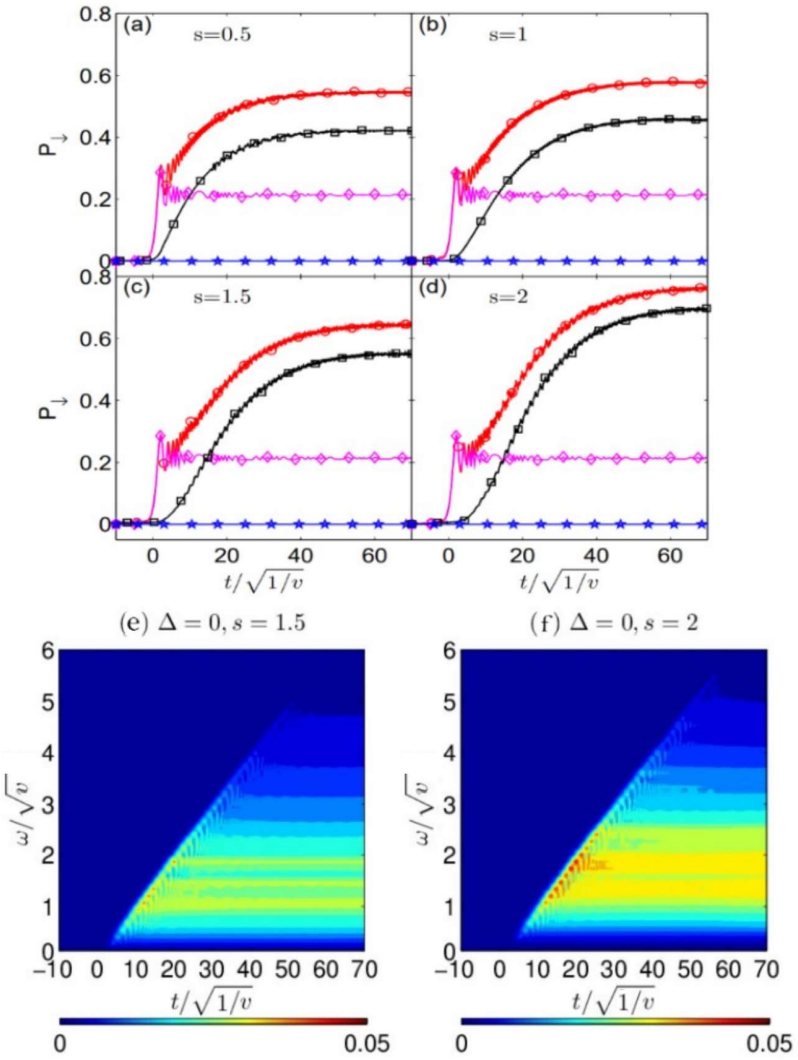

Figure 10: Time evolution of transition probability for (a) a sub-Ohmic bath of $s = 0.5$, (b) an Ohmic bath of $s = 1$, and (c) a super-Ohmic bath of $s = 1.5$ and (d) $s = 2$ is obtained from the $D_2^{M=3}$ Ansatz with an identical coupling strength $\alpha = 0.002$. $\omega_c = 10\sqrt{v}$. For each of the four values of s, four cases are shown: $\Delta = 0.4\sqrt{v}, \theta = \pi/2$ (red line, circles), $\Delta = 0.4\sqrt{v}, \theta = 0$ (magenta line, diamonds), $\Delta = 0, \theta = \pi/2$ (black line, squares), and $\Delta = 0, \theta = 0$ (blue line, pentagrams). Time evolution of the boson number using for a super-Ohmic bath of (e) $s = 1.5$ and (f) $s = 2$, in the presence of off-diagonal coupling only ($\theta = \pi/2$). Other parameters are $\alpha = 0.002$ and $\Delta = 0$.

presence of only diagonal coupling, LZ dynamics of $\Delta = 0.4\sqrt{v}$ (magenta lines, diamonds) is almost identical in the four panels. For $\theta = \pi/2$, time evolution of the transition probability for $\Delta = 0$ has a single stage of slow growth until it reaches its steady state, and converged probabilities and convergence times depend on the spectral densities. Figs. 10 (a)-(d) also reveal that the convergence time for large s is significantly longer than that for a small s, since spectral densities of large s involve prominent contribution from high-frequency modes. For $\Delta = 0.4\sqrt{v}$, there exist two-stage transitions in the presence of off-diagonal coupling. In the first stage, transition probability jumps up at $t = 0$. In the second stage, it gradually reaches the steady state with the same convergence time as that of $\Delta = 0$. Further calculations show that there exist two-stage transitions for all non-zero tunneling strengths in the presence of off-diagonal coupling. In addition, as expected, the converged transition probability obtained from multi-D_2 Ansatz agrees with the steady-state analytic expression by Hänggi and coworkers [160]:

$$P_{\uparrow\to\downarrow}(\infty) = 1 - \exp\left[\frac{-\pi\left(\left|\Delta - \frac{1}{2}E_0\sin(2\theta)\right|^2 + S\sin^2\theta\right)}{2v}\right]. \tag{70}$$

To investigate the role of bosons, the time-dependent boson number $\langle\hat{b}_q^\dagger\hat{b}_q\rangle$ is calculated with zero initial boson number, and shown in Figs. 10 (e) and (f). If the qubit is only off-diagonally coupled to a single harmonic oscillator, the LZ transition would be temporally shifted from $t = 0$ to $t = \omega/v$, independent of the coupling strength [161]. If qubit is off-diagonally coupled to multiple harmonic oscillators, the transition will then occur mainly after $t = 0$ as there is a temporal shift of each mode, as shown in Figs. 10 (e) and (f). Because the split between diabatic states varies linearly with time, the frequency of the bosons created via qubit-bath coupling also has the same time dependence, resulting in the upper edge of the triangle starting from $t = 0$ in the $\omega - t$ plots. It is found that very few bosons will be created for $t < 0$, regardless of s and α. For a larger s, more high-frequency bosons are created, resulting in a larger steady-state probability for identical α. The time taken to create high-frequency bosons also increases, which can be seen from comparing Fig. 10 (f) and Fig. 10 (e). This is expected from the convergence times taken to reach steady states in Figs. 10 (d) and (c).

Very recently, the multi-D_2 Ansatz has been utilized to explore photon-assisted dynamics of the Landau-Zener-Stückelberg-Majorana interferometry, driven by a sinusoidal external driving field, with the photon mode initialized with Schrödinger-cat states [162]. Transition pathways involving multiple energy levels are unveiled by analyzing the photon dynamics, offering insights into quantum state control and monitoring. Similar applications of the multi-D_2 Ansatz have been made to hybrid circuit quantum electrodynamics devices in a number of settings by Zheng *et al.* [163–165] In a Rabi-dimer system with the qubits coupled to a collection of micromechanical resonators, the composite

photon-qubit-phonon dynamics has been investigated using the multi-D_2 Ansatz. The photon states can be engineered not only by external driving fields, but also via manipulating the qubit states through tuning the qubit-phonon coupling. The schemes proposed in these studies for quantum state engineering and control would be beneficial to qubit and photon states engineering in quantum information devices and quantum computers.

6.3 The Holstein Hamiltonian

6.3.1 Diagonal exciton-phonon coupling

In Holstein's original treatment exciton-phonon coupling was limited to the site-diagonal form [166], and the Holstein Hamiltonian in the site-space representation reads

$$\begin{aligned} \hat{H}_{\rm Hol} &= \hat{H}_{\rm ex}^{\rm n.n.} + \hat{H}_{\rm ph}^{\rm Ein} + \hat{H}_{\rm ex-ph}^{\rm diag}, \\ \hat{H}_{\rm ex}^{\rm n.n.} &= -J\sum_n a_n^\dagger (a_{n+1} + a_{n-1}), \\ \hat{H}_{\rm ph}^{\rm Ein} &= \omega \sum_n b_n^\dagger b_n, \\ \hat{H}_{\rm ex-ph}^{\rm diag} &= g\omega \sum_n (b_n^\dagger \ + \ b_n) a_n^\dagger a_n, \end{aligned} \tag{71}$$

where $\hat{H}_{\rm ex}^{\rm n.n.}$ is the nearest-neighbor excitonic coupling Hamiltonian, J is the nearest-neighbor transfer integral, and $\hat{H}_{\rm ex-ph}^{\rm diag}$ is the diagonal exciton-phonon coupling Hamiltonian with coupling strength g. $\hat{H}_{\rm ph}^{\rm Ein}$ is the Hamiltonian for Einstein phonons with frequency ω.

Many methods that were used to study the Fröhlich Hamiltonian, Eq. (2), have been borrowed to treat the Holstein Hamiltonian. For example, the intermediate coupling theory of Lee, Low and Pines [167], formulated in 1953 for the Fröhlich Hamiltonian, was later used by Merrifield [76] in a variational treatment of Eq. (71). Instead of resorting to the Lee-Low-Pines transformation, which eliminates the exciton coordinate from the Holstein Hamiltonian, Toyozawa's Ansatz and the Global-Local Ansatz, being translationally invariant, are fully capable to treat the ground state properties of Eq. (71). Fig. 11 (a) displays the phase diagram of the zone-center self-trapping in the g-J plane given by the small polaron Ansatz of Eq. (3), Toyozawa's Ansatz of Eq. (7), and the Global-Local Ansatz of Eq. (11). The area of the wedge-shaped region is found to decrease with increasing sophistication of the variational trial state. Multiple solutions are obtained within the sizable, wedge-shaped discontinuity regions for the small polaron Ansatz. More sophiscated Ansätze significantly reduced the area of the discontinuity region: the outer thin tongue for Toyozawa's Ansatz and the inner thin tongue for the Global-Local Ansatz.

The simple coherent state in Eq. (5) has an inherent deficiency if the limit of weak coupling is

considered. Assuming a transfer integral J greater than $\omega/4$, the bare cosine exciton band intersects, at some finite crystal momentum K°, a horizontal line at ω above the bottom of the bare exciton band, which will be called the one-phonon line. For a non-interacting exciton-phonon system, there is a quasi-continuum of states above the one-phonon line [168–170], which can be readily explained by level-crossing arguments. This quasi-continuum turns into a true continuum as the volume goes infinite. Depending on whether the magnitude of crystal momentum K is greater or smaller than $|K^\circ|$, the ground state of the non-interacting system assumes different characteristics. For $K > K^\circ$, the ground state contains one phonon with momentum K and one exciton with zero momentum, while for $K < K^\circ$, the ground state contains only the phonon vacuum and the bare exciton with momentum K. In the interacting system, as the coupling strength goes to zero, the ground state is expected to be essentially phonon-free at low crystal momenta ($K < K^\circ$) and essentially one-phonon at high crystal momenta ($K > K^\circ$). Therefore, the small polaron Ansatz is rather inadequate in this limit as the single coherent state in Eq. (5) fails to properly describe the one-phonon number state. In contrast, a ground-state phase diagram given by Toyozawa's Ansatz shows significant improvements over Eq. (3), especially in the weak coupling limit, as shown in Fig. 11 (a). By employing an additional set of variational parameters that provide explicit exciton-phonon correlations, the Global-Local Ansatz improves upon Toyozawa's Ansatz and reduces considerably the discontinuity region in the g-J phase diagram of Fig. 11 (a).

Projecting the Davydov D_1 Ansatz onto the crystal-momentum space leads to the delocalized D_1 Ansatz, $|\Psi^K_{\mathrm{dD}_1}\rangle$ of Eq. (12), with substantially higher accuracy than Toyozawa's Ansatz and the Global-Local Ansatz, and ground state energies of Eq. (71) have been obtained with a precision matching that of the computationally much more demanding DMRG method (cf. Table I of Ref. [84]). The delocalized D_1 Ansatz lowers the ground-state energies at the Brillouin zone boundary significantly compared with Toyozawa's Ansatz and the Global-Local Ansatz in the weak coupling regime, while considerable improvement is demonstrated to have been achieved over the entire Brillouin zone in the strong coupling regime. Unique solutions are obtained with the delocalized D_1 Ansatz for various initial conditions of an iterative relaxation procedure in variational energy optimization when the transfer integral J is 20 times the phonon frequency at the zone center, implying the absence of any self-trapping discontinuity in the g-J phase diagram of Fig. 11 (a).

It can be shown that while the transfer integral J may alter the spatial distribution of the phonon displacements, the total deformation of the lattice is conserved: $\sum_n \lambda^K_n = g$ for Toyozawa's Ansatz, for example [82]. It can also be shown that the sum-rule for phonon displacements in the Davydov $\tilde{\mathrm{D}}$ Ansatz is satisfied by $\sum_n \alpha_n + \beta_n = g$ [83]. These reults are consistent with those of Lee-Low-

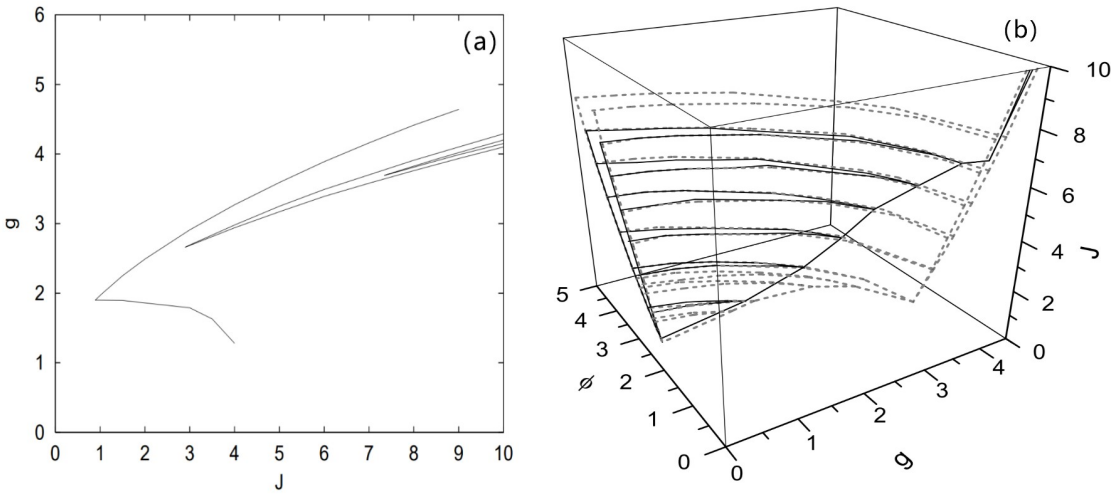

Figure 11: (a) Phase diagram of the zone-center self-trapping in the g-J plane for the small polaron Ansatz of Eq. (3), Toyozawa's Ansatz of Eq. (7), and the Global-Local Ansatz of Eq. (11) (in the order of decreasing width of the wedge-shaped religion). Multiple solutions are obtained within the wedge-shaped discontinuity regions for the small polaron Ansatz. More sophiscated Ansätze significantly reduced the area of the discontinuity region: the outer thin tongue for Toyozawa's Ansatz and the inner thin tongue for the Global-Local Ansatz. (b) Phase diagram of the near zone-center self-trapping in g-ϕ-J space for the Global-Local Ansatz (solid) and Toyozawa's Ansatz (dashed). Under the solid-line ax-shaped region (small J), there is a unique solution to the set of self-consistency equations derived from the Global-Local Ansatz, and the crossover from small-polaron correlations to large-polaron ones is smooth. Within the ax-shaped region, two convergent solutions are found to coexist for the the Global-Local Ansatz. The 2D phase diagram of (a) is partially reproduced here on the J-g subspace.

Pines transformation which yields an effective phonon Hamiltonian for each crystal momentum by eliminating the electronic degree of freedom:

$$\hat{H}_{\rm trans} = \sum_K \hat{H}^K a_K^\dagger a_K, \tag{72}$$

$$\hat{H}^K = \sum_q [b_q^\dagger b_q + gN^{-1/2}(b_q + b_{-q}^\dagger)] - 2J\cos(K - \sum_q q b_q^\dagger b_q). \tag{73}$$

Here $\hat{H}_{\rm trans}$ stands for the transformed Hamiltonian, and $\hat{H}^K$ is the effective phonon Hamiltonian. The last term of the effective Hamiltonian $\hat{H}^K$ couples all $q \neq 0$ phonon modes. The $q = 0$ mode, however, is left alone, forming a simple displaced oscillator with phonon displacement g. In the site-space, this leads to the "sum-rule": the sum of phonon displacements over all sites equals g.

In the strong coupling regime, the polaron is called "small" in the sense that the phonon component of the polaron wave function is mostly localized on the site where the electronic excitation is generated. The lattice distortion surrounding the excitation (or electron) creates a potential well sufficiently deep so that the excitation (or electron) is "self-trapped" by the phonon cloud it itself generates. In the weak coupling regime, on the other hand, the spatial extension of the lattice distortion accompanying the excitation (or electron) is significantly increased as compared to the small polaron. Consequently, the excitation (or electron) together with the phonon cloud of large spatial dimension is called a "large" polaron. A large polaron has an effective mass comparable to that of a bare exciton (or electron), while a small polaron may acquire an effective mass several orders of magnitude larger. The cross-over between the two is found to exhibit "quasi-phase-transition" behavior, which has long been a matter of contention and interest for both the Fröhlich Hamiltonian [171–176] and the Holstein Hamiltonian [75–78, 177–183]. Recent path-integral formulations by Gerlach and Löwen (1987) [184], and Löwen (1988) [185], claim the nonexistence of a formal phase transition in Fröhlich systems (at finite temperatures for optical phonons), and in Holstein systems (at all temperatures for optical phonons, and at nonzero temperatures for arbitrary dispersion). Calculations based on Davydov's Ansätze provide useful insights into how the apparent discontinuity, marking the transition between large and small polaron, is introduced due to insufficiencies in the variational Ansätze. With the small polaron Ansatz, a large wedge-shaped discontinuity regime is found in the phase diagram spanned by the transfer integral J and exciton-phonon couling constant g, while Toyozawa's Ansatz reduces that discontinuity regime to merely a thin tongue, and the more sophisticated Global-Local Ansatz of Eq. (11) pushes the tip of the tongue to much greater J, as shown in Fig. 11 (a). For large transfer integral J, the discontinuity tongue roughly follows $g^2 = J$, as suggested by adiabatic polaron theories.

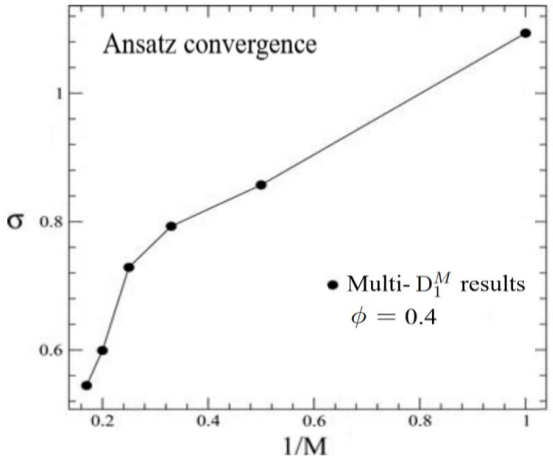

Figure 12: Relative deviation σ of the multi-D_1 Ansatz, defined in Eq. (27), is displayed as a function of $1/M$ for the off-diagonal coupling only case with the coupling strength $\phi = 0.4$. Other parameters $J = W = g = 0$ are set. In the limit of $M \to \infty$, the multi-D_1 Ansatz is numerically exact.

6.3.2 Off-diagonal exciton-phonon coupling

Off-diagonal coupling, also known as the "nonlocal coupling," is defined as the dependence of the electronic excitation transfer integral on phonon coordinates. Properties of some molecular crystals are significantly affected by off-diagonal coupling; in particular, nonlocal coupling is believed to play an important role in the scattering of transport species in aromatic hydrocarbon crystals [186–193], in the V_k center in alkali halides [194–196], in self-trapping of magnetic polarons in antiferromagnetic semiconductors [197], and in excimer spectra [198]. However, due to difficulties in achieving a reliable treatment, off-diagonal coupling is customarily omitted [199]. It has been demonstrated that the method of HDA is fully capable to treat off-diagonal coupling to desired precision by increasing the sophistication in the Davydov trial state [26, 27, 123, 200]. In Fig. 12, relative deviation σ of the multi-D_1 Ansatz, as defined in Eq. (27), is plotted as a function of $1/M$ for the off-diagonal coupling only case ($\phi = 0.4$, and $J = W = g = 0$). With the increase of the Ansatz multiplicity, σ gradually vanishes, and the multi-D_1 Ansatz becomes numerically exactly for sufficiently large M.

Fig. 11 (b) displays the phase diagram of the near zone-center self-trapping in g-ϕ-J space for the Global-Local Ansatz (solid) and Toyozawa's Ansatz (dashed). Under the solid-line ax-shaped region (small J), there is a unique solution to the set of self-consistency equations derived from the Global-Local Ansatz, and the crossover from small-polaron correlations to large-polaron ones is smooth. Within the ax-shaped region, two convergent solutions are found to coexist for the the

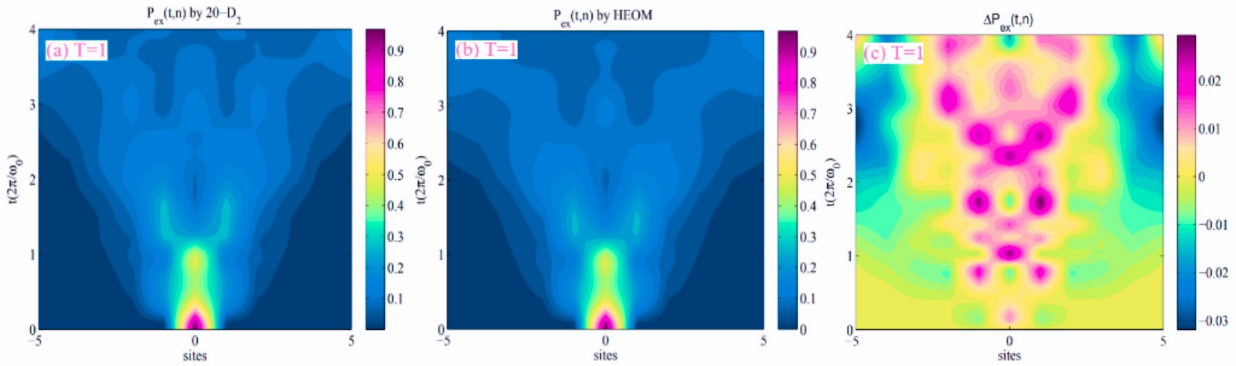

Figure 13: Time evolution of the exciton probability $P_{ex}(t,n)$ at $T=1$ for the case of $J=0.1, W=0, g=0, \phi=0.3$ are displayed in panels (a) and (b) for a lattice of 10 sites, corresponding to the results obtained with the $\mathrm{D}_2^{M=20}$ Ansatz and the HEOM method, respectively. The differences $\Delta P_{ex}(t,n)$ between the HEOM method and the $\mathrm{D}_2^{M=20}$ Ansatz are also displayed in panel (c).

Global-Local Ansatz. The 2D phase diagram of Fig. 11 (a) is partially reproduced in Fig. 11 (b) on the J-g subspace.

Toyozawa's Ansatz has been utilized to compute various types of entanglement in the Holstein system of Eq. (71) [201, 202]. For exmaple, it has been demonstrated that a simple analysis of quantum entanglement between excitonic and phononic degrees of freedom allows one to effectively characterize both the small and the large polaron regime as well as the crossover in between [202]. The small (large) polaron regime corresponds to a high (low) degree of bipartite quantum entanglement between the exciton and the phonon cloud that clothes the exciton. Moreover, decreasing the exciton-phonon coupling strength through the self-trapping line is clearly accompanied by a sharp drop of exciton-phonon entanglement. With off-diagonal coupling, self-trapping takes place with dramatic changes in entanglement occurring at both vicinities near the Brillouin-zone center and edge [201].

Combining the multi-D_2 Ansatz with the TFD method, finite temperature dynamics of a Holstein polaron has been worked out to great precision [45]. Using the hierarchy equations of motion method as a benchmark [203], it has been demonstrated that the finite-temperature variational approach based on the multi-D_2 Ansatz provides an efficient, robust description of dynamics of the Holstein polaron in the presence of off-diagonal coupling at various temperatures, as shown in Fig. 13 for a lattice of 10 sites. The TFD method handles temperature effects with key numerical advantages over other treatments of finite-temperature dynamics based on quantum master equations in the Liouville space or wave function propagation with Monte Carlo importance sampling. While for weak to moderate diagonal coupling an increase in temperature inhibits polaron mobility, it is found that off-diagonal coupling induces phonon-assisted transport which dominates at high temperatures. As

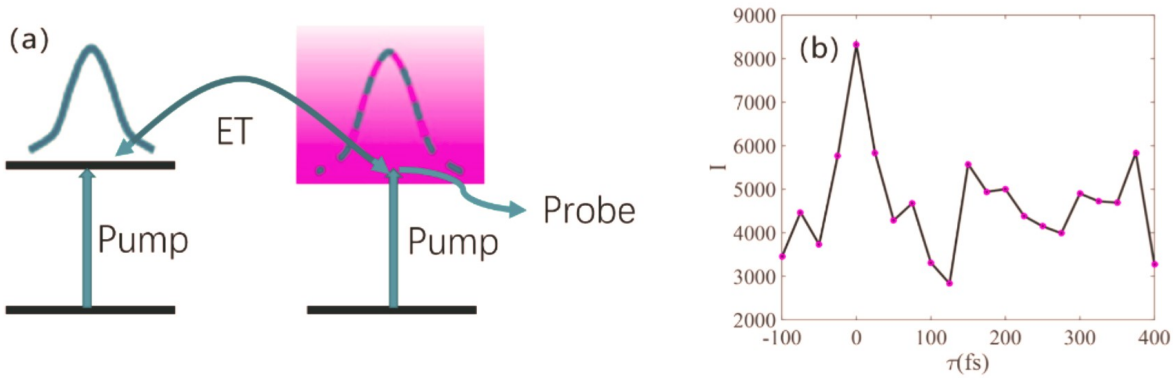

Figure 14: (a) Sketch of ultrafast phase coherent excitation of individual LH2 complexes. The first pulse on the left creates an excitation in the B800 band, and the second pulse on the right, resonant with the B850 band, modulates the population transfer to the B850 excited states after energy transfer to the B850 band. (b) Single-molecule signals $I(\tau)$ simulated for excitonic energy modulation amplitudes $\delta_{B800} = 60$ cm^{-1} and $\delta_{B850} = 130$ cm^{-1}. The discretization step Δ_τ is 5 fs and 25 fs (lower panels) and $\tau_1 = \tau_2 = 15$ fs.

a proof of concept, marrying the multi-D_2 Ansatz to the TFD method provides a unified treatment of coherent and incoherent transport in molecular crystals and is applicable to any temperature.

6.4 Excitation energy transfer in light-harvesting antenna complexes

6.4.1 Simulation of femtosecond single-molecule signals of individual light-harvesting complexes

Recent phase-locked femtosecond double-pump experiments on individual LH2 complexes revealed undamped oscillatory responses on a time scale of at least 400 fs [204]. A sketch of the experimental detection scheme is shown in Fig. 14(a), in which a single LH2 complex is excited by a two-color pulse pair with the delay time Δt and the relative carrier envelope phase $\Delta\phi$ generated by applying the spectral phase function. The first pulse on the left of Fig. 14(a) creates an excitation in the B800 band. After energy transfer to the B850 band, the second time-delayed pulse on the right of Fig. 14(a), resonant with the B850 band, modulates the population transfer to the B850 excited states by quantum interference and thus changes the probe signal, the spontaneous emission from a single complex. Inspired by these experiments, a first principles theoretical description has been developed for the simulation of femtosecond double-pump single-molecule signals of molecular aggregates using the method of Davydov's Ansätze [205, 206]. All singly excited electronic states and vibrational modes with significant exciton-phonon coupling were incorporated into a system Hamilto-

nian and were treated with the Davydov D_1 Ansatz [205]. The remaining intra- and inter-molecular vibrational modes were handled as a heat bath and their effect was accounted for through line shape functions. The theory is then applied to simulate single-molecule signals of the individual light harvesting complexes LHCII [205] and LH2 [206]. All excitonic and exciton-phonon couplings were treated numerically accurately, in a nonperturbative manner. Calculated signals exhibit pronounced oscillations of mixed electron-vibrational (vibronic) origin with periods decreasing with decreasing exciton-phonon coupling. Heterogeneity of the local environment results in the (Gaussian) modulation of the electronic energies of the light-harvesting complexes, which is manifested as noise in the single-molecule signals (see Fig. 14(b)). These simulations provide novel insights into the origin of coherent dynamics and oscillatory responses in individual molecular aggregates and uncover microscopic origins of the formation of femtosecond single-molecule signals.

6.4.2 Exciton diffusion in light-harvesting complexes

An accurate description of energy transfer in light harvesting systems has to go beyond perturbative theory and Markovian approximations that are often employed in dynamics descriptions of energy transfer in natural and artificial photosynthesis. Inter-LH2 energy transfer takes place between neighboring B850 rings that are densely packed, and strong inter-pigment coupling gives rise to delocalized exciton over several chromophores. Excitation energy migration in B850 nanoarrays is modeled with an extended Holstein Hamiltonian [177–183]:

$$\hat{H}_{\mathrm{B850}} = \sum_{r_1 r_2} \sum_{mn} J_{mn}^{r_1 r_2} \hat{a}_m^{r_1 \dagger} \hat{a}_n^{r_2} + \hat{H}_{\mathrm{bath}} + \hat{H}_{\mathrm{ex-bath}}. \tag{74}$$

Here the first term on the right hand side of Eq. (74) is the Frenkel-exciton Hamiltonian, and $\hat{a}_n^{r\dagger}$ ($\hat{a}_n^r$) is the exciton creation (annihilation) operator on the n^{th} site (with a total number of $N_{\mathrm{s}} = 16$ sites in one B850 ring) of the r^{th} ring (with a total number of N_{r} B850 rings). $J_{mn}^{r_1 r_2}$ is the excitonic coupling between pigment m on the r_1^{th} B850 ring and pigment n on the r_2^{th} B850 ring, and diagonal elements are site energies of the B850 pigments with computational details given in Ref. [207]. The exciton dynamics in B850 complexes is affected by environmental effects, such as conformational changes in pigments and surrounding proteins, which are modeled as a set of harmonic oscillators, $\hat{H}_{\mathrm{bath}} = \sum_r \sum_q \omega_q^r \hat{b}_q^{r\dagger} \hat{b}_q^r$. Here $\hat{b}_q^{r\dagger}$ ($\hat{b}_q^r$) is the phonon creation (annihilation) operator with momentum $q = 2\pi n_q / N_{\mathrm{s}}$ ($n_q = -7, -6, \cdots, 7, 8$) and frequency ω_q^r in the r^{th} ring. The exciton is coupled to the phonon bath via the coupling Hamiltonian

$$\hat{H}_{\mathrm{ex-bath}} = -\frac{1}{\sqrt{N_{\mathrm{s}}}} \sum_r \sum_n \sum_q g_q^r \omega_q^r \hat{a}_n^{r\dagger} \hat{a}_n^r (e^{iqn} \hat{b}_q^r + e^{-iqn} \hat{b}_q^{r\dagger}). \tag{75}$$

Here g_q^r is the exciton-phonon coupling strength. For simplicity, a linear phonon dispersion $\omega_q^r = \omega_0[1 + W(2|q|/\pi - 1)]$ with a width of $W = 0.1$ is adopted. The exciton-phonon coupling strength is parameterized from the Huang-Rhys factor S with the relation $\sum_q (g_q^r)^2 \omega_q^r / N_\mathrm{s} = S\omega_0$ where $\omega_0 = 1670$ cm^{-1} is the characteristic phonon frequency and a fixed Huang-Rhys factor $S = 0.5$ is used.

To study the effects of coherence on exciton diffusion in B850 nanoarrays, the coherence size L_ρ based on the Davydov D_1 Ansatz is defined as [208, 209]

$$L_\rho(t) = \left(\sum_{r_1 r_2} \sum_{mn} |\rho_{mn}^{r_1 r_2}(t)| \right)^2 \left[N \sum_{r_1 r_2} \sum_{mn} |\rho_{mn}^{r_1 r_2}(t)|^2 \right]^{-1} \tag{76}$$

with

$$\rho_{mn}^{r_1 r_2}(t) = \mathrm{Tr}_\mathrm{b}\Big[|\Psi_{\mathrm{D}_1}(t)\rangle\langle\Psi_{\mathrm{D}_1}(t)| \hat{a}_m^{r_1 \dagger} \hat{a}_n^{r_2} \Big] = \alpha_m^{r_1 *}(t) \alpha_n^{r_2}(t) S_{mn}^{r_1 r_2}(t), \tag{77}$$

where the Debye-Waller factor $S_{mn}^{r_1 r_2}(t)$ is

$$S_{mn}^{r_1 r_2}(t) \;=\; \exp\Big\{ \sum_q \big[\lambda_{mq}^{r_1 *}(t) \lambda_{nq}^{r_2}(t) \delta_{r_1 r_2} - \frac{1}{2} |\lambda_{mq}^{r_1}(t)|^2 - \frac{1}{2} |\lambda_{nq}^{r_2}(t)|^2 \big] \Big\}. \tag{78}$$

Here $N = N_\mathrm{s} \times N_\mathrm{r}$ is the total number of pigments in the system. The coherence size L_ρ has been used as the exciton delocalization length in various photosynthetic systems, such as the LH2 [207, 208] and the chlorosome [210]. L_ρ quantifies the length scale over which $\rho_{mn}^{r_1 r_2}$ decays along the anti-diagonal direction [207, 208]. This quantity is related to the superradiance enhancement factor L_s which is the ratio of radiative decay rate of a molecular aggregate to that of a monomer of the same type. In a doorway-window representation, L_s can be written as [207, 208]

$$L_s(t) = \sum_{r_1 r_2} \sum_{mn} M_{mn}^{r_1 r_2} \rho_{mn}^{r_1 r_2}(t) \tag{79}$$

where $M_{mn}^{r_1 r_2} = \mathbf{d}_m^{r_1} \cdot \mathbf{d}_n^{r_2}$ contains all the relevant geometric information on the system with $\mathbf{d}_m^{r_1}$ being the unit vector of the transition dipole moment of pigment m on the r_1^{th} B850 ring. Exciton dynamics is first simulated in a three-ring B850 chain with the excitation initiated on the central B850. Three forms of excitation initiation are employed. In Cases I and II, the lowest and second lowest exciton state of the central ring are populated initially, respectively. In Case III, only one pigment on the central B850 is excited. For the third case, 16 trajectories are simulated and each trajectory is started from an individual pigment on the central complex. Results for 3 cases are shown in Fig. 15. For Case III, results averaged over 16 trajectories are depicted with those from a single trajectory.

The superradiance enhancement factor L_s and the coherence size L_ρ are recorded in simulation to characterize exciton delocalization in B850 nanoarrays. As can be seen from Eq. (79), L_s is

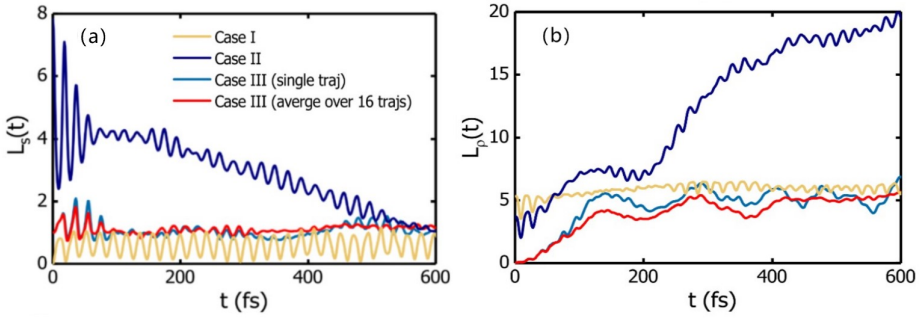

Figure 15: The superradiance enhancement factor (a), and the coherence size (b) for exciton diffusion in a chain of three B850 complexes. Three initial excitation conditions are used, i.e., the lowest (Case I) and the second lowest (Case II) exciton states, and an individual pigment (Case III) of the central complex. For comparison, results from a single trajectory (blue curves) of Case III are shown with the averaged results over 16 trajectories (red curves).

dependent on the state and the transition dipole configuration [207–209]. In contrast, L_ρ contains only information of the reduced density matrix. As illustrated in Fig. 15 (a), L_s in Case II has an initial value of 8, thanks to being initialized in the second lowest exciton state of B850 which is one of the superradiant states [207, 208]. For Case III where the exciton is initialized from one pigment, a superradiance enhancement factor oscillates around 1.0.

Compared to L_s, L_ρ presents a different picture as shown in Fig. 15 (b). At $t = 0$ fs, Case I has the largest L_ρ because of nearly uniform excitation for the pigments in the central ring. With temporal evolution, L_ρ oscillates around the value of 5 for Case I. Cases II and III exhibit larger coherence sizes covering more than 10 pigments. Special attention should be paid to the out-of-phase oscillations in L_s and L_ρ for Case II. The total transition dipole moment of the B850 complex is very small due cancellation of transition dipole moments of adjacent pigments. It follows that the emission is induced by the loss of coherence, and L_s increases with the decrease of L_ρ [207, 208].

6.5 Singlet fission

A process of exciton multiplication allowing an excited singlet state to be converted into two triplet excitations, SF has attracted great attention as it can potentially enable photovoltaic devices to bypass the Shockley-Queisser limit in conversion efficiency in monomers as well as in the crystalline phase of organic molecular aggregates [211]. A variety of factors are known to affect SF dynamics. For instance, molecular modes coupled to electronic excitations have been found recently to take a central role in the SF process according to theoretical calculations [212, 213] and ultrafast spectroscopic measurements [214–216]. It was also shown that efficient fission in pentacene derivatives [217–219]

and crystalline tetracene [220, 221] has been facilitated by high-frequency phonon modes owing to vibronic resonances. Especially, in diphenyl-dicyano-oligoene ($DPDC_n$) solid films, both diagonal and off-diagonal exciton phonon coupling can aid efficient SF if excitonic coupling is weak, and fission is only facilitated by diagonal coupling if excitonic coupling is strong. In the presence of off-diagonal coupling, it is found that high frequency modes create additional channels for rapid intramolecular SF [222]. In addition, little attention has been paid to accurate simulation of temperature effects on the conical intersections (CIs) mediated SF dynamics in organic molecular aggregates and its spectroscopic manifestations. Our current understanding of electron-vibration interactions including thermally assisted SF mechanisms is inadequate, hindering the design of versatile SF materials. To yield useful dynamic information on population transfer and spectral relaxation, a more realistic model system, e.g., an *ab initio* exciton model, needs to be considered, such as those presented by Zeng *et al.* [223], Petelenz *et al.* [224, 225] and Zirzlmeier *et al.* [226], allowing for simulation for diabatic population dynamics and time evolution of nonlinear spectroscopic signals, Time-dependent Davydov Ansätz and their multiple extensions have been shown to represent an accurate, efficient description for the electron-vibrational dynamics with many degrees of freedom [51, 222, 227]. Among its myriad applications, the method is also found to perform excellently for both the diabatic and adiabatic wave-packet dynamics at multimode conical intersections. As demonstrated previously [51, 126, 222, 227], the method of Davydov's Ansätze can be conveniently utilized to simulate third-order response functions and various spectroscopic signals.

6.5.1 Temperature-dependent fission dynamics via conical intersections

We consider, as an example, the two-electronic-states (S_1 and TT) and two/three-vibrational-modes models of SF in rubrene crystal. Here S_1 is the (optically bright) singlet state and TT is the (optically dark) correlated triplet pair state. For simplicity, the higher-lying singlet states and triplet states are not included explicitly. The linear-vibronic-coupling (LVC) Hamiltonian of the CI model can be recast in the operator form [31, 51, 227]

$$\begin{aligned}\hat{H}_{\rm LVC} = &\sum_{k=S_1,TT} \epsilon_k |k\rangle\langle k| + \sum_{\alpha=t,c} w_\alpha \hat{b}_\alpha^\dagger \hat{b}_\alpha \\ &+ \frac{\lambda}{\sqrt{2}}(|S_1\rangle\langle TT| + |TT\rangle\langle S_1|)(\hat{b}_c^\dagger + \hat{b}_c) + \frac{1}{\sqrt{2}} \sum_{\alpha=t} \sum_{k=S_1,TT} \kappa_\alpha^k |k\rangle\langle k|(\hat{b}_\alpha^\dagger + \hat{b}_\alpha),\end{aligned}$$

where $\hat{b}_\alpha^\dagger(\hat{b}_\alpha)$ is the electronic creation (annihilation) operator of the α-th mode. ε_{S_1} and ε_{TT} are the vertical excitation energies of the states $|S_1\rangle$ and $|TT\rangle$, respectively, and λ is the interstate coupling constant responsible for the CI of $|S_1\rangle$ and $|TT\rangle$. κ_α^k are the linear intrastate electron-vibrational couplings. We employ two models to simulate SF dynamics. The first one, the two-mode

model, is essentially the model suggested in Ref. [228] and further exploited in Ref. [227], which includes a low-frequency coupling mode Q_c and a single high-frequency tuning mode Q_{t1}. The second model, the three-mode model, adds an extra low-frequency tuning mode Q_{t2}. The motivation behind the consideration of the three-mode model is twofold. First, there are indications that extra low-frequency tuning modes may be necessary for a detailed modeling of the SF process in rubrene. Second, an additional low-frequency tuning mode increases sensitivity of the model to temperature effects. Numerical values of the model parameters are collected in Table I.

Table I. Numerical values of the model parameters (in units of eV).

Energy	mode	ω_l	$\kappa_l^{(1)}$	$\kappa_l^{(2)}$	λ_l
$\epsilon_{S_1} = 2.23$	Ω_c	0.0154	0	0	0.0745
$\epsilon_{TT} = 2.28$	Ω_{t1}	0.1860	0.3720	-0.3720	0
	Ω_{t2}	0.0260	0.0745	-0.0745	0

We set $N = 14$ ($N = 10$) for the two-mode (three-mode) CI model to simulate finite-temperature population dynamics $P(t)$ of the S_1 state in the SF process (cf. Fig. 2). For both models, a multiplicity of $M = 108$ is used for the multi-D_2 Ansatz in simulation. The population dynamics $P(t)$ in the two models is presented in Figs. 16 and 17 for the temperature range from 0 to 300 K. Fig. 16 displays an accuracy comparison of $P(t)$ for the two-mode model between the Multi-D_2 Ansatz and TFD-MCTDH. There is great agreement between the two over a broad temperature range. Using the displaced number states, the Multi-D_2 Ansatz method has demonstrated its simplicity, accuracy and efficiency, an excellent apparatus for the study of dynamics CI system.

The population decay (hence the SF efficiency) increases with temperature in both models, which can be understood by the following considerations. Using the explicit form of H_S, it is straightforward to show that the initial depopulation dynamics is Gaussian, $\langle P(t)\rangle = \exp\{-\nu^2 t^2\} + O(t^3)$, where ν^{-1} is the so-called Zeno time which can be evaluated according to Refs. [51, 229]. Explicitly,

$$\nu^2 = \lambda^2 \langle Q_c^2 \rangle = \lambda^2 \left(\frac{1}{2} + \frac{1}{\exp\{\omega_c/(k_B T)\} - 1} \right). \tag{80}$$

Hence the population decay rate ν is minimal at $T = 0$ ($\nu = \lambda/\sqrt{2}$) and increases $\sim \sqrt{T}$ in the classical limit of $k_B T \gg \omega_c$, yielding $\nu = \lambda\sqrt{k_B T/\omega_c}$. Independent of the tuning modes, the initial decay of $P(t)$ is thus determined solely by temperature T and the coupling mode frequency ω_c, in agreement with the temperature dependency of initial population dynamics in Figs. 16 and 17. At $t > \nu^{-1}$, the $P(t)$ evolution becomes much more complex and depends strongly on the tuning modes. In particular, the depopulation in the 3-mode model is faster than that in the 2-model model. This indicates that thermally-activated modes accelerate the SF process. For $t < 75$ fs (Fig. 16) and

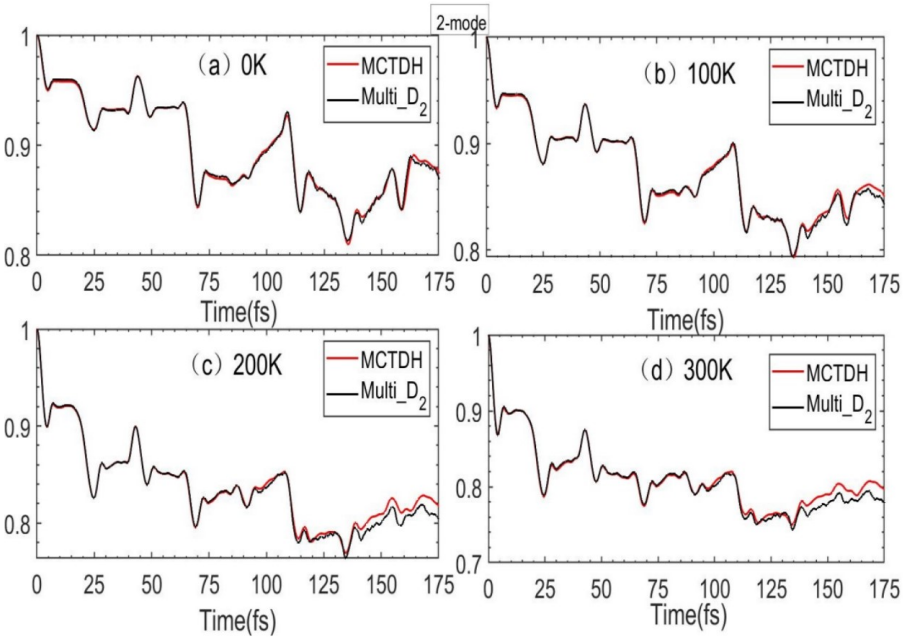

Figure 16: Accuracy comparisons of diabatic population dynamics of the singlet S_1 state between Multi-D_2 and TFD-MCTDH for the two-mode model for T $= 0, 100, 200, 300$ K.

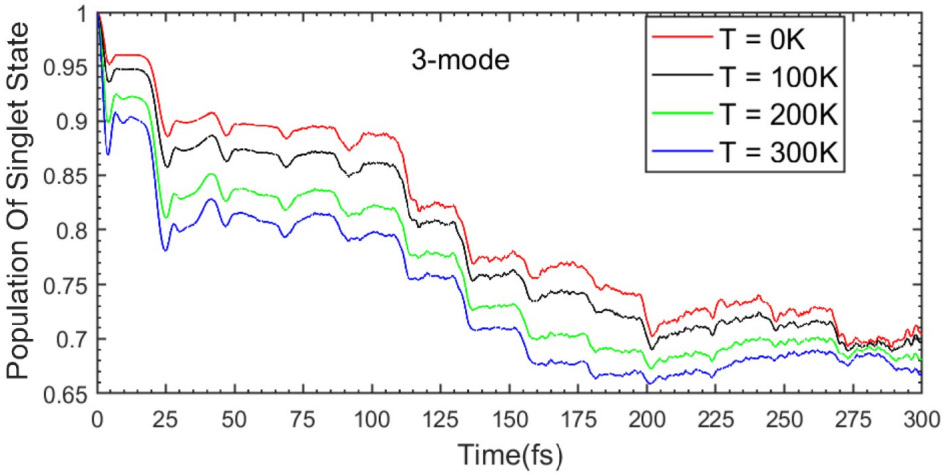

Figure 17: Diabatic population dynamics of the singlet S_1 state for the three-mode model for T $= 0, 100, 200, 300$ K.

$t < 150$ fs (Fig. 17), $P(t)$ exhibits a characteristic step-like structure which is characterized by the period of $2\pi/\omega_{t1} = 22$ fs, revealing the high-frequency tuning mode. This structure is indicative of the stepwise, CI-driven $|\mathrm{S}_1\rangle \rightarrow |\mathrm{TT}\rangle$ population transfer, generic for nonadiabatic vibronic systems (see Ref. [230] and discussion therein). On a longer timescale, $P(t)$ of Fig. 16 exhibits quite erratic behavior, which is typical for two-mode CIs [231]. The dynamics of $P(t)$ in Fig. 17 is smoother, faster, and more irreversible, since more modes are involved in the CI-driven population transfer.

6.5.2 Spectral simulation of crystalline rubrene

The more realistic model system of Ref. [51] is considered in this section so as to better understand the experimental results of Ref. [228]. The CI model, which contains all primary vibrational modes strongly affecting the SF process, is coupled to a harmonic phonon bath described by the Hamiltonian H_{B}, which mimics the impact of the remaining inter- and intramolecular modes on the SF dynamics. Thus, the total Hamiltonian is given by $H_{\mathrm{tot}} = H_{\mathrm{LVC}} + H_{\mathrm{B}} + H_{\mathrm{SB}}^{\mathrm{SF}}$, where the system-bath coupling Hamiltonian is assumed to be diagonal in the electronic space,

$$H_{\mathrm{SB}}^{\mathrm{SF}} = \sum_q \sum_{k=\mathrm{S}_1,\mathrm{TT}} |k\rangle\langle k|\kappa_q^k(\hat{B}_q^\dagger + \hat{B}_q). \tag{81}$$

and κ_q^k are the coupling constants. The phonon reservoir has two effects. Firstly, it is the source of optical dephasing between $|g\rangle$ and the vibronic states in the electronically excited manifold of $|\mathrm{S}_1\rangle - |\mathrm{TT}\rangle$, giving rise to the interesting spectral characteristics. Secondly, it also generates intra-manifold dephasing of $|\mathrm{S}_1\rangle - |\mathrm{TT}\rangle$, which dampens phonon wave packets, leading to population relocation. For simplicity, identical coupling coefficients are assumed for electronic states ($\kappa_q^{S_1} = -\kappa_q^{\mathrm{TT}}$), and an Ohmic spectral density $J(\omega) = \eta\omega\exp(-\omega/\omega_{\mathrm{cut}})$ is chosen to characterize bath-induced dephasing and relaxation, where η and ω_{cut} are the system-bath coupling strength and the cutoff frequency, respectively. It should be noted that coupling constants κ_q^k for bath modes in Eq. (81) can be obtained by discretizing the spectral density, the details of which can be found in Ref. [227]. In applying the Multi-D_2 Ansatz to spectral simulation of rubrene crystal, zero temperature is assumed.

By fitting the absorption spectra with the experimental data, the relevant parameters, such as the energies of diabatic states $\epsilon_{\mathrm{S}_1} = 2.50$ eV and $\epsilon_{\mathrm{TT}} = 2.58$ eV, the inter-state coupling $\lambda = 0.05$ eV, the optimal system-bath coupling strength $\eta = 0.2$, the cutoff frequency $\omega_{\mathrm{cut}} = 1000$ cm^{-1}, the primary phonon frequencies $\omega_{t1} = 1400$ cm^{-1}, $\omega_{t2} = 210$ cm^{-1}, and the corresponding dimensionless Huang-Rhys factors $S_1 = 0.805$ and $S_2 = 4.1$, are obtained. Furthermore, an antisymmetric intermolecular coupling mode with $\omega_c = 124$ cm^{-1} has been introduced in the CI model. The transition dipole moments are chosen as $\mu_{\mathrm{gS}_1} = 1$ and $\mu_{\mathrm{gTT}} = 0$ since the TT state is optically dark.

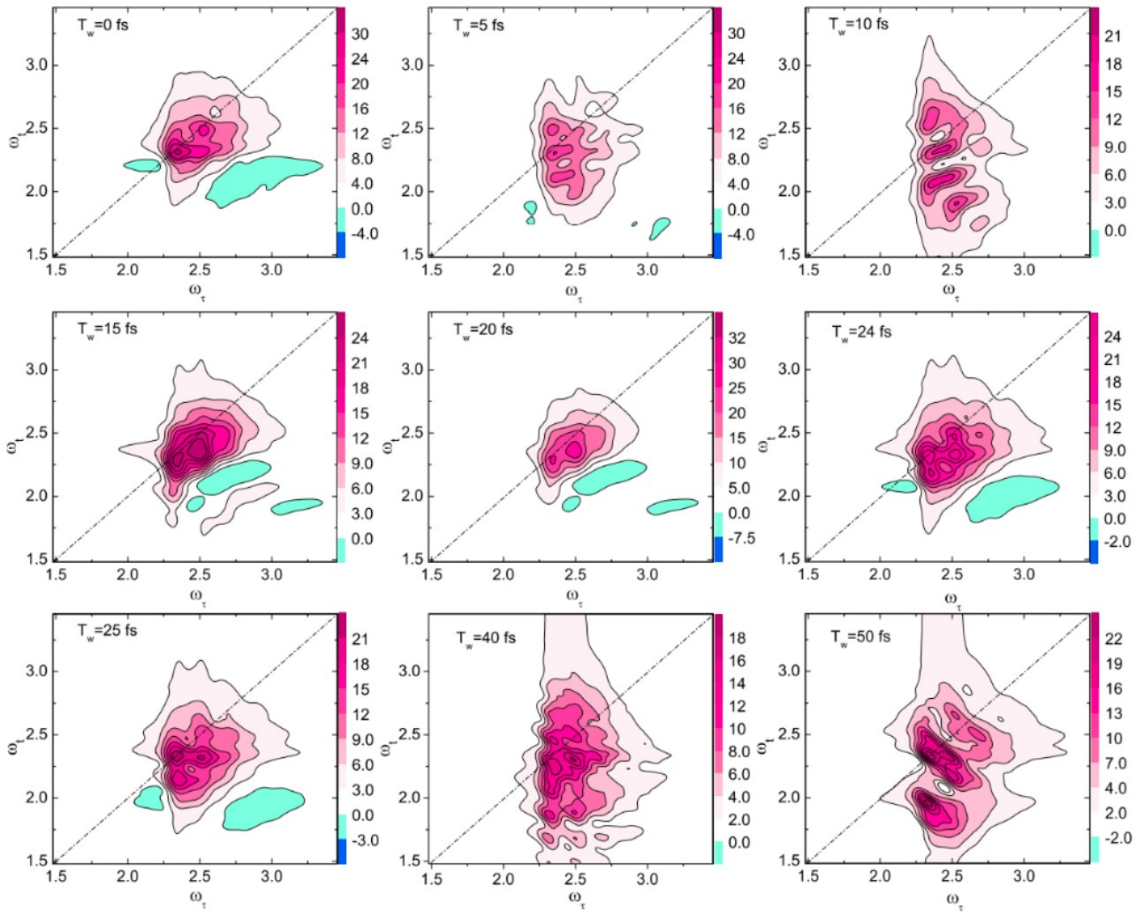

Figure 18: Real parts of the total 2D spectra for the CI-mediated SF model in crystalline rubrene for various waiting times T_w. The parameters $\epsilon_{S1} = 2.50$ eV, $\epsilon_{TT} = 2.58$ eV, $\lambda = 0.05$ eV, and $\eta = 0.2$ are adopted.

Equipped with realistic model parameters, we are in a position to extract dynamical information from the 2D spectra, including the electronic, vibrational, and fission dynamics at CIs in the system. To simulate 2D spectra, we need to evaluate the third-order response functions as described in Sec. 5. We further multiply the response functions by $\exp[-\nu \cdot (\tau + t)]$ with $\nu = 0.033$ eV to account for the optical dephasing. Fig. 18 displays the 2D spectra at different waiting time T_w. The 2D spectrumat $T_w = 0$ fs exhibits pronounced vibrationally structured diagonal peaks that correspond to the vibronic progression in the absorption spectrum. At $T_w = 5$ fs, while the 2D spectrum is dominated by the peaks below the diagonal, there also exist peaks above the diagonal. This reflects the fact that the wave packet moving along the lower adiabatic state e_1 reaches the CI and partially transfers to the higher adiabatic state e_2. The 2D spectrum at $T_w = 10$ fs looks similar to that at $T_w = 5$ fs, albeit with more contributions from the lower adiabatic state e_1. From $T_w = 10$ fs to $T_w = 20$ fs, the peaks below and above the diagonal gradually disappear due to the reverse movement of the wave packet along Ω_{t1} in comparison with the case of the first 10 fs. One can clearly see the recurrence of the 2D spectra as a function of T_w regulated by the tuning mode Ω_{t1} with a vibrational period of 23.8fs (2D spectra at $T_w = 0$ fs and $T_w = 24$ fs), which usually reveals wave packet evolution in the ground (electronic) state due to the fast CI-driven internal conversion to the dark state (see, e.g., the discussion in Ref. [232]). In the present model, however, the CI-driven SF is relatively slow. Hence both stimulated emission and ground-state bleach signals contribute significantly to the 2D spectra on the considered timescale. The evolution of the 2D spectra mainly reflects the wave packet motion along Ω_{t1}. From $T_w = 25$ fs to $T_w = 50$ fs, the peaks below the diagonal emerge, thanks to the wavepacket movement towards the lower potential energy surface of e_1. The aforementioned spectral recurrence is not obvious, and more evolution time is needed to clearly observe the globally periodic movement as there exist two tuning modes (Ω_{t1} and Ω_{t2}) in the model. In conclusion, the 2D spectra computed in our model carry signatures of the excited-state wave packet motion due to the stimulated emission contribution.

7 Davydov Ansätze vs other Gaussian basis-set methods

We have demonstrated that the method of Davydov's Ansätze offers a powerful, versatile toolkit for numerically accurate evaluations of expectation values of steady-state and time-dependent operators for a large variety of many-body systems. In the literature, the HDA approach belongs to a large family of methods which employ time-dependent Gaussian basis functions to accurately solve multi-dimensional time-dependent Schrödinger equations. We should begin with the seminal semiclassical thawed Gaussian approximation (TGA) [233] and frozen Gaussian approximation (FGA) [234] de-

veloped by Heller [235]. In TGA, the center of a Gaussian wavepacket moves according to classical Newtonian equation, while the width is propagated using a time-dependent effective potential obtained by truncating the potential energy surface around the Gaussian center at second order. In FGA, the shape of the wavepacket is frozen, but the nonlinearity of the potential energy surface is approximately taken into account. The variational multi-configurational Gaussian (vMCG) method of Burghardt and coworkers [38, 236, 237], similar to the method of Davydov's Ansätze, employs the time-dependent variational principle to obtain coupled equations of motion for the Gaussian parameters. The multiple spawning (MS) method of Ben-Nun and Martínez [23, 24, 238] uses adaptive linear combinations of Gaussian basis sets following classical nuclear trajectories. Thereby, the number of Gaussian basis functions increases by a process called "spawning," which is designed to accurately describe nonadiabatic dynamics at several coupled potential energy surfaces and/or tunneling effects. Werther and Grossmann developed a complementary strategy and suggested the procedure of apoptosis which removes quasi-degenerate Gaussian wave packets and thereby circumvents the problem of linear dependency of vibrational coherent states [239, 240]. The coupled-coherent states (CCS) method developed by Shalashilin and co-workers [37, 241–243] represents nuclear wave function in a basis of trajectory-guided coherent states that are propagated by an averaged quantum potential. The CCS method has been further extended toward multiple coupled potential energy surfaces, resulting in the MCE method [32–34], which represents wave functions by a linear combination of Ehrenfest configurations guided by mean-field trajectories. The Hagedorn wave packets [244, 245] and the generalized coherent state method [29, 35, 246] employ basis functions consisting of products of Gaussians and multi-dimensional polynomials.

All the Gaussian methods mentioned above differ in the choice of specific basis functions (frozen vs thawed Gaussians, coherent vs squeezed states), in the number of Gaussian wave packets per nuclear degree of freedom, and in specific methods for obtaining equations of motion for the parameters specifying multi-dimensional time-dependent Gaussian wave packets. Nevertheless, the Gaussian nature of the basis functions frequently permits seamless application of the tools developed within the Davydov-Ansatz formalism to other methods in the Gaussian family and vice versa. For example, the methodology combining TFD with the Davydov's Ansätze in Ref. [45] has been successfully applied to the simulations of nonlinear spectroscopic signals via TGA [247, 248] and MCE [249]. The Davydov Ansatz methodology for the computation of nonlinear spectroscopic signals [25, 58] was transferred to the MCE framework [250]. However, the list of possible methodological "exchanges" is by no means exhausted. For example, it is promising to spread the Davydov-Anstaz-based machinery for the evaluation of multidimensional diabatic and adiabatic wave packets [31] to other Gaussian methods

and to interface the Davydov Ansätze with *ab initio* electronic structure methods for on-the-fly simulations of photophysical and spectroscopic responses by adopting the methodologies of *ab initio* multiple spawning (AIMS) [251], *ab initio* multiple cloning (AIMC) [252], the direct dynamics variant of vMCG (DD-vMCG) [253], MCE [254] and (for time-dependent Hamiltonians) the external-field AIMS [255, 256].

8 Conclusion

In this review, we have presented a comprehensive overview of the methodological development of Davydov's Ansätze in the past decade and their applications to many-body quantum systems of interest in computational physical chemistry and chemical physics. Davydov's solitons were proposed in the 1970s as a candidate for vibrational energy carriers in proteins, owing to their close association with the Fröhlich Hamiltonian and the Holstein molecular crystal model. Momentum-space projection of those solitons emerged to be great approximations to the ground-state wave functions to the extended Holstein Hamiltonian, providing unambiguous evidence to the absence of quantum phase transition in the generalized Holstein systems [184, 185]. Pioneered by Shore and Sander in early 1970s, the multiple Davydov Ansätze were first developed as incremental improvements of their single-Ansatz parents to better depict the vibrational portion of the many-body wave function. Two forms of the multiple Davydov Ansätze, namely, the multi-D_1 and the multi-D_2 Ansätze, have been developed and applied successfully to a number of many-body quantum systems of interest, including variants of the SBM [26, 28, 54] and the extended Holstein Hamiltonian in 1D [27, 45] and 2D [257].

Application of HDA to finite-temperature dynamics of many-body systems can be accomplished via the method of Monte Carlo importance sampling to initialize vibrational modes [39, 40], the method of TFD to map the density-matrix Liouville-von Neumann equation to the TFD Schrödinger equation with twice the degrees of freedom [41–45], and the method of displaced number states to exploit the fact that initial excitation of the vibrational manifold can be conveniently described by displaced number states of the bath degrees of freedom [50, 51]. Using the SBM as a demonstration of the finite-temperature time-depedent variation with HDA, variational dynamics with the single Davydov Ansatz already shows excellent agreement with the QUAPI results at high temperatures, while finite-temperature variation with multiple Davydov trial states has been demonstrated to remain efficient even at elevated temperatures [40]. Results in the sub-Ohmic regime demonstrate a great advantage of the HDA method because conventional perturbative approaches fail to describe strong non-Markovianity due to the long-time tail of the correlation function of the sub-Ohmic bath. Comparison of the HDA machinery with the HEOM method has also been carefully made for the

dynamics of the Holstein polaron at finite temperatures [45], which confirms the efficiency and robustness of the HDA machinery for describing the finite-temperature dynamics in the simultaneous presence of diagonal and off-diagona exciton-phonon coupling. As an application in a practical problem, the variational HDA machinery has been extended to the evaluation of third-order response functions of crystalline rubrene at finite temperatures, which yields accurate 2DES signals of two-mode and three-mode models of rubrene from 0 to 300 K.

We can thus conclude that the variational framework of HDA and its finite-temperature variants equip practitioners of quantum simulations with numerically accurate, powerful tools for the evaluation of fully quantum, steady-state and time-dependent, linear and nonlinear responses for a large variety of many-body electron-vibrational systems. It seems auspicious to harness the HDA techniques for numerically accurate and efficient exploration and benchmarking of nonlinear and mode-mode coupling effects in quantum transport and ultrafast spectroscopy, to extend the multi-coherent-state-description to systems with fermionic and rotational degrees of freedom, as well as to systematically apply the HDA machinery to scrutinize the femtosecond dynamics of cavity QED systems and to simulate nonlinear responses of various many-body systems in molecular science to quantum and/or incoherent light.

Acknowledgments

The authors thank Lu Wang, Yiying Yan, Fulu Zheng, Raffaele Borrelli, and Frank Großmann for enlightening discussion. Support from the Singapore Ministry of Education Academic Research Fund Tier 1 (Grant No. RG190/18) is gratefully acknowledged. M.F.G. acknowledges support of Hangzhou Dianzi University through the startup funding.

Conflict of Interest

The authors have declared no conflicts of interest for this article.

*Bibliography

[1] Clarke TM, Durrant JR. Charge photogeneration in organic solar cells. *Chem Rev.* 2010;*110*(11):6736-6767.

[2] Chen LP, Shenai P, Zheng FL, Somoza A, Zhao Y. Optimal energy transfer in light-harvesting systems. *Molecules.* 2015;*20*(8):15224-15272.

[3] Cao JS, Cogdell RJ, Coker DF, Duan HG, Hauer J, Kleinekathöfer U, Jansen TLC, Mancăl T, Miller RJD, Ogilvie JP, Prokhorenko VI, Renger T, Tan HS, Tempelaar R, Thorwart M, Thyrhaug E, Westenhoff S, Zigmantas D. Quantum biology revisited. *Sci Adv.* 2020; *6*(14):eaaz4888.

[4] Cho M. *Two-dimensional Optical Spectroscopy.* CRC Press: New York; 2009.

[5] Hamm P, Zanni M. *Concepts and Methods of 2D Infrared spectroscopy.* Cambridge University Press: Cambridge; 2011.

[6] Mukamel S. *Principles of Nonlinear Optical Spectroscopy.* Oxford University Press: New York; 1995.

[7] Gelin MF, Egorova D, Domcke W. Efficient Calculation of Time- and Frequency-Resolved Four-Wave-Mixing Signals. *Acc Chem Res.* 2009;*42*(9):1290-1298.

[8] Tanimura Y. Stochastic Liouville, Langevin, Fokker-Planck, and master equation approaches to quantum dissipative systems. *J Phys Soc Jpn.* 2006;*75*(8):082001.

[9] Tanimura Y. Numerically "exact" approach to open quantum dynamics: The hierarchical equations of motion (HEOM). *J Chem Phys.* 2020;*153*(2):020901.

[10] Makri N, Makarov DE. Tensor propagator for iterative quantum time evolution of reduced density matrices. I. Theory. *J Chem Phys.* 1995;*102*(11):4600-4610.

[11] Makri N, Makarov DE. Tensor propagator for iterative quantum time evolution of reduced density matrices. II. Numerical methodology. *J Chem Phys.* 1995;*102*(11):4611-4618.

[12] Tanimura Y, Ishizaki A. Modeling, Calculating, and Analyzing Multidimensional Vibrational Spectroscopy. *Acc Chem Res.* 2009;*42*(9):1270-1279.

[13] Tanimura Y. Reduced hierarchy equations of motion approach with Drude plus Brownian spectral distribution: Probing electron transfer processes by means of two-dimensional correlation spectroscopy. *J Chem Phys.* 2012;*137*(22):22A550.

[14] Ikeda T, Tanimura Y. Probing photoisomerization processes by means of multi-dimensional electronic spectroscopy: The multi-state quantum hierarchical Fokker-Planck equation approach. *J Chem Phys.* 2017;*147*(1):014102.

[15] Liang XT. Simulating signatures of two-dimensional electronic spectra of the Fenna-Matthews-Olson complex: By using a numerical path integral. *J Chem Phys.* 2014;*141*(4):044116.

[16] Hu J, Luo M, Jiang F, Xu RX, Yan YJ. Padé spectrum decompositions of quantum distribution functions and optimal hierarchical equations of motion construction for quantum open systems. *J Chem Phys.* 2011;*134*(24):244106.

[17] Tang Z, Ouyang XQ; Gong Z, Wang H, Wu JL. Extended hierarchy equations of motion for the spin-boson model. *J Chem Phys.* 2015;*143*(22):224112.

[18] Rahman H, Kleinekathöfer U. Chebyshev hierarchical equations of motion for systems with arbitrary spectral densities and temperatures. *J Chem Phys.* 2019;*150*(24):244104.

[19] Beck MH, Jäckle A, Worth GA, Meyer HD. The Multiconfiguration Time-Dependent Hartree (MCTDH) Method: A Highly Efficient Algorithm for Propagating Wave packets. *Phys Rep.* 2000;*324*(1):1-105.

[20] Worth GA, Meyer HD, Köppel H, Cederbaum LS, Burghardt I. Using the MCTDH Wavepacket Propagation Method to Describe Multimode Non-Adiabatic Dynamics. *Int Rev Phys Chem.* 2008;*27*(3):569-606.

[21] Wang HB, Thoss M. Multilayer formulation of the multiconfiguration time-dependent Hartree theory. *J Chem Phys.* 2003;*119*(3):1289.

[22] Manthe U. A multilayer multiconfigurational time-dependent Hartree approach for quantum dynamics on general potential energy surfaces. *J Chem Phys.* 2008;*128*(16):164116.

[23] Ben-Nun M, Martínez TJ. Nonadiabatic Molecular Dynamics: Validation of the Multiple Spawning Method for a Multidimensional Problem. *J Chem Phys.* 1998;*108*(17):7244-7257.

[24] Ben-Nun M, Martínez TJ. A multiple spawning approach to tunneling dynamics. *J Chem Phys.* 2000;*112*(14):6113-6121.

[25] Huynh T, Sun K, Gelin MF, Zhao Y. Polaron dynamics in two-dimensional photon-echo spectroscopy of molecular rings. *J Chem Phys.* 2013;*139*(10):104103.

[26] Zhou N, Huang Z, Zhu J, Chernyak V, Zhao Y. Polaron dynamics with a multitude of Davydov D_2 trial states. *J Chem Phys.* 2015;*143*(1):014113.

[27] Zhou N, Chen L, Huang Z, Sun K., Tanimura Y, Zhao Y. Fast, Accurate Simulation of Polaron Dynamics and Multidimensional Spectroscopy by Multiple Davydov Trial State. *J Phys Chem A.* 2016;*120*(9):1562-1576.

[28] Deng T, Yan Y, Chen L, Zhao Y. Dynamics of the two-spin spin-boson model with a common bath. *J Chem Phys*. 2016;*144*(14):144102.

[29] Chen L, Borrelli R, Zhao Y. Dynamics of Coupled Electron-Boson Systems with the Multiple Davydov D_1 Ansatz and the Generalized Coherent State. *J Phys Chem A*. 2017;*121*(46):8757-8770.

[30] Chen L, Gelin MF, Zhao Y. Dynamics of the spin-boson model: A comparison of the multiple Davydov D_1, $D_{1.5}$, D_2 Ansätze. *Chem Phys*. 2018;*515*(14):108-118.

[31] Chen L, Gelin MF, Domcke W. Multimode quantum dynamics with multiple Davydov D_2 trial states: Application to a 24-dimensional conical intersection model. *J Chem Phys*. 2019;*150*(2):024101.

[32] Shalashilin DV. Quantum mechanics with the basis set guided by Ehrenfest trajectories: Theory and application to spin-boson model. *J Chem Phys*. 2009;*130*(24):244101.

[33] Shalashilin DV. Nonadiabatic dynamics with the help of multiconfigurational Ehrenfest method: Improved theory and fully quantum 24D simulation of pyrazine. *J Chem Phys*. 2010;*132*(24):244111.

[34] Chen LP, Gelin MF, Shalashilin DV. Dynamics of a one-dimensional Holstein polaron: The multiconfigurational Ehrenfest method. *J Chem Phys*. 2019;*151*(24):244116.

[35] Borrelli R, Gelin MF. The Generalized Coherent State ansatz: Application to quantum electron-vibrational dynamics. *Chem Phys*. 2016;*481*:91-98.

[36] Burghardt I, Giri K, Worth GA. Multimode quantum dynamics using Gaussian wavepackets: The Gaussian-based multiconfiguration time-dependent Hartree (G-MCTDH) method applied to the absorption spectrum of pyrazine. *J Chem Phys*. 2008;*129*(17):174104.

[37] Shalashilin DV, Child MS. The Phase Space CCS Approach to Quantum and Semiclassical Molecular Dynamics for High-dimensional System. *Chem Phys*. 2004;*304*:103-120.

[38] Richings GW, Polyak I, Spinlove KE, Worth GA, Burghardt I, Lasorne B. Quantum dynamics simulations using Gaussian wave packets; the vMCG method. *Int Rev Phys Chem*. 2015;*34*(2):269-308.

[39] Wang H, Thoss M. Quantum-mechanical evaluation of the Boltzmann operator in correlation functions for large molecular systems: A multilayer multiconfiguration time-dependent Hartree approach. *J Chem Phys.* 2006;*124*(3):034114.

[40] Wang L, Fujihashi Y, Chen LP, Zhao Y. Finite-temperature time-dependent variation with multiple Davydov states. *J Chem Phys.* 2017;*146*(12):124127.

[41] Suzuki M. Thermo Field Dynamics in Equilibrium and Non-Equilibrium Interacting Quantum Systems. *J Phys Soc Jpn.* 1985;*54*(12):4483-4485.

[42] Takahashi Y, Umezawa H. Thermo Field Dynamics. *Int J Mod Phys B.* 1996;*10*(13n14):1755-1805.

[43] Borrelli R, Gelin MF. Quantum electron-vibrational dynamics at finite temperature: Thermo field dynamics approach. *J Chem Phys.* 2016;*145*(22):224101.

[44] Borrelli R, Gelin MF. Simulation of Quantum Dynamics of Excitonic Systems at Finite Temperature: an efficient method based on Thermo Field Dynamics. *Sci Rep.* 2017;*7*:9127.

[45] Chen LP, Zhao Y. Finite temperature dynamics of a Holstein polaron: The thermo-field dynamics approach. *J Chem Phys.* 2017;*147*(21):214102.

[46] Reddy CS, Prasad MD. Finite temperature vibronic spectra of harmonic surfaces: a time-dependent coupled cluster approach. *Mol Phys.* 2015;*113*(19-20):3023-3030.

[47] Begušić T, Vaníček J. On-the-fly ab initio semiclassical evaluation of vibronic spectra at finite temperature. *J Chem Phys.* 2020;*153*(2):024105.

[48] Harsha G, Henderson TM, Scuseria GE. Thermofield theory for finite-temperature quantum chemistry. *J Chem Phys.* 2019;*150*(15):154109.

[49] Harsha G, Henderson TM, Scuseria GE. Thermofield Theory for Finite-Temperature Coupled Cluster. *J Chem Theory Comput.* 2019;*15*(11):6127-6136.

[50] Werther M, Grossmann F, Huang ZK, Zhao Y. Davydov-Ansatz for Landau-Zener-Stueckelberg-Majorana transitions in an environment: Tuning the survival probability via number state excitation. *J Chem Phys.* 2019;**150**(23):234109.

[51] Hu WJ, Sun KW, Xu Q, Chen LP, Zhao Y. Ultrafast dynamics in rubrene and its spectroscopic manifestation. *J Chem Phys.* 2020;*153*(17):174105.

[52] Luo B, Ye J, Guan C, Zhao Y. Validity of time-dependent trial states for the Holstein polaron. *Phys Chem Chem Phys*. 2010; *12*(45):15073-15084.

[53] Sun J, Luo B, Zhao Y. Dynamics of a one-dimensional Holstein polaron with the Davydov Ansatze. *Phys Rev B*. 2010;*82*(1):014305.

[54] Wang L, Chen LP, Zhou NJ, Zhao Y. Variational dynamics of the sub-Ohmic spin-boson model on the basis of multiple Davydov D_1 states. *J Chem Phys*. 2016;*144*(2):024101.

[55] Huang Z, Wang L, Wu C, Chen L, Grossmann F, Zhao Y. Polaron dynamics with off-diagonal coupling: beyond the Ehrenfest approximation. *Phys Chem Chem Phys*. 2017;*19*(2):1655-1668.

[56] Huang Z, Chen L, Zhou N, Zhao Y. Transient dynamics of a one-dimensional Holstein polaron under the influence of an external electric field. *Ann Phys*. 2017;*529*(5):1600367.

[57] Chen L, Gelin MF, Domcke W, Zhao Y. Theory of femtosecond coherent double-pump single-molecule spectroscopy: application to light harvesting complexes. *J Chem Phys*. 2015;*142*(16):164106.

[58] Sun KW, Gelin MF, Chernyak V, Zhao Y. Davydov ansatz as an efficient tool for the simulation of nonlinear optical response of molecular aggregates. *J Chem Phys*. 2015;*142*(21):212448.

[59] Davydov AS. The theory of contraction of proteins under their excitation. *J Theor Biol*. 1973;*38*(3):559-569.

[60] Davydov AS. *Theory of Molecular Excitons*. Plenum Press: New York-London; 1971.

[61] Davydov AS. Deformation of Molecular Crystals at Electronic Excitation. *Phys Stat Sol*. 1969;*36*(1):211-219.

[62] Scott AC. The laser-Raman spectrum of a Davydov soliton. *Phys Lett A*. 1981;*86*(1):60-62.

[63] Careri G, Buontempo U, Carta F, Gratton E, Scott AC. Infrared Absorption in Acetanilide by Solitons. *Phys Rev Lett*. 1983;*51*(4):304.

[64] Scott AC. Dynamics of Davydov solitons. *Phys Rev A*. 1982;*26*(1):578.

[65] Davydov AS, Kislukha N. Solitary excitons in one-dimensional molecular chains. *Phys Stat Sol*. 1973;*59*(2):465-470.

[66] Davydov AS. Dvizhenie solitona v odnomernoi molekulyarnoi reshetke s uchetom teplovih kolebanii. *Zh Eksp Teor Fiz*. 1980;*78*:789.

[67] Scott AC. Davydov's soliton. *Phys Rep.* 1992;*217*(1):1-67.

[68] Škrinjar MJ, Kapor DV, Stojonović SD. Classical and quantum approach to Davydovs soliton theory. *Phys Rev A.* 1988;*38*(12):6402-6407.

[69] Zhang Q, Romero-Rochin V, Silbey R. Variational approach to the Davydov soliton. *Phys Rev A.* 1988;*38*(12):6408-6415.

[70] Bernstein L, Eilbeck JC, Scott AC. The quantum theory of local modes in a coupled system of nonlinear oscillators. *Nonlinearity.* 1990;*3*(2):293.

[71] Zhao Y, Brown DW. Robustness of the single dressing fraction characterization of polaron structure in multi-mode partial dressing theory. *J Lumin.* 1994;*58*(1-6):61-65.

[72] Plodzien M, Sowinski T, Kokkelmans S. Simulating polaron biophysics with Rydberg atoms. *Sci Rep.* 2018;*8*:9247.

[73] Georgiev DD, Glazebrook JF. On the quantum dynamics of Davydov solitons in protein alpha-helices. *Physica A.* 2019;*517*:257-269.

[74] Čápek V, Krausová D. To the relation between energies of molecular soliton and extended states in chains. *Czech J Phys B.* 1987;*37*:1201-1202.

[75] Toyozawa Y. Self-Trapping of an Electron by the Acoustical Mode of Lattice Vibration. I. *Prog Theor Phys.* 1961;*26*(1): 29-44.

[76] Merrifield RE. Theory of the Vibrational Structure of Molecular Exciton States. *J Chem Phys.* 1964;*40*(2):445.

[77] Shore HB, Sander LM. Ground State of the Exciton-Phonon System. *Phys Rev B.* 1973;*7*(10):4537.

[78] Venzl G, Fischer SF. Theory of exciton-phonon coupling in one-dimensional molecular crystals: A variational treatment with delocalized solitary states. *Phys Rev B.* 1985;*32*(10):6437.

[79] Zhao Y. *Doctoral thesis.* University of California: San Diego; 1994.

[80] Zhao Y, Brown D, Lindenberg K. A Variational Approach to Nonlocal Exciton-Phonon Coupling. *J Chem Phys.* 1997;*106*(7): 2728.

[81] Zhao Y, Brown D, and Lindenberg K. Variational Energy Band Theory for Polarons: Mapping Polaron Structure with the Merrifield Method, *J Chem Phys.* 1997;*106*(13):5622.

[82] Zhao Y, Brown D, and Lindenberg K. Variational Energy Band Theory for Polarons: Mapping Polaron Structure with the Toyozawa Method. *J Chem Phys.* 1997;*107*(8):3159.

[83] Zhao Y, Brown D, and Lindenberg K. Variational Energy Band Theory for Polarons: Mapping Polaron Structure with the Global-Local Method. *J Chem Phys.* 1997;*107*(8):3179.

[84] Sun J, Duan L, Zhao Y, Delocalized Davydov D_1 Ansatz for the Holstein Polaron. *J Chem Phys.* 2013;*138*(17):174116.

[85] Zhou N, Chen L, Zhao Y, Mozyrsky D, Chernyak V, Zhao Y. Ground state properties of sub-Ohmic spin-boson model with simultaneous diagonal and off-diagonal coupling. *Phys Rev B.* 2014;*90*(15):155135.

[86] Zakharov VE, Shabat AB. Exact theory of two-dimensional self-focusing and one-dimensional self-modulation of waves in nonlinear media. *Zh Eksp Theor Fiz.* 1971;*61*:118-134.

[87] Fröhlich H. Theory of electrical breakdown in ionic crystals. *Proc Roy Soc A.* 1937;*160*(901):230; Fröhlich H. Electrons in lattice fields. *Adv Phys.* 1954;*3*(11):325-361.

[88] Emin D, Hillery MS. Formation of a large singlet bipolaron: Application to high-temperature bipolaronic superconductivity. *Phys Rev B.* 1989;*39*(10):6575.

[89] Wang XF, Lei XL. A simple description of Fröhlich interaction in cylindrical GaAs/AlAs quantum wires. *Sol Stat Comm.* 1994;*91*(7):513-517.

[90] Zhou HY, Gu SW. Strong coupling polaron in quantum well wire. *Sol Stat Comm.* 1994;*91*(9):725-729.

[91] Niu Q, Ao P, Thouless DJ. From Feynmans wave function to the effective theory of vortex dynamics. *Phys Rev Lett.* 1994;*72*(11):1706.

[92] Feynman RP. Slow Electrons in a Polar Crystal. *Phys Rev.* 1955;*97*(3):660.

[93] Lee TD. *Particle Physics and Introduction to Field Theory, Contemporary Concepts in Physics, Vol. 1.* Harwood Academic Publishers: New York; 1988.

[94] Wang X, Brown DW, Lindenberg K. Quantum Monte Carlo Simulations of the Davydov Model. *Phys Rev Lett.* 1989;*62*(15):1796.

[95] Wang X, Brown DW, Campbell DK. Equivalence of the Holstein Polaron to an One-Dimension Classical Gas. *Phys Lett A.* 1993;*181*(2):123-128.

[96] Limdahl PS, Kerr WC. Do Davydov Solitons Exist at 300 K?. *Phys Rev Lett.* 1985;*55*(11):1235-1238.

[97] Förner W. Davydov solition dynamics-temperature effects. *J Phys Cond Matt.* 1991;*3*(24):4333-4348.

[98] Förner W. Davydov solition dynamics: Initial state, boundary conditions, and numerical procedure. *J Comp Chem.* 1992;*13*(3):275-313.

[99] Förner W. Quantum and temperature effects on Davydov soliton dynamics. III. Interchain coupling. *J Phys Cond Matt.* 1993;*5*(7):823-840.

[100] Ivić Z, Brown DW. Soliton excitations of a small-polaron band. *Phys Rev Lett.* 1989;*63*(4):426; Brown DW, Ivić Z. Unification of polaron and soliton theories of exciton transport. *Phys Rev B.* 1989;*40*(14):9876.

[101] Feinberg D, Ciuchi S, de Pasquale F. Squeezing phenomena in interacting electron-phonon systems. *Int J Mod Phys B.* 1990;*4*(07n08):1317-1367.

[102] Werther M, Grossmann F. The Davydov D1.5 Ansatz for the quantum Rabi model. *Phys Scr.* 2018;*93*(7):074001.

[103] Sun KW, Xie WW, Chen LP, Domcke W, Gelin MF. Multi-faceted spectroscopic mapping of ultrafast nonadiabatic dynamics near conical intersections: A computational study. *J Chem Phys.* 2020;*153*(17):174111.

[104] Jakucionis M, Mancal T, Abramavicious D. Modeling irreversible molecular internal conversion using the time-dependent variational approach with sD_2 Ansatz. *Phys. Chem. Chem. Phys.* 2020;22(16):8952-8962.

[105] Werther M, Großmann F. Stabilization of adiabatic population transfer by strong coupling to a phonon bath. *Phys. Rev. A.* 2020;102(6):063710.

[106] Yan Y, Chen L, Luo J, Zhao Y. Variational approach to time-dependent fluorescence of a driven qubit. *Phys. Rev. A.* 2020;102(2):023714.

[107] Glauber RJ. Coherent and Incoherent States of the Radiation Field. *Phys Rev.* 1963;*131*(6):2766.

[108] Sudarshan ECG. Equivalence of Semiclassical and Quantum Mechanical Descriptions of Statistical Light Beams. *Phys Rev Lett.* 1963;*10*(7):277.

[109] Hillery M, O'connell RF, Scully MO, Wigner EP. Distribution functions in physics: Fundamentals. *Phys Rep.* 1984;*106*(3):121-167.

[110] Umezawa H, Matsumoto H, Tachiki M. *Thermo field dynamics and condensed states.* North-Holland; 1982.

[111] Ojima I. Gauge fields at finite temperatures-Thermo field dynamics and the KMS condition and their extension to gauge theories. *Annals of Physics*, 1981;*137*(1):1-32.

[112] Suzuki M. Density matrix formalism, double-space and thermo field dynamics in nonequilibrium dissipative systems. *Int J Mod Phys B.* 1991;*5*(11):1821-1842.

[113] Oseledets IV. Tensor-Train Decomposition. *SIAM J Sci Comput.* 2011;*33*(5):2295-2317.

[114] Haegeman J, Lubich C, Oseledets I, Vandereycken B, Verstraete F. Unifying time evolution and optimization with matrix product states. *Phys Rev B.* 2016;*94*(16):165116.

[115] Borrelli R, Gelin MF. Finite temperature quantum dynamics of complex systems: Integrating thermo-field theories and tensor-train methods. *WIREs Comput Mol Sci.* 2021;e1539.

[116] Feiguin AE, White SR. Finite-temperature density matrix renormalization using an enlarged Hilbert space. *Phys. Rev. B.* 2005;*72*(22):220401R.

[117] Paeckel S, Köler T, Swoboda A, Manmana SR, Schollwök U, Hubig C. Time-evolution methods for matrix-product states. *Ann. Phys.* 2019;*411*:167998.

[118] Baiardi A, Reiher M. The density matrix renormalization group in chemistry and molecular physics: Recent developments and new challenges. *J Chem Phys.* 2020;*152*(4):040903.

[119] Domcke W, Stock G. Theory of Ultrafast Nonadiabatic Excited-State Processes and their Spectroscopic Detection in Real Time. *Adv Chem Phys.* 1997;*100*:1-169.

[120] Koppel H, Domcke W, Cederbaum LS. Multimode Molecular Dynamics Beyond the Born-Oppenheimer Approximation. *Adv Chem Phys.* 1984;*57*:59-246.

[121] Mukamel S, Abramavicius D. Many-Body Approaches for Simulating Coherent Nonlinear Spectroscopies of Electronic and Vibrational Excitons. *Chem Rev.* 2004;*104*(4):2073-2098.

[122] Abramavicius D, Palmieri B, Voronine DV, Sanda F, Mukamel S. Coherent Multidimensional Optical Spectroscopy of Excitons in Molecular Aggreagtes; Quasiparticle vs Supermolecule Perspective. *Chem Rev.* 2009;*109*(6), 2350-2408.

[123] Chen D, Ye J, Zhang H, Zhao Y. On the Munn–Silbey approach to polaron transport with off-diagonal coupling and temperature- dependent canonical transformations. *J Phys Chem B.* 2011;*115*(18):5312-5321.

[124] Oberhofer H, Reuter K, Blumberger J. Charge Transport in Molecular Materials: An Assessment of Computational Methods. *Chem Rev.* 2017;*117*(15):10319-10357.

[125] Gelin MF, Borrelli R. Thermal Schröinger Equation: Efficient Tool for Simulation of Many-Body Quantum Dynamics at Finite Temperature. *Ann Phys.* 2017;*529*(12):1700200.

[126] Sun KW, Yao Y. Beating maps of singlet fission: Simulation of coherent two-dimensional electronic spectroscopy by Davydov ansatz in organic molecules. *J Chem Phys.* 2017;*147*(22):224905 (2017).

[127] Zhao Y, Knox RS. A Brownian Oscillator Approach to the Kennard-Stepanov Relation. *J Phys Chem A.* 2000;*104*(33):7751-7761.

[128] Su L, Tok A, Zhao Y, Ng N, Boey F, Woodhead J, Summers CJ. Electron-phonon interactions in ce3+-doped yttrium aluminum garnet nanophosphors. *J Phys Chem B.* 2008;*112*(35):10830-10832.

[129] Chorosajev V, Marciulionis T, Abramavicius D. Temporal dynamics of excitonic states with nonlinear electron-vibrational coupling. *Journal of Chemical Physics.* 2017;147(7):074114.

[130] Leggett AJ, Chakravarty S, Dorsey, AT, Fisher MPA, Garg A, Zwerger W. Dynamics of the dissipative two-state system. *Rev. Mod. Phys.* 1987;*59*(1):1-85.

[131] Lü Z, Zheng H. Quantum dynamics of the dissipative two-state system coupled with a sub-Ohmic bath. *Phys Rev B.* 2007;*75*(5):054302.

[132] Wang Q, Hu AY, Zheng H. Analytical approach to dynamical behavior and phase diagrams in dissipative two-state systems. *Phys Rev B.* 2009;*80*(21):214301.

[133] Wang H, Thoss M. From coherent motion to localization: dynamics of the spin-boson model at zero temperature. *New J Phys.* 2008;*10*:115005.

[134] Wang H, Thoss M. From coherent motion to localization: II. Dynamics of the spin-boson model with sub-Ohmic spectral density at zero temperature. *Chem Phys.* 2010;*370*(1-3):78-86.

[135] Nalbach P, Thorwart M. Crossover from coherent to incoherent quantum dynamics due to sub-Ohmic dephasing. *Phys Rev B.* 2013;*87*(1):014116.

[136] Kast D, Ankerhold J. Persistence of Coherent Quantum Dynamics at Strong Dissipation. *Phys Rev Lett.* 2013;*110*(1):010402.

[137] Nalbach P, Thorwart M. Ultraslow quantum dynamics in a sub-Ohmic heat bath. *Phys Rev B.* 2010;*81*(5):054308.

[138] Bulla R, Tong NH, Vojta M. Numerical Renormalization Group for Bosonic Systems and Application to the Sub-Ohmic Spin-Boson Model. *Phys Rev Lett.* 2003;*91*(17):170601; Vojta M, Tong NH, Bulla R. Quantum Phase Transitions in the Sub-Ohmic Spin-Boson Model: Failure of the Quantum-Classical Mapping. *Phys Rev Lett.* 2005;*94*(7):070604; Anders FB, Bulla R, Vojta M. Equilibrium and Nonequilibrium Dynamics of the Sub-Ohmic Spin-Boson Model. *Phys Rev Lett.* 2007;*98*(21):210402.

[139] Orth PP, Roosen D, Hofstetter W, Hur KL. Dynamics, synchronization, and quantum phase transitions of two dissipative spins. *Phys Rev B.* 2010;*82*(14):144423.

[140] McCutcheon DPS, Nazir A, Bose S, Fisher AJ. Separation-dependent localization in a two-impurity spin-boson model. *Phys Rev B.* 2010;*81*(23):235321.

[141] Wang C, Chen QH. Exact dynamics of quantum correlations of two qubits coupled to bosonic baths. *New J Phys.* 2013;*15*:103020.

[142] Lv Z, Duan L, Li X, Shenai PM, Zhao Y. Sub-Ohmic spin-boson model with off-diagonal coupling: Ground state properties. *J Chem Phys.* 2013;*139*(16):164103.

[143] Zhao Y, Yao Y, Chernyak V, Zhao Y. Communication: Spin-boson model with diagonal and off-diagonal coupling to two independent baths: Ground-state phase transition in the deep sub-Ohmic regime. *J Chem Phys.* 2014;*140*(16):161105.

[144] Zhou NJ, Chen LP, Xu D, Chernyak V, Zhao Y. Symmetry and the critical phase of the two-bath spin-boson model: Ground-state properties. *Phys Rev B.* 2015;*91*(19):195129.

[145] Kotov VN, Oitmaa J, Sushkov O. Local magnetic impurities in the two-dimensional quantum Heisenberg antiferromagnet. *Phys Rev B.* 1998;*58*(13):8500.

[146] Vojta M, Buragohain C, Sachdev S. Quantum impurity dynamics in two-dimensional antiferromagnets and superconductors. *Phys Rev B.* 2000;*61*(22):15152.

[147] Neto AHC, Novais E, Borda L, Zaránd G, Affleck I. Quantum Magnetic Impurities in Magnetically Ordered Systems. *Phys Rev Lett.* 2003;*91*(9):096401.

[148] Khveshchenko DV. Quantum impurity models of noisy qubits. *Phys Rev B*. 2004;*69*(15):153311.

[149] Pachón LA, Brumer P. Incoherent excitation of thermally equilibrated open quantum systems. *Phys Rev A*. 2013;*87*(2):022106.

[150] You JQ, Nori F. Superconducting Circuits and Quantum Information. *Physics Today*. 2005;*58*(11):42.

[151] Cárdenas PC, Paternostro M, Semião FL. Non-Markovian qubit dynamics in a circuit-QED setup. *Phys Rev A*. 2015;*91*(2):022122.

[152] Raftery J, Sadri D, Schmidt S, Türeci HE, Houck AA. Observation of a Dissipation-Induced Classical to Quantum Transition. *Phys Rev X*. 2014;*4*(3):031043.

[153] Liao JQ, Kuang LM. Generation of entangled coherent states of two cavity fields via coupling to a SQUID-based charge qubit. *J Phys B: At Mol Opt Phys*. 2007;*40*(10):1845.

[154] Ruokola T, Ojanen T. Thermal conductance in a spin-boson model: Cotunneling and low-temperature properties. *Phys Rev B*. 2011;*83*(4):045417.

[155] Sengupta AM. Spin in a fluctuating field: The Bose(+Fermi) Kondo models. *Phys Rev B*. 2000;*61*(6):4041.

[156] Zhu L, Si Q. Critical local-moment fluctuations in the Bose-Fermi Kondo model. *Phys Rev B*. 2002;*66*(2):024426; Zarand G, Demler E. Quantum phase transitions in the Bose-Fermi Kondo model. *Phys Rev B*. 2002;*66*(2):024427.

[157] Guo C, Weichselbaum A, Delft JV, Vojta M, Critical and Strong-Coupling Phases in One- and Two-Bath Spin-Boson Models. *Phys Rev Lett*. 2012;*108*(16):160401.

[158] Wubs M, Saito K, Kohler S, Hänggi P, Kayanuma Y. Gauging a Quantum Heat Bath with Dissipative Landau-Zener Transitions. *Phys Rev Lett*. 2006;*97*(20):200404.

[159] Whitney RS, Clusel M, Ziman T. Temperature Can Enhance Coherent Oscillations at a Landau-Zener Transition. *Phys Rev Lett*. 2011;*107*(21):210402.

[160] Saito K, Wubs M, Kohler S, Kayanuma Y, Hänggi P. Dissipative Landau-Zener transitions of a qubit: Bath-specific and universal behavior. *Phys Rev B*. 2007;*75*(21):214308.

[161] Saito K, Wubs M, Kohler S, Hänggi P, Kayanuma Y. Quantum state preparation in circuit QED via Landau-Zener tunneling. *Europhysics Lett*. 2006;*76*(1):22.

[162] Wang L, Zheng F, Wang J, Grossmann F, Zhao Y. Schrödinger-cat states in Landau-Zener-Stueckelberg-Majorana interferometry: a multiple Davydov Ansatz approach. *J Phys Chem B.* 2021;*125*(12):3184-3196.

[163] Zheng F, Shen Y, Sun K, Zhao Y. Photon-assisted Landau-Zener transitions in a periodically driven Rabi dimer coupled to a dissipative mode. *J Chem Phys.* 2021;*154*(4):044102.

[164] Huang Z, Zheng F, Zhang Y, Wei Y, Zhao Y. Dissipative dynamics in a tunable Rabi dimer with periodic harmonic driving. *J Chem Phys.* 2019;*150*(18):184116.

[165] Zheng F, Zhang Y, Wei Y, Zhao Y. Engineering photon delocalization in a Rabi dimer with a dissipative bath. *Annalen der Physik.* 2018;*530*(12):1800351.

[166] Holstien T. Studies of polaron motion: Part I. The molecular-crystal model. *Annals of Phys.* 1959;*8*(3):325-342.

[167] Lee TD, Low FE, Pines D. The Motion of Slow Electrons in a Polar Crystal. *Phys Rev.* 1953;*90*(2):297.

[168] Whitfield G, Puff R. Weak-Coupling Theory of the Polaron Energy-Momentum Relation. *Phys Rev.* 1965;*139*(1A):A338.

[169] Larsen DM. Polaron Energy Spectrum. *Phys Rev.* 1966;*144*(2):697.

[170] Sumi H. Exciton Polarons of Molecular Crystal Model. I. CDynamical CPAC. *J Phys Soc Jpn.* 1974;*36*(3):770-779.

[171] Sumi A, Toyozawa Y. Discontinuity in the Polaron Ground State. *J Phys Soc Jpn.* 1973;*35*(1):137-145.

[172] Toyozawa Y, Shinozuka Y. Stability of an Electron in Deformable Lattice -Force Range, Dimensionality and Potential Barrier-. *J Phys Soc Jpn.* 1980;*48*(2):472-478.

[173] Peeters FM, Devreese JT. Acoustical polaron in three dimensions: The ground-state energy and the self-trapping transition. *Phys Rev B.* 1985;*32*(6):3515.

[174] Spohn H. Roughening and pinning transitions for the polaron. *J Phys A: Math Gen.* 1986;*19*(4):533.

[175] Shoji H, Tokuda N. Phase-transition-like behaviour in the problems of different types of polaron. *J Phys C: Solid State Phys.* 1981;*14*(9):1231.

[176] Mańka R. The first-order phase transition in the large polaron ground state. *Phys Lett A*. 1978;*67*(4):311-312.

[177] Sun K, Ye J, Zhao Y. Path induced coherent energy transfer in light-harvesting complexes in purple bacteria. *J Chem Phys.* 2014;*141*(12):124103.

[178] Ye J, Sun K, Zhao Y, Yu Y, Lee C K, Cao J. Excitonic energy transfer in light-harvesting complexes in purple bacteria. *J Chem Phys.* 2012;*136*(24):245104.

[179] Yang G, Wu N, Chen T, Sun K, Zhao Y. Theoretical Examination of Long-range Energy Propagation in Nano-Engineered Light Harvesting Antenna Arrays. *J Phys Chem B.* 2012;*116*(5):3747-3756.

[180] Prelovšek P. On the existence of a sharp transition in the coupled spin-1/2-phonon system. *J Phys C: Solid State Phys.* 1979;*12*(10):1855-1868.

[181] Lagendijk A, De Raedt H. On self-trapping in the molecular crystal model in onw, two and three dimensions. *Phys Lett A*. 1985;*108*(2):91-94.

[182] Scherer POJ, Knapp EW, Fischer SF. Exciton-phonon self-trapping: A continuous transition. *Chem Phys Lett.* 1984;*106*(3):191-196.

[183] Yarkony D, Silbey R. Comments on exciton phonon coupling: Temperature dependence. *J Chem Phys.* 1976;*65*(3):1042.

[184] Gerlach B, Löwen H. Proof of the nonexistence of (formal) phase transitions in polaron systems. I. *Phys Rev B.* 1987;*35*(9):4291.

[185] Löwen H. Absence of phase transitions in Holstein systems. *Phys Rev B.* 1988;*37*(15):8661.

[186] Gosar P, Vilfan I. Phonon-assisted current in organic molecular crystals. *Mol Phys.* 1970;*18*(1):49-61.

[187] Sumi H. Origin of temperature-independent electron mobilities in organic molecular crystals. *Solid State Commun.* 1978;*28*(4):309-312; Sumi H. Theory of electrical conduction in organic molecular crystals: Temperature-independent mobilities. *J Chem Phys.* 1979;*70*(8):3775.

[188] Madhukar A, Post W. Exact Solution for the Diffusion of a Particle in a Medium with Site Diagonal and Off-Diagonal Dynamic Disorder. *Phys Rev Lett.* 1977;*39*(22):1424.

[189] Vilfan, "Conference on Organic Conductors and Semiconductors, Siófok, Hungary 1976", pp. 629; I. Vilfan, in *Organic Conductors and Semiconductors*, Lecture Notes in Physics, Vol. 65, edited by J. Ehlers, K. Hepp, R. Kippenhahn, H. A. Weidenmüller, and d J. Zittartz (Springer Verlag, Heidelberg, 1977), p. 629

[190] Schein LB, Duke CB, McGhie AR. Observation of the Band-Hopping Transition for Electrons in Naphthalene. *Phys Rev Lett.* 1978;*40*(3):197; Schein LB. Electron drift mobilities over wide temperature ranges in anthracene, deuterated anthracene and As2S3. *Chem Phys Lett.* 1977;*48*(3):571-579; Duke CB, Schein LB. Organic solids: is energy-band theory enough?. *Physics Today.* 1980;*33*(2):42.

[191] Efrima S, Metiu H. The temperature dependence of the electron mobility in molecular crystals. *Chem Phys Lett.* 1979;*60*(2):226-231.

[192] Roberts GG, Apsley N, Munn RW., Temperature dependent electronic conduction in semiconductors. *Phys Rep.* 1980;*60*(2):59-150.

[193] Munn RW, Silbey R. Theory of electronic transport in molecular crystals. II. Zeroth order states incorporating nonlocal linear electronCphonon coupling. *J Chem Phys.* 1985;*83*(4):1843; Munn RW, Silbey R. Theory of electronic transport in molecular crystals. III. Diffusion coefficient incorporating nonlocal linear electronCphonon coupling. *J Chem Phys.* 1985;*83*(4):1854.

[194] Song KS. Calculation on Vk-Centres in Alkali Halides. *J Phys Soc Jpn.* 1969;*26*(5):1131-1139.

[195] Umehara M. On a Self-Trapped Acoustic Polaron with the Site Diagonal and Site Off-Diagonal Electron-Phonon Interaction. *J Phys Soc Jpn.* 1979;*47*:852-860.

[196] Das TP, Jette AN, Knox RS. Theory of the Optical and Magnetic Properties of the Self-Trapped Hole in Lithium Fluoride. *Phys Rev.* 1964;*134*(4A):A1079.

[197] Umehara M. Importance of the site-off-diagonal electron-phonon interaction on the self-trapped small magnetic polaron. *Phys Rev B.* 1983;*27*(9):5669.

[198] Sumi H. Two kinds of excimers in -perylene and pyrene crystals: Origin of Y and V emissions. *Chem Phys.* 1989;*130*(1-3),433-449.

[199] Mahan GD. *Many-Particle Physics.* Plenum Press: New York; 1981.

[200] Zhao Y, Brown DW, Lindenberg K. On the Munn-Silbey Approach to Nonlocal Exciton-phonon Coupling, *J Chem Phys.* 1994;*100*(3):2335.

[201] Sun J, Zhao Y, Liang W. Self-trapping of polarons with off-diagonal coupling, *Phys Rev B.* 2009;*79*(15):155112.

[202] Zhao Y, Zanardi P, Chen G. Quantum Entanglement and the Self-Trapping Transition in Polaronic Systems, *Phys Rev B.* 2004;*70*(19):195113.

[203] Chen L, Zhao Y, Tanimura Y. Dynamics of a One-Dimensional Holstein Polaron with the Hierachical Equations of Motion Approach, *J Phys Chem Lett.* 2015;*6*(15):3110-3115.

[204] Hildner R, Brinks D, Nieder JB, Cogdell RJ. Van Hulst NF. Quantum coherent energy transfer over varying pathways in single light-harvesting complexes. *Science.* 2013;*340*(6139):1448-1451.

[205] Chen LP, Gelin MF, Domcke W, Zhao Y. Theory of femtosecond coherent double-pump single-molecule spectroscopy: application to light harvesting complexes. *J Chem Phys.* 2015;*142*(16):164106.

[206] Chen LP, Gelin MF, Domcke W, Zhao Y. Simulation of Femtosecond Phase-Locked Double-Pump Signals of Individual Light-Harvesting Complexes LH2. *J Phys Chem Lett.* 2018;*9*(16):4488-4494.

[207] Zheng FL, Chen LP, Gao JB, Zhao Y. Fully Quantum Modeling of Exciton Diffusion in Mesoscale Light Harvesting Systems, *Materials.* 2021;*14*(12):3291.

[208] Meier T, Zhao Y, Chernyak V, Mukamel S. Polarons, Localization, and Excitonic Coherence in Superradiance of Biological Antenna Complexes. *J Chem Phys.* 1997;*107*(10):3876.

[209] Zhao Y, Meier T, Zhang WM, Chernyak V, Mukamel S. *J Phys Chem B.* 1999;*103*(19):3954-3962.

[210] Márquez AS, Chen LP, Sun KW, Zhao Y. Probing ultrafast excitation energy transfer of the chlorosome with exciton-phonon variational dynamics. *Phys Chem Chem Phys.* 2016;*18*(30):20298-20311.

[211] Smith MB, Michl J. Singlet Fission. *Chem Rev.* 2010;*110*(11),6891-6936.

[212] Berkelbach TC, Hybertsen MS, and Reichman DR. Microscopic theory of singlet exciton fission. I. General formulation. *J Chem Phys.* 2013;*138*(11):114102.

[213] Berkelbach TC, Hybertsen MS, and Reichman DR. Microscopic theory of singlet exciton fission. II. Application to pentacene dimers and the role of superexchange. *J Chem Phys.* 2013;*138*(11):114103.

[214] Musser AJ, Liebel M, Schnedermann C, Wende T, Kehoe TB, Rao A, Kukura P. Evidence for conical intersection dynamics mediating ultrafast singlet exciton fission. *Nat Phys.* 2015;*11*:352-357.

[215] Bakulin AA, Morgan SE, Kehoe TB, Wilson MW, Chin AW, Zigmantas D, Egorova D, Rao A. Real-time observation of multiexcitonic states in ultrafast singlet fission using coherent 2D electronic spectroscopy. *Nat Chem.* 2016;*8*:16-23.

[216] Monahan NR, Sun D, Tamura H, Williams KW, Xu B, Zhong Y, Kumar B, Nuckolls C, Harutyunyan AR, Chen G, Dai HL, Beljonne D, Rao Y, Zhu XY. Dynamics of the triplet-pair state reveals the likely coexistence of coherent and incoherent singlet fission in crystalline hexacene. *Nat Chem.* 2017;*9*(4):341-346.

[217] Fujihashi Y, Chen L, Ishizaki A, Wang J, Zhao Y, Effect of high-frequency modes on singlet fission dynamics. *J Chem Phys.* 2017;*146*(4):044101.

[218] Tempelaar R, Reichman DR. Vibronic exciton theory of singlet fission. I. Linear absorption and the anatomy of the correlated triplet pair state. *J Chem Phys.* 2017;*146*(17):174703.

[219] Tempelaar R, Reichman DR. Vibronic exciton theory of singlet fission. II. Two-dimensional spectroscopic detection of the correlated triplet pair state. *J Chem Phys.* 2017;*146*(17):174704.

[220] Morrison AF, Herbert JM. Evidence for Singlet Fission Driven by Vibronic Coherence in Crystalline Tetracene. *J Phys Chem Lett.* 2017;*8*(7):1442-1448.

[221] Elenewski JE, Cubeta US, Ko E, Chen H. Functional Mode Singlet Fission Theory. *J Phys Chem C.* 2017;*121*(8):4130-4138.

[222] Huang Z, Fujihashi Y, Zhao Y. Effect of off-diagonal exciton-phonon coupling on intramolecular singlet fission. *J. Phys. Chem. Lett.* 2017;*8*(14):3306-3312.

[223] Zeng T, Hoffmann R, Ananth N, The Low-Lying Electronic States of Pentacene and Their Roles in Singlet Fission. *J Am Chem Soc.* 2014;*136*(15):5755-5764.

[224] Petelenz P, Snamina M, Mazur G. Charge-Transfer States in Pentacene: Dimer versus Crystal. *J Phys Chem C.* 2015;*119*(25):14338-14342.

[225] Petelenz P, Snamina M. Locally Broken Crystal Symmetry Facilitates Singlet Exciton Fission. *J Phys Chem Lett.* 2016;*7*(10):1913-1916.

[226] Zirzlmeier J, Lehnherr D, Coto PB, Chernick ET, Casillas R, Basel BS, Thoss M, Tykwinski RR, Guldi DM. *Proc Natl Acad Sci USA*. 2015;*112*(17):5325-5330.

[227] Sun KW, Huang ZK, Gelin MF, Chen LP, Zhao Y. Monitoring of singlet fission via two-dimensional photon-echo and transient-absorption spectroscopy: Simulations by multiple Davydov trial states. *J Chem Phys*. 2019;*151*(11):114102.

[228] Miyata K, Kurashige Y, Watanabe K, Sugimoto T, Takahashi S, Tanaka S, Takeya J, Yanai T, Matsumoto Y. Coherent singlet fission activated by symmetry breaking. *Nat Chem*. 2017;*9*:983-989.

[229] Gelin MF, Borrelli R, Domcke W. Origin of Unexpectedly Simple Oscillatory Responses in the Excited-State Dynamics of Disordered Molecular Aggregates. *J Phys Chem Lett*. 2019;*10*(11):2806-2810.

[230] Pisliakov AV, Gelin MF, Domcke W. Detection of Electronic and Vibrational Coherence Effects in Electron-Transfer Systems by Femtosecond Time-Resolved Fluorescence Spectroscopy: Theoretical Aspects. *J Phys Chem A*. 2003;*107*(15):2657-2666.

[231] Chen L, Gelin MF, Chernyak V, Domcke W, Zhao Y. Dissipative dynamics at conical intersections: simulations with the hierarchy equations of motion method. *Faraday Discuss*. 2016;*194*:61-80.

[232] Chen L, Gelin MF, Zhao Y, Domcke W. Mapping of Wave Packet Dynamics at Conical Intersections by Time- and Frequency-Resolved Fluorescence Spectroscopy: A Computational Study. *J Phys Chem Lett*. 2019;*10*(19):5873-5880.

[233] Heller EJ. Time-dependent Approach to Semiclassical Dynamics. *J Chem Phys*. 1975;*62*(4):1544-1555.

[234] Heller EJ. Frozen Gaussians: A very simple semiclassical approximation. *J Chem Phys*. 1981;*75*(6):2923-2931.

[235] Heller EJ. Guided Gaussian Wave Packets. *Acc Chem Res*. 2006;*39*(2):127-134.

[236] Worth GA, Burghardt I. Full Quantum Mechanical Molecular Dynamics Using Gaussian Wavepackets. *Chem Phys Lett*. 2003;*368*(3-4):502-508.

[237] Lasorne B, Robb M, Worth GA. Direct Quantum Dynamics Using Variational Multiconfiguration Gaussian Wavepackets. Implementation Details and Test Case. *Phys Chem Chem Phys*. 2007;*9*(25):3210-3227.

[238] Curchod BFE, Martínez TJ. Ab Initio Nonadiabatic Quantum Molecular Dynamics. *Chem Rev*. 2018;*118*(7):3305-3336.

[239] Werther M, Choudhury SL, Großmann F. Coherent state based solutions of the time-dependent Schrödinger equation: hierarchy of approximations to the variational principle. *Int Rev Phys Chem*. 2021;*40*(1):81-125.

[240] Werther M, Großmann F. Apoptosis of moving nonorthogonal basis functions in many-particle quantum dynamics. *Phys Rev B*. 2020;*101*(17):174315.

[241] Shalashilin DV, Child MS. Basis set sampling in the method of coupled coherent states: Coherent state swarms, trains, and pancakes. *J Chem Phys*. 2008;*128*(5):054102.

[242] Kirrander A, Shalashilin DV. Quantum dynamics with fermion coupled coherent states: Theory and application to electron dynamics in laser fields. *Phys Rev A*. 2011;textit84(3):033406.

[243] Green JA, Shalashilin DV. Simulation of the quantum dynamics of indistinguishable bosons with the method of coupled coherent states. *Phys Rev A*. 2019;*100*(1):013607.

[244] Hagedorn GA. Raising and Lowering Operators for Semiclassical Wave Packets. *Ann Phys*. 1998;*269*(1):77-104.

[245] Faou E, Gradinaru V, Lubich C. Computing semiclassical quantum dynamics with Hagedorn wavepackets. *SIAM J Sci Comput*. 2009;*31*(4):3027-3041.

[246] Borrelli R, Peluso A. Quantum dynamics of electronic transitions with Gauss-Hermite wave packets. *J Chem Phys*. 2016;*144*(11):114102.

[247] Begušić T, Vaníček J. Finite-Temperature, Anharmonicity, and Duschinsky Effects on the Two-Dimensional Electronic Spectra from Ab Initio Thermo-Field Gaussian Wavepacket Dynamics. *J Phys Chem Lett*. 2021:*12*(11):2997-3005.

[248] Begušić T, Vaníček J. On-the-fly ab initiosemiclassical evaluation of vibronic spectra at finite temperature. *J Chem Phys*. 2020;*153*(2):024105.

[249] Chen L, Borrelli R, Shalashilin DV, Zhao Y, Gelin MF. Simulation of Time-and Frequency-Resolved Four-Wave-Mixing Signals at Finite Temperatures: A Thermo-Field Dynamics Approach. *J Chem Theory Comput.* 2021;*17*(7):4359-4373.

[250] Chen L, Sun K, Shalashilin DV, Gelin MF, Zhao Y. Efficient simulation of time-and frequency-resolved four-wave-mixing signals with a multiconfigurational Ehrenfest approach. *J Chem Phys.* 2021;*154*(5):054105.

[251] Ben-Nun M, Quenneville J, Martínez TJ. Ab Initio Multiple Spawning: Photochemistry from First Principles Quantum Molecular Dynamics. *J Phys Chem A.* 2000;*104*(22):5161-5175.

[252] Makhov DV, Glover WJ, Martínez TJ, Shalashilin DV. Ab initio multiple cloning algorithm for quantum nonadiabatic molecular dynamics. *J Chem Phys.* 2014;*141*(5):054110.

[253] Worth G, Robb M, Burghardt I. A Novel Algorithm for Non-Adiabatic Direct Dynamics Using Variational Gaussian Wavepackets. *Faraday Discuss.* 2004;*127*:307-323.

[254] Makhov DV, Symonds C, Alberti SF, Shalashilin, DV. Ab initio quantum direct dynamics simulations of ultrafast photochemistry with Multiconfigurational Ehrenfest approach. *Chem Phys.* 2017;*493*:200-218.

[255] Mignolet B, Curchod BFE, Martínez TJ. Communication: XFAIMS-eXternal Field Ab Initio Multiple Spawning for electron-nuclear dynamics triggered by short laser pulses. *J Chem Phys.* 2016;*145*(19):191104.

[256] Mignolet B, Curchod BFE. Excited-State Molecular Dynamics Triggered by Light Pulses - Ab Initio Multiple Spawning vs Trajectory Surface Hopping. *J Phys Chem A.* 2019;*123*(16):3582-3591.

[257] Zhao Y, Chen G, Yu L. Lattice and Spin Polarons in Two Dimensions. *J. Chem. Phys.* 2000;*113*(16):6502-6508.